NUMERICAL MODELLING OF A HEAVY GAS IN FAST ROTATION

Numerical modelling of a heavy gas in fast rotation
van Ommen, Klaas
Ph.D thesis, University of Twente, Enschede, The Netherlands
June 2010

ISBN 978-90-365-2896-2

NUMERICAL MODELLING OF A HEAVY GAS IN FAST ROTATION

PROEFSCHRIFT

ter verkrijging van de graad van doctor aan de Universiteit Twente
op gezag van de rector magnificus,
prof.dr. H. Brinksma.
volgens besluit van het College voor Promoties
in het openbaar te verdedigen op
17 juni 2010, 15.00 uur

door

Klaas van Ommen

geboren op 30 mei 1955
te Oldebroek

Dit proefschrift is goedgekeurd door de promotor:

prof. dr. ir. Th. H. van der Meer

Aan Hammy

Nomenclature

a	Radius of cylinder	[m]
A	Velocity parameter	[-]
Br	Brinkman number	[-]
D	Diffusion coefficient	[m^2/s]
l	Length of cylinder	[m]
L	Dimensionless length/radius ratio of the cylinder	[-]
Lm	Dimensionless length of the cylinder multiplied by *A*	[-]
M	Molecular weight	[kg/kmol]
T	Temperature	[K]
E	Ekman number	[-]
E_f	Flow efficiency factor	[-]
F_s	Tensile strength	[Pa]
m	Flow strength	[-]
*m**	Intrinsic flow strength	[-]
P	Pressure	[Pa]
P_w	Wall pressure	[Pa]
R	Radial coordinate	[m]
r	Dimensionless radial coordinate	[-]
R_0	General gas constant	[J/(Kmol)]
T_0	Average temperature of the gas	[K]
U	Radial gas velocity	[m/s]
u	Dimensionless radial gas velocity	[-]
V	Tangential gas velocity	[m/s]
v_w	Wall velocity	[m/s]
v_s	Velocity of sound	[m/s]
W	Axial gas velocity	[m/s]
w	Dimensionless axial gas velocity	[-]
x	Dimensionless radial coordinate	[-]
Z	Axial coordinate	[m]
z	Dimensionless axial coordinate	[-]

h	Heat transfer coefficient	[W/(m^2 K)]
λ	Thermal conductivity coefficient	[W/(mK)]
ρ	Density	[kg/m^3]
μ	Dynamic viscosity	[kg/(ms)]
γ	Ratio C_p / C_v	[-]
ω	Dimensionless angular velocity	[-]
θ	Dimensionless temperature	[-]
ζ	Dimensionless vorticity	[-]

ψ	Dimensionless stream function	[-]
ψ^*	Stream function	[kg/s]
ξ	Vorticity	[1/s]
$\underline{v}$	Velocity vector	[m/s]
Ω	Angular velocity	[1/s]
ε	Rossby number	[-]
Pr	Prandtl number	[-]
Br	Brinkman number	[-]
E	Ekman number	[-]
Re	Reynolds number	[-]

List of frequently used abbreviations

"ψ - ζ": refers to the model definition in (dimensionless) stream function – vorticity formulation, Appendix A8.

"*IBC*": refers to Ideal Boundary Conditions as defined in eq. (2.62) and eq. (2.63) applied at both end caps.

"*Semi-IBC*": refers to Ideal Boundary Conditions as defined in eq. (2.62) and eq. (2.63) applied one-sided at the top or bottom end cap.

"*SBC*": refers to Simple Boundary Conditions, constant temperatures at both end caps.

Three different parameter sets for gas centrifuges are defined, Section 2.5.1:

- "*Short*" centrifuge: a parameter set given by $1 < Lm < 1/\sqrt{Em}$.
- "*Semi-long*" centrifuge: a parameter set given by $1/\sqrt{Em} \cong Lm < 1/Em$.
- "*Long*" centrifuge: $Lm > 1/Em$.

The flow strength m is calculated from the Rossby number and the intrinsic flow strength by: $m = \varepsilon\, m^*$. The intrinsic flow strength m^* is defined in Appendix A, eq. (A94) and the Rossby number ε in Chapter 2, eq. (2.14).

Contents

Introduction

This thesis describes a study on the modelling of a heavy gas in a fast rotating cylinder. The subject has been studied widely since the middle of the 20th century due to the development of gas centrifuges for the separation of isotopes. A well-known application of centrifuge isotope separation is the enrichment of Uranium to be applied as fuel in nuclear reactors. More recently the same technology has been used to produce isotopes for medical and science applications, Ying and others [25], special isotopes, Mol [43] and for the production of pure Silica in computer applications, Tarbeyev [39]. The characteristics of the gas used in parameter studies in this thesis are based on UF_6 the gas used to separate Uranium isotopes for nuclear fuel, Dewitt [46]. UF_6 is a gas with a molecular mass of 352 kg/kmol hence the word “heavy” in the title of this thesis. What a gas centrifuges can look like is explained in Chapter 1.

The isotope separation performance of a gas centrifuge is determined by two physical phenomena: isotope transport in a gas phase and the gas flow inside the rotating cylinder. Obviously these are coupled, the transport of isotopes is partly by convection and this convection is determined by the gas flow. Isotope transport in a gas phase and how it plays a role in the performance of a centrifuge is well understood and will be summarised in the first chapter of this thesis. The gas flow inside a rotating cylinder is a complex phenomenon and has been the subject of several analytical and numerical approaches. Brouwers [3] developed an analytical model based on mathematical techniques stemming from geophysical disciplines and predicts that several, vertical, flow regions coexist in a gas centrifuge. The position of these flow regions plays an important role in determining the flow pattern and subsequently the performance of a centrifuge. Analytical solutions predicting the flows in these regions are available, however, subject to symmetrical boundary conditions at top and bottom end cap. Numerical models to simulate the flow in a rotating cylinder have been published, they do not deal with complex boundary conditions either. These various models and approaches on the fluid dynamics of a gas in a rotating cylinder are discussed in detail in Chapter 2.

The available analytical models provide theoretical insight and give directional answers from an engineering point of view as well: they provide quickly an indication how the performance of a centrifuge varies with e.g. length, diameter, wall pressure and wall velocity.

Two questions are raised concerning the validity and accuracy of the analytical approach. The first question is: do the flow regions appear in a numerical model as predicted by the analytical approach and how accurately is their radial position predicted? This is important since it determines the accuracy of the predicted separation performance of a centrifuge. The second question is the impact of less than ideal boundary conditions on the flow pattern and separation performance. Does the separation performance show a considerable decrease or is it highly forgiving with respect to the precise boundary conditions? With respect to the boundary conditions: the wall, end caps of cylinder as well as the containing environment have certain thermal properties. These thermal properties result in a temperature distribution along the wall and end caps of the cylinder and as such they are interacting directly with the

gas flow since they form the boundary conditions for the energy distribution in the cylinder. How strong is this interaction? If the material of the end cap is upgraded to a material with very different thermal properties, does it change the performance of the centrifuge? All these considerations are addressed in Chapter 3 where the final model is presented. The numerical approach used to solve the model equations is introduced in Chapter 4.

Calculation of the separation performance of a gas centrifuge is complex and engineers like a simple, easy to use directional design tool to be used during strategic studies. This means that there is a demand for a simple representation of the separation performance of a centrifuge which captures most or all of the important parameters playing a role. This is the subject of Chapter 5 where the model will be applied as an “Engineering tool”.

In Chapter 6 and 7 specific results are presented dealing with the effects of very high wall speeds on the internal flow and the effects that the thermal properties of the cylinder wall and end caps have on the performance of the centrifuge.

This thesis is based on information that can be found in open literature and it does not contain any classified information.

Chapter 1

Centrifuge for Isotope separation

1.1 Description of a centrifuge

A schematic example of a gas centrifuge for isotope separation is given in Fig. 1.1. This sketch is from a patent by RCN, Reactor Centre Netherlands, Los and Wind [1].

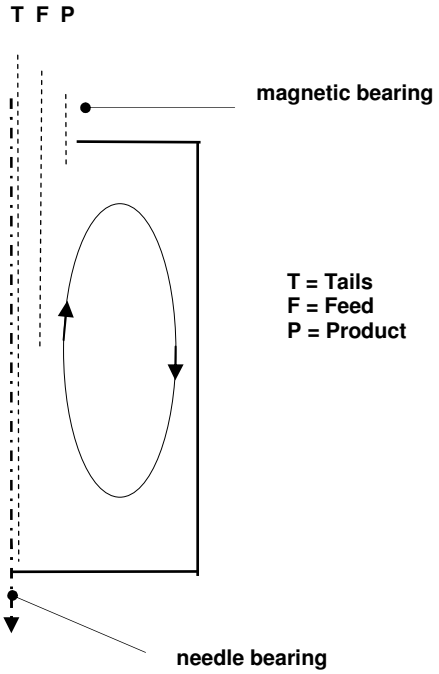

Figure 1.1: A schematic overview of a gas centrifuge indicating the feed (F), depleted (T) and enriched (P) gas flow.

A centrifuge is a vertical cylinder with a point bearing at the bottom and a magnetic bearing at the top, rotating at high velocities. Tubes for feeding (F) gas into the cylinder and to extract the enriched (P) and depleted (T) gas out of the cylinder are led through the centre of this magnetic top bearing.

Designs of centrifuges might be more complicated than the description in the patent by Los and Wind [1]. An example is the publication of Harada and Koyama [35] about the flow around obstacles attached to the rotating wall.

Various materials have been quoted over the years to improve separation performance of centrifuges by increasing its rotational velocity. Modern materials like Carbon fibre

as suggested by Dan Charles [45] allow for high to very high rotational velocities. These commercial Carbon fibres are available with tensile strength (F_s) of more than 4000 MPa and have a density (ρ) of 2500 kg/m^3 or less. The velocity at which a thin walled individual ring of this material would break can be calculated by classical mechanics according to:

$$v_w^2 = \frac{F_s}{\rho} \text{ or } v_w = \sqrt{\frac{4}{2.5}} 10^3 \approx 1200 \text{ m/s} \tag{1.1}$$

This result indicates that it is realistic to assume that velocities up to 1000 m/s are applicable for modern centrifuges. High tensile steel would allow for velocities up to about half of this velocity due to its lower tensile strengths and higher densities. Additional material properties play important roles, e.g. chemical resistance to the applied gas and long term creep of the material. Creep depends on the applied temperatures and influences the maximum allowable gas wall pressure inside the centrifuge. As an example: at room temperature is UF_6 in a gaseous state up to a pressure $\approx$ 0.1 bar and sublimates into a solid state if the temperature is lowered or the pressure increased. UF_6 sublimates into a solid at a pressure exceeding 1.0 bar at a temperature of $\approx 60\,^0C$.

Due to the very high velocities there is a need to maintain a low gas pressure outside the cylinder to prevent frictional forces from overheating the cylinder material and to limit the energy required to rotate the cylinder. This means that energy transport between all outer surfaces of the rotating cylinder and the containing environment is by radiation only.

Typical centrifuge diameters mentioned in literature by Matsuda [2] and Brouwers [3] are 0.13 to 0.20 m and lengths to radius ratios much higher than 1 are assumed. Data published by the USEC, the United States centrifuge programme on their website, indicates that the US machines have a larger radius, typically a diameter of 0.3 to 0.4 m and a length of at least 6.0 meters, as can be seen at the website of USEC [40]. This indicates a length to radius ratio of ≈ 40 .

This difference in size is likely to be a contributing factor to the different views on economical optimisation of the centrifuge plant. It seems that the smaller size, as developed by the European industry has clear advantages, since 2 out of 3 separation plants currently (2009) under construction in the US are based on these designs [47].

The working fluid used to separate Uranium isotopes, UF_6 has a molecular weight of 352 and $\gamma = \frac{C_p}{C_v} \approx 1.06$, Dewitt [46].

Consequently the velocity of sound is calculated to be:

$$v_s = \sqrt{\gamma R_0 T / M} \tag{1.2}$$

resulting in approximately 80 m/s at room temperature.

v_s is much lower than v_w, so any disturbance of the rotating gas by mechanical means will result in a shockwave upstream of the leading edge of the object.

The amount of gas rotating inside the cylinder results in an increasing gas pressure towards the wall. A typical wall pressure value mentioned by Brouwers [3] is 8000 Pa. This can be higher as long as the gas temperature inside the cylinder is well above the sublimation temperature corresponding to the local gas pressure. If sublimation occurs, meaning that solid UF_6 crystals develop at the rotating cylinder wall, where the gas pressure is high, then potential mechanical damage of the cylinder might occur. The pressure profile for UF_6 , due to its high molecular mass, is very steep. This pressure profile results in a gas pressure in a large cross sectional area so low, that it can be considered as “empty” and not used for separation of isotopes. Increasing the wall pressure is a first measure to make more use of the available rotational forces acting on the gas molecules. The importance of the wall pressure on the overall efficiency of the gas centrifuge is clearly indicated and stressed by early publications stemming from the centrifuge project in Europe, as will be quoted below.

Centrifuge development is a global research activity and publications on separation theory and gas dynamics in a rotating cylinder can be found from around the world. Examples are: United States, Parker & Mayo [50], Steenbeck [48], Cohen [6] and von Halle [8]; Netherlands, Los [1] and [36], Brouwers [3], [4] and [42]; Russia, Borisevich [37], Sweden, Bark and Bark [5]; Japan, Matsuda [2], [16], [24] and Makihara & ITO [29]; France, Soubbaramayer [7]; United Kingdom, Dickinson & Jones[17] more recently Brazil: Migliavacca, Rodrigues & Nascimento [28], Andrada [33], Peirera [19] and Lopez [20] and more. Some of these resources are directly linked to actual centrifuge projects and plants, e.g. Los and Brouwers to the development of centrifuge technology in the Netherlands, Dickinson & Jones in the UK and Cohen in the US. It is expected that these models in one or another form have been used in plant development. For the others it is less clear whether they are connected to projects or that they perform more academically based studies

In the following sections the basics of a centrifuge and the theoretical background of Isotope Separation will be discussed, resulting in defining the objective of this study.

1.2 Centrifuge basics

As mentioned in 1.1, a common concept of a centrifuge is the one in which feed is introduced at one location in the centrifuge and depleted and enriched gas is removed. The three tubes enter the rotating cylinder from the top, as illustrated in Mol [43] and Wood [44]. The position of the feed is approximately at half the height along the centre line. In Los [36] the optimal position of the feed flow into the cylinder as a function of separation characteristics (enriching and depleting factors) is given; Japanese literature shows the same configuration, e.g. Matsuda [2] and Nakayama [14]. The overall effect of the feed both in terms of flow and position along the axial axis on the

separation performance is limited. Los [36] shows that for optimal performance of the centrifuge, the internal flow in the centrifuge is several times higher than the feed flow but the internal flow in absolute value is still very low. Therefore in most studies the effect of the feed gas on the internal flow is ignored, as it will be in this thesis.

The centrifugal forces acting on the gas mixture fed into the cylinder result in an increase of concentration of the heavy component close to the wall and of the light component near the centreline. This is the primary separation effect of a centrifuge. Cohen [6] and Los [36] show that this primary separation is relatively small and that it can be magnified by enforcing an axial flow pattern inside the cylinder, as schematically seen in Fig. 1.1 and 1.2.

The explanation of this effect is as follows: in this closed circulation, the heavier components located near the rotating wall are moved towards the bottom and the lighter components along the centre line towards the top, as a result of this an axial concentration gradient develops. This axial separation appears to be considerably higher than the primary one, depending on the flow, feed conditions (amount of fresh gas entering the cylinder) and some characteristics of this closed circulation. These characteristics, Los [36], are:

- the shape of the radial distribution of the velocity
- the overall amount of gas circulating in the cylinder.

The ideal shape of this internal circulation is the one that transports the same amount of gas per unit area in [kg/(sm^2)] over an as large as possible part of the cross section of the cylinder. The amount of circulating gas has to be optimised. A too low circulation rate will result in an overall axial separation close to the primary separation factor. If the circulating amount of gas is too high, than the centrifugal force acting on the two components is unable to separate the components sufficiently while the gas is flowing from the bottom to the top near the centreline and towards the bottom along the cylinder wall.

Practice and theory have shown that the optimal internal circulation is very small, because of the time needed to separate the mixture. Given that only a small circulation is necessary simplifies the analysis to some extent. The fluid dynamic model can be simplified to a linear model. This model will be derived, presented and discussed in the next chapter.

The circulating internal gas moves in a boundary layer along the end caps and the cylinder wall. These layers become extremely thin, complicating the mathematical modelling of this phenomenon. The layers along the end caps can be locally as thin as 0.01 to 0.001 of a mm and along the cylinder wall down to $\approx$ 0.5 mm presenting severe challenges in developing the numerical model as will be explained later in this thesis.

The amount and to some extent the velocity profile of the circulating gas can be tuned and optimised in two ways, Brouwers [4]:

- by a mechanical drive, which means that the gas at the bottom of the cylinder is slowed down, relative to the cylinder wall and the isothermal rigid body rotation. This can be done by penetration of a (small) tube or bar in the gas
- by a thermal drive, by heating the temperature at the bottom and/or cooling down the gas at the top of the cylinder. Furthermore this drive is influenced by the axial profile over the cylinder wall. In Fig. 1.2 this profile is shown to be linear although that is not necessarily the case.

Both drives result in the same effect: higher temperature and/or lower rotational velocity at the bottom will result in somewhat higher gas pressure at the centreline compared to isothermal rigid body rotation pressure profiles. This higher pressure results in a gas flow towards the top where the gas pressure is lower.

Decreasing the temperature at the top has the same effect: the gas density increases which results in a lower pressure near the centreline compared to the pressure caused by the isothermal rigid body rotation. As a result, the gas is “sucked” from the bottom towards the top adding to the effects of mechanical drive at the bottom and the locally higher temperature at the bottom. Obviously, the driving phenomena, thermal and/or mechanical drives, are not necessarily constant over the radius. By adding a profile over the radius to the temperature increase/decrease and/or rotational velocity reduction at the bottom, the shape of the internally circulating flow pattern can be influenced. An increasing temperature towards the centreline will generate a progressively higher pressure near the centre line and generate a higher velocity at this location. Similarly for the cooling of the gas at the top, a lower temperature towards the centreline will reduce progressively the pressure and increase the suction near the centreline and consequently more gas is flowing at this location.

Subsequently extraction of the enriched gas at the top and depleted gas near the bottom results in two gas streams: a product stream and a tails stream, these stream have to be further processed.

Scoops sticking to some extent into the rotating gas can be used for extraction of the enriched gas at the top and depleted gas at the bottom. The scoop for the tail stream can be used to serve a triple function:

- the scoop extracts the depleted gas
- by sticking it into the rotating gas, energy will be dissipated and consequently the local temperature will increase causing the thermal drive as mentioned above
- the same effect causes a mechanical drive. Sticking the scoop in the gas will reduce the rotational velocity.

As is shown in Fig. 1.2, based on Kai and others [34], these effects can be uncoupled to some extent by applying a perforated plate just above the scoop, shielding the scoop from the main compartment. The gas is sucked close to the wall and injected at a

smaller radius into the main compartment. Furthermore the plate prevents any resulting shockwave attached to the scoop from adversely influencing the flow inside the cylinder. The heat generated by the scoop will be transported to the gas via the shielding plate. Wood [44] shows a depleted gas scoop at the bottom which is not covered by a shielding plate or baffle.

The extraction scoop for the enriched gas, at the top, has to be shielded from the gas in the rest of the rotating cylinder because the three effects generated by the scoop on the gas near the bottom are unwanted at the top. To suck the gas towards the top, a temperature decrease is needed as mentioned earlier in this section and the same holds for the rotational velocity: a reduction of the rotational velocity at this location is not wanted since this will reduce the suction effect, as presented by Wood [44]. An external cooling can be used to cool the top of the cylinder generating the needed thermal drive.

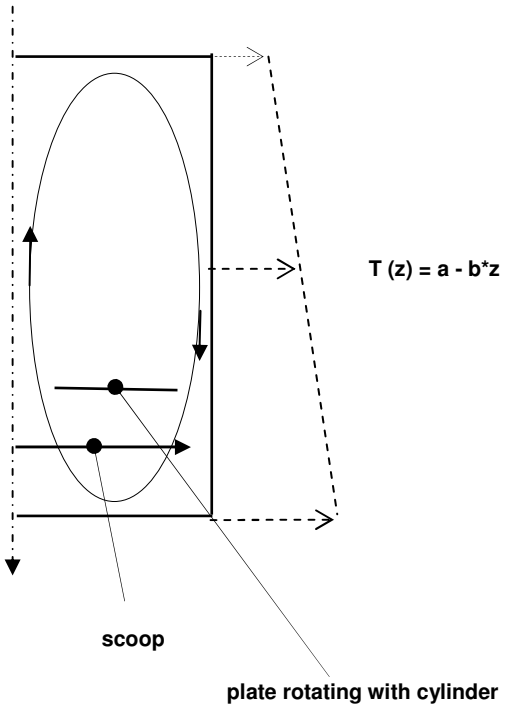

Figure 1.2: Schematically showing the internal gas flow in a gas centrifuge driven by a mechanical and thermal drive mechanism. A perforated plate shields the mechanical drive generated by the scoop.

1.3 Separation theory

In a centrifuge, the primary separation results from the centrifugal forces acting on the components of the mixture. A detailed explanation of the physics behind separation in a gas phase can be found in Cohen [6], which was later applied and extended by Los

[36]. Von Halle [8], Olander [9] and Hirschfelder [10] published several reviews and considerations on these works. They considered the separation theory from a fundamental point of view and used analytical methods to predict the separation performance of a centrifuge.

From Cohen [6], the transport equation for the molecular concentration C_N of component *N* in a binary mixture is obtained:

$$\frac{1}{ar}\frac{\partial}{\partial r}\left(r\rho u C_N + rJ_r\right)+\frac{1}{l}\frac{\partial}{\partial z}\left(\rho w C_N + J_z\right)=0 \qquad (1.3)$$

with *r* and *z* the dimensionless radial and axial coordinates. r and z are defined as *r = R/a* and *z = Z/l, a* is the radius and *l* is the length of the rotating cylinder.

The first term is radial convection + diffusion of component *N* and the second term the axial convection and diffusion. Obviously, transient effects are not of interest and since temperature gradients are very small, as will be discussed later, thermal diffusion will be neglected. Due to the nature of a centrifuge, radial pressure gradients are much larger than axial pressure gradients. With these assumptions, eq.(1.3) can be completed by substituting the diffusion terms:

$$J_r = -\rho D\left\{\frac{\Delta M}{R_0 T}\omega^2 ar C_N(1-C_N)+\frac{1}{a}\frac{\partial}{\partial r}\left(C_N\right)\right\}$$

$$J_z = -\frac{\rho D}{l}\frac{\partial}{\partial z}\left(C_N\right) \qquad (1.4)$$

By neglecting convection and axial effects in eq. (1.3), then this equation describes the primary separation of the components in radial direction only, which can be found by substituting the radial diffusion of eq. (1.4) in the radial term of eq. (1.3). Cohen [6] shows that this primary separation is relatively small and that enforcing an axial flow pattern inside the cylinder, as schematically seen in Fig. 1.1 and 1.2, can strengthen it. This can be explained as follows: by consequently moving the heavier components located near the rotating wall towards the bottom and the lighter components along the centre line to the top, an axial concentration gradient develops. This axial separation is potentially much higher than the primary one, depending on the flow and feed conditions. Separation of the gas isotopes results from tapping enriched gas at the top and depleted gas near the bottom.

Los [36] uses eqs. (1.3) and (1.4) to derive a simple relation enabling the calculation of the separation power of this type of centrifuge:

$$\delta U = 0.81 E_f m^2/(1+m^2)\delta U_{\max} \qquad \text{[kg/s]} \qquad (1.5)$$

E_f is the "f*low efficiency*" , defined by:

$$E_f = \frac{4\left[\int_0^1 \psi^*(r) r dr\right]^2}{\int_0^1 \frac{\left[\psi^*(r)\right]^2}{r} dr} \qquad [-] \qquad (1.6)$$

m is the *"flow strength"* defined by*:*

$$m = \sqrt{\int_0^1 \frac{\psi^*(r)^2}{r} dr} \Big/ \left(\sqrt{2}\pi\rho a D\right) \qquad [-] \qquad (1.7)$$

$\delta U_{\max}$ is the theoretically maximal achievable separation:

$$\delta U_{\max} = \frac{\pi l \rho D}{2}\left[\frac{\Delta M v_w^2}{2R_0 T_0}\right]^2 \qquad [kg/s] \qquad (1.8)$$

ΔM is the difference in molecular mass between the two fractions and $\psi^*(r)$ is defined as the stream function according to:

$$\psi^*(r) = 2\pi a^2 \int_0^r \rho(r^*) w(r^*) r^* dr^* \qquad [kg/s] \qquad (1.9)$$

The factor 0.81 as derived by Los [36] is due to the effect of the closed circulation inside the cylinder. A feature of this internal circulation is that the concentration gradient in radial direction at the very top and bottom is negligible.

The flow strength m is a measure of the flow associated with the internal circulation. The required value follows from the overall design of separation plant (number of stages and the required isotope concentration in the product flow of the plant) and is outside the area of interest of this thesis. From eq. (1.5) it is deducted that it is advisable to aim at values of m higher than 3 to obtain a high separating performance of the centrifuge.

Eq. (1.5) is widely used in studies and is referred to in many articles, as it is easy to use. Based on the analysis of Los, the formulation is only valid if E_f and m are constant over the length of the centrifuge. In practice this can be overcome by applying averaged values for both parameters. Standard numerical methods can be used to solve eq. (1.3), resulting in the concentration field in the centrifuge. These results can be used to validate the accuracy of eq. (1.5). An example of this approach can be found in Kai [15].

As can been seen from eq. (1.5), the last term of the equation has the fourth power to the wall velocity, showing the overall importance of this parameter in terms of achievable separation performance. An increasing wall velocity will affect the flow inside the cylinder resulting in a lower flow efficiency factor E_f. Furthermore it follows from Los [36] that E_f has a maximum attainable value of 1 if the stream function is quadratic with radius, meaning that a constant flux of gas is flowing through each area of the cross section of the cylinder in the centre from the bottom to the top and back along the wall to the bottom end cap in a very thin layer. The closer the stream function profile approaches this quadratic function, the higher E_f.

1.4 Objective of the study

There is a clear requirement in the separation industry to have a model readily available to accurately predict the separation performance of a centrifuge, subject to engineering choices and challenges.

On the one hand, the equation to calculate the separation performance, eq. (1.5), is very transparent and elegant. On the other hand, calculating the flow efficiency factor E_f and flow strength m is complicated. Obviously the result of eq. (1.5) is only as good as the accuracy of the predicted flow efficiency factor E_f, which is the subject of this thesis. Over the years several approaches were developed to calculate these parameters. Due to the increasing strength of modern materials the rotational velocity can be increased, positively influencing the separation performance. In this thesis the main focus will be on very high wall velocities up to 1000 [m/s]. This is considered to be the upper limit for materials currently available. Validity of models developed during the era of lower velocities will be tested by applying numerical techniques and software specifically developed to simulate the flow in a fast rotating cylinder. It will be shown that besides velocity, temperature, wall pressure, overall dimensions of the cylinder as well as thermal properties of used materials for the various parts of the rotating cylinder and thermal conditions are influencing E_f to some extent and m considerably. Furthermore these two parameters can be optimised under the assumption of certain, “ideal” chosen boundary conditions. Some of these ideal boundary conditions cannot be achieved in a real life situation due to limits in physics and/or design options of a centrifuge as will be discussed in the next chapter. In this thesis the consequences of moving from ideal to these achievable boundary conditions will be shown as well.

In Chapter 2, literature will be discussed and a mathematical model is derived. Chapter 3 deals with modelling a centrifuge as a whole. In Chapter 4, a numerical approach is designed and in Chapter 5 a parameter study is presented showing how E_f and m develops under various variations of boundary values and design choices. Chapter 6 deals with the impact of increasing the wall velocity to very high values on the flow. In Chapter 7, the effect of the thermal properties of the materials applied for the cylinder wall and end caps will be discussed.

Chapter 2

Literature review and mathematical formulation

Summary

The objective of this study is predicting the flow efficiency (E_f) and flow strength (m) of a centrifuge as defined in Chapter 1. In this chapter a mathematical model will be derived and relevant literature sources quoted and reviewed. In Section 2.5 analytical results are discussed. The analytical models are mainly stemming from the 70's when computers and numerical computing techniques were still in their childhood. The analytical results are very valuable to gain detailed insight in all aspects of the fluid dynamics in the gas centrifuge. Full details regarding the derivation of the equations are given in Appendix A. Interested readers are advised to read this appendix.

2.1 Basic equations of the fluid dynamics model

The mathematical model is based on the following equations, here for convenience given in vector notation employing absolute velocities.

Momentum conservation according to Navier Stokes:

$$\rho\left(\frac{\partial \underline{v}}{\partial t}+\underline{v}.\nabla\underline{v}\right)=-\nabla P+\mu\nabla^2\underline{v}+f+(\ \mu/3+\mu^V)\,\nabla(\nabla.\underline{v}) \tag{2.1}$$

Mass conservation equation:

$$\frac{\partial(\rho)}{\partial t}+\nabla.(\rho\underline{v})=0 \tag{2.2}$$

Energy conservation equation:

$$\rho C_p\left(\frac{\partial T}{\partial t}+\underline{v}.\nabla T\right)=-\frac{T}{\rho}\left(\frac{\partial\rho}{\partial T}\right)_p\underline{v}.\nabla P+\lambda\nabla^2T+\Phi \tag{2.3}$$

Equation of state for an ideal gas:

$$P=\rho\frac{R_0T}{M} \tag{2.4}$$

This study focuses on the separation performance of a gas centrifuge. Therefore only steady behaviour of the gas flow inside the rotating cylinder is of interest and non-steady terms in the equations will be removed. According to Dewitt [46], UF_6 can be modelled as an ideal gas with almost constant properties over a wide temperature range; this allows to remove the bulk viscosity and to assume constant material

properties for viscosity and thermal properties. These assumptions simplify the energy equation since:

$$-\frac{T}{\rho}\left(\frac{\partial \rho}{\partial T}\right)_p = 1$$

for an ideal gas.

Body forces (e.g. gravitational) are extremely small compared to the rotational forces in this application and are neglected as well.

In view of the overall rotation of the system, it may be preferable to describe the flow in terms of a relative velocity $\underline{v}$ with respect to a co-rotating coordinate system. The governing equations then take the following form:

Navier Stokes

$$\rho(\underline{v}.\nabla)\underline{v} + 2\rho\underline{\Omega}\times\underline{v} - \rho\nabla\left(\frac{1}{2}\Omega^2 r^2\right) = -\nabla P + \mu\left(\nabla^2\underline{v} + \frac{1}{3}\nabla(\nabla.\underline{v})\right) \tag{2.5}$$

with $2\rho\underline{\Omega}\times\underline{v}$ the Coriolis term and $\rho\nabla\left(\frac{1}{2}\Omega^2 r^2\right)$ representing the centrifugal forces acting on the fluid, written as the gradient of a scalar potential.

continuity equation

$$\nabla.(\rho\underline{v}) = 0 \tag{2.6}$$

energy equation

$$\rho C_p\left(\underline{v}.\nabla T\right) = \underline{v}.\nabla P + \lambda\nabla^2 T + \Phi \tag{2.7}$$

As mentioned in Chapter 1, three-dimensional flow effects can develop locally around the gas extracting scoops but are not expected to be of major concern for the remainder of the flow in the cylinder. This assumption and the applied linearization to be discussed in the following sections are the only significant simplifications in this thesis. In Matsuda [16] a study is published on the three-dimensional effects around a scoop placed in a centrifuge. In all other cases axisymmetrical conditions are assumed.

Studies applying full Navier Stokes solvers have become available over the past decades and are quoted in a few publications, Nakayama [14], Merten [38], Kai [15] and Park [32]. Very detailed configurations are being modelled, however, at a cost: to have super computers available. They form a different league. These studies and models are very useful for final design calculations when most or all of the engineering parameters are frozen but less useful during earlier design phases during which more directional supporting tools are needed to evaluate the relevance of multiple changes in the design, which is the subject of this thesis. As discussed in Chapter 1, the internal flow in a centrifuge is small and the need to resolve in all design phases the fully detailed set of equations (2.5), (2.6) through (2.7) is doubtful. Merten [38] explicitly confirms this by concluding that linear models are sufficiently accurate and full Navier Stokes equations is not necessary to gain insight in all parameters affecting the flow efficiency and flow strength.

2.1.1 Dimensionless equations

Firstly a “reduced pressure” is defined as

$$\nabla P_r = \nabla P - \rho\nabla(\frac{1}{2}\Omega^2 r^2) \tag{2.8}$$

a result that can be used to simplify eq. (2.5):

$$\rho(\underline{v}.\nabla)\underline{v} + 2\rho\underline{\Omega}\times\underline{v} = -\nabla P_r + \mu(\nabla^2\underline{v} + \frac{1}{3}\nabla(\nabla.\underline{v})) \tag{2.9}$$

The following non-dimensional variables are defined:

$$\underline{v}^* = \frac{\underline{v}}{U}, P^* = \frac{P_r}{\rho_w \Omega a U}, \rho^* = \frac{\rho}{\rho_w}, T^* = \frac{T}{T_0} \text{ and } P_t^* = \frac{P}{\rho_w v_w^2} \tag{2.10}$$

and dimensionless length scales:

$$r = \frac{R}{a},\ z = \frac{Z}{l}\ ,\ L = \frac{l}{a} \tag{2.11}$$

with

$$v_w = \Omega a \tag{2.12}$$

the wall velocity, ρ_w the density at the wall, a the radius of the cylinder and Ω the angular velocity of the rotating cylinder. U is a small velocity in the co-rotating framework. Furthermore, the dimensionless length ratio *L* will be used, *L* will be referred to as the aspect ratio of the cylinder. p_w is the pressure at the wall.

Incorporating the dimensionless parameters and variables in eq. (2.9), the Navier-Stokes equation takes the following form:

$$\varepsilon\rho^*(\underline{v}^*.\nabla^*)\underline{v}^* + 2\rho^*\underline{k}\times\underline{v}^* = -\nabla^* P^* + E(\nabla^2\underline{v}^* + \frac{1}{3}\nabla^*(\nabla^*.\underline{v}^*)) \tag{2.13}$$

with $\underline{k} = \frac{\underline{\Omega}}{|\underline{\Omega}|}$ is the unit vector in axial direction.

Furthermore, the following dimensionless variables are used:

- the Rossby number ε, which is a measure of the ratio of Coriolis and inertial forces since

$$\varepsilon = \frac{\left[(\underline{v}.\nabla)\underline{v}\right]}{\left[\underline{\Omega}\times\underline{v}\right]} = \frac{U^2/a}{\Omega U} = \frac{U}{\Omega a} \tag{2.14}$$

- the Ekman number E, describing the relative importance of viscous forces relative to the Coriolis forces

$$E = \frac{\left[\upsilon\nabla^2\underline{v}\right]}{\left[\underline{\Omega}\times\underline{v}\right]} = \frac{\upsilon U/a^2}{\Omega U} = \frac{\upsilon}{\Omega a^2} \tag{2.15}$$

ν is the kinematic viscosity of the fluid. Typical values for the Ekman number in these applications are 10^{-4} to 10^{-8}. The Rossby number ε is usually very small, as it scales the perturbations relative to the rigid-body rotation. The Rossby number is defined by the driving mechanism of the internal flow; e.g.: if the flow is driven by an end cap rotating at a somewhat different angular velocity compared to the cylinder wall at an angular velocity of $\Omega + \Delta\Omega$ or has a temperature $T_0 + \Delta T$, then ε follows from:

$$\varepsilon = \frac{\Delta\Omega}{\Omega} \text{ or } \varepsilon = \frac{\Delta T}{T_0} \tag{2.16}$$

Obviously both driving mechanisms can be combined and ε should be calculated accordingly. Alternatively a temperature gradient of ∇T along the wall can be applied resulting in the same definition of ε.

Assuming a very low Rossby number, ε << 1, eq. (2.13) can be simplified by neglecting the inertial forces which results in:

$$2\rho^*\underline{k}\times\underline{v}^* = -\nabla^*P^* + E(\nabla^2\underline{v}^* + \frac{1}{3}\nabla^*(\nabla^*.\underline{v}^*)) \tag{2.17}$$

This equation is the basis for the linearization as will be executed in the next sections.

The energy equation is given by eq. (2.7):

$$\rho C_p\left(\underline{v}.\nabla T\right) = \underline{v}.\nabla P + \lambda\nabla^2 T + \Phi \tag{2.18}$$

Here Φ represents an internal heat source (in the gas) due to viscous dissipation and is of the order:

$$\Phi \sim \mu(\nabla\underline{v})^2 .$$

Applying the dimensionless variables as defined in eqs. (2.10) – (2.12), then this equation can be written as:

$$\varepsilon a \rho_w C_p v_w T_0 \rho^* \left(\underline{v}^* . \nabla^* T^* \right) = \varepsilon a v_w^3 \rho_w \underline{v}^* . \nabla^* P_t^* + \lambda T_0 \nabla^{*2} T^* + \varepsilon^2 \mu v_w^2 \Phi^* \qquad (2.19)$$

with

$$\Phi^* \approx (\nabla^* \underline{v}^*)^2$$

Rearranging terns in eq. (2.19) results in:

$$\varepsilon \frac{Pr}{E} \rho^* \left(\underline{v}^* . \nabla^* T^* \right) = \varepsilon \frac{Br}{E} \underline{v}^* . \nabla^* P_t^* + \nabla^{*2} T^* + \varepsilon^2 Br \Phi^* \qquad (2.20)$$

where

$$Br = \frac{\mu v_w^2}{\lambda T_0} \text{ and } Pr = \frac{\mu C_p}{\lambda} \qquad (2.21)$$

Br is the Brinkman number, *E* is the Ekman number as defined in eq. (2.15). *Br* is a non-dimensional number representing the ratio of heat production and diffusion terms:

$$Br = \frac{[\Phi]}{[\lambda \nabla^2 T]} = \frac{\mu v_w^2}{\lambda T_0} \qquad (2.22)$$

Pr is the Prandtl number, for most gasses *Pr* $\approx$ 1. In this study it is assumed that *Br* can reach values up to $\approx$ 10.

2.1.2 Iso-thermal rigid body rotation

A radial pressure gradient present in static equilibrium ($\underline{v} = 0$) can be calculated from eq. (2.9) by:

$$\nabla P_r = \nabla P_s - \rho_s \nabla (\frac{1}{2} \Omega^2 r^2) = 0 \qquad (2.23)$$

with P_s, ρ_s the pressure and density in static equilibrium, respectively.

Substituting the ideal gas relation and the definition for the density and applying the definition for the wall velocity yields:

$$\rho_s \frac{M}{R_0 T_0} v_w^2 r = \frac{\partial P_s}{\partial r} \qquad (2.24)$$

Integration of this equation and applying the boundary condition $P_s\big|_{r=1} = P_w$ results in:

$$P_s(r) = P_w e^{-x} \tag{2.25}$$

with

$$x = A(1 - r^2) \tag{2.26}$$

defined as a new radial coordinate and

$$A = \frac{1}{2}\frac{Mv_w^2}{R_0 T_0} \tag{2.27}$$

Subsequently for the density results:

$$\rho_s(r) = \rho_w e^{-x} \tag{2.28}$$

The coordinate *x* fits the physics of the problem much better than the radial coordinate *r*, which is just a geometrical dimension. By applying *x,* all equations can be scaled relative to the exponential pressure decrease.

Eqs. (2.25) and (2.28) are the pressure and density distribution in iso-thermal rigid rotation. In dimensionless form these are defined as:

$$\overline{P}(r) = e^{-x} \text{ and } \overline{\rho}(r) = e^{-x} \tag{2.29}$$

with

$$\overline{\rho}(r) = \frac{\rho_s(r)}{\rho_w} \text{ and } \overline{P}(r) = \frac{P_s(r)}{P_w} \tag{2.30}$$

Substituting the definition for *A* , the Brinkman number definition can be expressed as:

$$Br = 2A\frac{\mu R_0}{\lambda M} \tag{2.31}$$

For Uranium Hexafluoride (UF_6), $M = 352$, $\mu = 1.710^{-5}$ kg/(ms) and $\lambda = 710^{-3}$ W/(mK), meaning that at wall velocities of 500 m/s: $A \approx 16$ and $Br \approx 2$. At 1000 m/s: $A \approx 64$ and $Br \approx 8$.

From eqs. (2.28) and (2.29) it follows that if *A* is much higher than one, a region near the centre line (high values of *x*) will develop with an extremely low density. The continuum approximation is no longer valid in this domain. Very low density gas dynamics is referred to in the literature as Knudsen flow, some centrifuge studies focus on this. Mass transport in this domain is so low that it can be neglected, e.g. Borisevich [37].

2.2 Linear equations in primary variables

The internal flow induced in the centrifuge to magnify the primary separation effect (Section 1.3) is small. This keeps the mass transport inside the cylinder small and allows eliminating nonlinearities in the governing equations. The linearization applied in this study is based on the perturbation method. The perturbation approach is based on simplifying the fundamental equations of all variables to linear model equations. The variables are small variations compared to the mainstream variables. These small variations are the so-called perturbations. The mainstream variables are based on the isothermal rigid body rotation of an ideal gas as derived in the previous section. The following definitions for the perturbations will be used:

$$\begin{aligned} P &= P_s(1+\varepsilon P^{**}) \\ \rho &= \rho_s(1+\varepsilon \rho^{**}) \\ T &= T_0(1+\varepsilon\theta) \end{aligned} \tag{2.32}$$

and the components of $\underline{v}^*$ are:

$$\begin{aligned} v_r^* &= u(r,z) \\ v_\theta^* &= r\omega(r,z) \\ v_z^* &= w(r,z) \end{aligned} \tag{2.33}$$

In eqs. (2.32) $P^{**}, \rho^{**}, \theta$ are the perturbations. P_s, ρ_s and T_0 are the pressure, density and temperature of an ideal gas in a rigid body rotation. This rigid body rotation, as derived in Section 2.1 provides the mainstream values in the linearization of the equations in the following sections. By substituting the perturbations (2.32) - (2.33) in eqs. (2.17) - (2.20) and by discarding higher order terms in ε, a set of first order equations for the variables results.

Axial momentum:

$$0 = -\frac{1}{L}\frac{\partial(P_r^{**})}{\partial z} + E\left[\frac{\partial}{\partial r}\left(\frac{1}{r}\frac{\partial rw}{\partial r}\right) + \frac{1}{L^2}\frac{\partial^2 w}{\partial z^2} + \frac{1}{3L}\frac{\partial}{\partial z}\left(\nabla^*.\underline{v}^*\right)\right] \tag{2.34}$$

Radial momentum:

$$r(\theta - 2\omega)e^{-x} = -\frac{\partial(P_r^{**})}{\partial r} + E\left[\frac{\partial}{\partial r}\left(\frac{1}{r}\frac{\partial ru}{\partial r}\right) + \frac{\partial^2 u}{L^2\partial z^2} + \frac{1}{3}\frac{\partial}{\partial r}\left(\nabla^*.\underline{v}^*\right)\right] \tag{2.35}$$

with

$$\nabla^*.\underline{v}^* = \left[\frac{1}{r}\frac{\partial ru}{\partial r} + \frac{1}{L}\frac{\partial w}{\partial z}\right] \tag{2.36}$$

Angular momentum:

$$\frac{2ue^{-x}}{r} = E\left[\frac{1}{r}\frac{\partial}{\partial r}\left(\frac{1}{r}\frac{\partial r^2\omega}{\partial r}\right)+\frac{1}{L^2}\frac{\partial^2\omega}{\partial z^2}\right] \tag{2.37}$$

Energy conservation:

$$-Bre^{-x}ur = E\left[\frac{1}{r}\frac{\partial}{\partial r}\left(r\frac{\partial\theta}{\partial r}\right)+\frac{1}{L^2}\frac{\partial^2\theta}{\partial z^2}\right] \tag{2.38}$$

Continuity equation:

$$\frac{e^x}{r}\frac{\partial(re^{-x}u)}{\partial r} + \frac{1}{L}\frac{\partial w}{\partial z} = 0 \tag{2.39}$$

The linearised equation of state for an ideal gas:

$$P^{**} = \rho^{**} + \theta \tag{2.40}$$

P_r^{**} is defined by $P_r^{**} = \frac{P_w}{\rho_w \Omega^2 a^2} e^{-x} P^{**}$.

The six equations (2.34) - (2.40) form a full set of equations to calculate the six primary variables $\underline{p}, \underline{\rho}, u, \omega, w, \theta$. The appropriate boundary conditions will be discussed later.

Dickinson and Jones [17], presented a numerical model based on the set of linear equations (2.34) - (2.40). They showed the resulting flow patterns generated by some relatively simple axial anti-symmetrical boundary conditions (meaning that conditions in the top half are the same as in the bottom half but countersigned). Examples of boundary conditions used by them are a linear temperature distribution along the cylinder wall, increased/reduced end caps temperatures and angular velocity at both end caps. Actually these simplifications result in modelling only half a cylinder. They use a discretisation on a staggered mesh and a direct solution method of the resulting set of six linear equations per grid point.

The extensive parameter study as published by Dickinson and Jones [17], confirms in broad terms the agreement between the analytical work of Brouwers [4] and the numerical approach. They show the thickness of the Stewartson layer close to the wall to be somewhat thicker compared to analytical models due to the assumption that the gas pressure is constant in the latter. The development of the Ekman layers is confirmed but there is not much focus on fundamental fluid dynamical aspects like the development of vertical boundary layers along the diffusive core. Furthermore, as mentioned above, the publication does not deal with more complex boundary conditions but only with symmetrical end cap boundary conditions. In real centrifuges symmetry relative to the mid plane hardly exists. Mechanical drive, for example, is applied only one sided, namely at the bottom. The used mesh in this literature is 15 radial grid points and 24 in axial direction, for half a cylinder, so equivalent to 48 for a full model.

2.3 Linear model in the stream function formulation

The equations presented in Section 2.2 can be transformed into a stream function - vorticity model. This description is very useful since the model is two-dimensional, axisymmetrical. For this particular case the stream function can be defined as:

$$\frac{1}{L}\frac{\partial \psi}{\partial z} = -e^{-x} ur \tag{2.41}$$

$$\frac{\partial \psi}{\partial r} = wre^{-x} \tag{2.42}$$

and only the azimuthal component of the vorticity vector, ζ, remains:

$$\zeta r = \frac{\partial w}{\partial r} - \frac{1}{L}\frac{\partial u}{\partial z} \tag{2.43}$$

After a transformation to the radial coordinate *x*, as defined in the previous section, the resulting set of equations is:

$$\frac{1}{L}\frac{\partial}{\partial z}(2\omega - \theta)e^{-x} = E\left[4A^2\frac{\partial^2(1-x/A)\zeta}{\partial x^2} + \frac{1}{L^2}\frac{\partial^2 \zeta}{\partial z^2}\right] \tag{2.44}$$

$$\zeta(1-x/A)\ e^{-x} = 4A^2(1-x/A)e^{-x}\frac{\partial}{\partial x}\left(e^{x}\frac{\partial \psi}{\partial x}\right) + \frac{1}{L^2}\frac{\partial^2 \psi}{\partial z^2} \tag{2.45}$$

$$\frac{Br}{L}\frac{\partial \psi}{\partial z} = E\left[4A^2\frac{\partial}{\partial x}\left((1-x/A)\frac{\partial \theta}{\partial x}\right) + \frac{1}{L^2}\frac{\partial^2 \theta}{\partial z^2}\right] \tag{2.46}$$

$$\frac{-2}{(1-x/A)L}\frac{\partial \psi}{\partial z} = E\left[4A^2\frac{\partial^2(1-x/A)\omega}{\partial x^2} + \frac{1}{L^2}\frac{\partial^2 \omega}{\partial z^2}\right] \tag{2.47}$$

Schroeder and Hanel [23], developed a numerical model based on this set of equations. Not many details are given in this publication nor comparisons with analytical models; it is more a description of the numerical method used to solve iteratively the discrete version of these equations.

The boundary layers along the wall and specifically along the end caps become extremely thin. This is a main challenge and it requires careful attention since they play a major role in determining the flow in the main compartment of the centrifuge. Schroeder and Hanel [23] do not deal in detail with the boundary layers. It is unclear if they put sufficient attention to the Ekman and Stewartson layers with regard to cell size

near the wall and end caps. The paper mentions the refinement of the mesh but does not underpin this with analytical knowledge of the boundary layers. Furthermore, convergence of the iterative procedure was hampered by the nature of the vorticity equation and its boundary conditions. The boundary conditions for the vorticity ζ are expressed in terms of the stream function ψ, as will be discussed later. This results in a very strong coupling between these 2 equations. This complicating issue in the numerical modelling will be discussed in Chapter 4.

One aspect of modern gas centrifuge technology appears by evaluating eq. (2.46) and (2.47). At wall velocities of around 500 m/s, the Brinkman number has a value of about 2, meaning that both equations are fairly symmetrical. Or, in other words, the equations indicate that angular velocity and the temperature are inter-exchangeable. The Brinkman number is about 8 at high wall velocities of $\approx$ 1000 m/s and the equations largely loose this property. This aspect will be studied later in detail in Chapter 6.

The stream function – vorticity, abbreviated as the $\psi - \zeta$ model, fits excellently with the final objective of this study which is the calculation of the flow efficiency E_f and flow strength *m* from eq. (1.6) and (1.7).

2.4 Onsager approach

To calculate the flow in the cylinder, far away from the end caps, Onsager reduced the equations as in Section 2.3 by removing all second-order axial terms. The assumption behind this simplification is that gradients in radial direction are much larger than in axial direction. This assumption holds for length over radius ratios much higher than 1. Furthermore Onsager assumes that the layer of gas next to the cylinder wall is so thin that all algebraic terms in the equations can be neglected. In Appendix B full details how to arrive at the final equation have been given as well as an exact solution for the limiting case of a long centrifuge with a very high wall velocity. The resulting equation is:

$$\frac{\partial^2}{\partial r^2}\left[e^x \frac{\partial^3}{\partial r^3}\left(e^x \frac{\partial \psi}{\partial r}\right)\right] + B^2 \frac{\partial^2 \psi}{\partial z^2} = 0 \tag{2.48}$$

With *B* defined as:

$$B^2 = \frac{(Br+4)}{L^2 E^2} \tag{2.49}$$

Moderate wall velocities result in $Br \approx 1$ and eq. (2.49) can be simplified to:

$$B^2 = \frac{5}{L^2 E^2} \tag{2.50}$$

Eq. (2.48) is called the Onsager equation for a rotating gas at high velocity. Due to the simplifications, Onsager's approach cannot fulfil the end caps boundary conditions.

Near the end caps the axial terms removed during the simplifications are dominating the local flow, resulting in the Ekman boundary layers.

Onsager's model is very popular in North American literature, see e.g. the works of Gunzburger [21], Wood [22], Vicelli [26] and Bourn [27]. They present several models and solution techniques that are based on the Onsager approach. Some early models expand eq. (2.48) into eigenfunctions. Some models use numerical, finite element methods to solve the mathematical problem. Eigenmethods have been used in the 60's by Parker and May [30] and Ging [31]. They produced useful results for centrifuges in the "long" limit. Solutions are mostly based on taking only the first eigenfunction into account, generally speaking under predicting the performance of the centrifuge. This method has serious difficulty in predicting the fine structure of the various boundary layers as present in heavy gas rotating at high angular velocities. More recently the application of finite element methods has overcome most of these limitations, Gunzburger [21].

The Onsager model is quoted here to show how it fits in line with the other models. The simplifications are considered too far reaching and not necessary when state of the art numerical techniques are used, as will be discussed later. The focus in this thesis is on being as complete as possible with respect to the model equations within the linear framework. This linearization is considered very valid based on expected small flows needed inside the centrifuge to produce optimally.

2.5 Analytical models

Work presented by Brouwers [3], [4], [42] from the European centrifuge project and by Matsuda [2], Bark [5], the latter two more academically oriented, are based on boundary layer theories. Stewartson [11] and Greenspan [49] applied the same theories previously in the geophysical context. The discussion in this section is fully based on the work of Brouwers [42], unless otherwise mentioned.

The analytical models focus on the various boundary layers and flow regions as they develop in a rotating gas. Along the end caps, the gas is guided through the thin Ekman layers. Along the wall of the cylinder a Stewartson layer develops. The flow regions and boundary layers have been illustrated in Fig. 2.1.

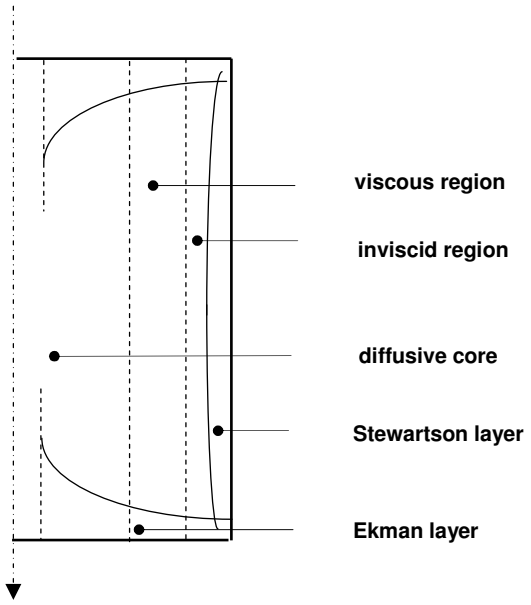

Figure 2.1: Flow regions and boundary layers in a gas centrifuge.

More towards the centre of the centrifuge vertical layers and flow regions might develop depending on boundary conditions and actual flow parameters. The development of these layers is attributed to the exponential decay of the gas pressure towards the axis.

The analytical approach described in this section is very different from the Onsager approach in which sets of eigenfunctions describe the solution. These eigenfunctions often converge very slowly hence many are needed. The boundary layer and flow region approach is based on establishing separate dominating terms in the set of equations for each flow region and subsequently matching of the analytical solutions to each other resulting in a continuous solution for the whole domain.

The analytical approach and the various boundary layers and flow regions will be discussed in more detail in the following sections.

2.5.1 Flow regions

Brouwers [42] defines somewhat different dimensionless parameters, variables and numbers compared to the set as discussed before:

$$Lm = LA$$

$$Em = EA^2$$

$$u = -\frac{v_w ar}{l\rho A}\frac{\partial}{\partial z}(\rho\psi_b)$$
$$w = \frac{v_w}{\rho rA}\frac{\partial}{\partial r}\left(\rho r^2\psi_b\right) \qquad (2.51)$$

Brouwers derives the following set of equations applying a perturbation method as summarized in Section 2.2. The set of equations is not fully identical with the set as given in Section 2.3, see for details Appendix A.

Stream function equation:

$$\frac{\partial}{\partial z}(2\omega-\theta) =$$
$$LmEm\left[\left\{4\frac{\partial}{\partial x}e^x\frac{\partial}{\partial x}(1-x/A) + L^{-2}e^x\frac{\partial^2}{\partial z^2}\right\}^2 - \frac{4}{3}\left\{2AL^{-1}e^x r^2\frac{\partial}{\partial z}\right\}\right](e^{-x}\psi_b) \qquad (2.52)$$

Angular velocity equation:

$$LmEm\left[4\frac{\partial^2(1-x/A)\omega}{\partial x^2} + \frac{1}{L^2}\frac{\partial^2\omega}{\partial z^2}\right] = -2e^{-x}\frac{\partial\psi_b}{\partial z} \qquad (2.53)$$

Temperature equation:

$$LmEm\left[4\frac{\partial}{\partial x}\left((1-x/A)\frac{\partial\theta}{\partial x}\right) + \frac{1}{L^2}\frac{\partial^2\theta}{\partial z^2}\right] = (1-x/A)Bre^{-x}\frac{\partial\psi_b}{\partial z} \qquad (2.54)$$

For x close to 0, at the rotating cylinder wall, the coupling via the term at the right hand side of (2.53) and (2.54) is maximal. The coupling reduces exponentially with x.

Brouwers defines two flow region:

- an inviscid flow region between the Stewartson layer and *x* derived from

$$\frac{e^{-x_i}}{Lm^{2}\,Em} = 1 \tag{2.55}$$

- a viscous flow region between the *x* value derived in eq. (2.55) and the *x* value derived from

$$\frac{e^{-x_c}}{LmEm} = 1 \tag{2.56}$$

Both radial locations will be referred to later in this thesis as:

- the location of the inviscid core: $x = x_i$

- the viscous core: $x = x_c$

Obviously there is not a sharp division between one flow region and the other. Full solutions could not always be reached as will be discussed later in this chapter. The flow regions fit to the Ekman layers at both end caps.

For values of $x > x_c$ the equations become uncoupled and the domain is fully diffusive.

The development and existence of the different flow regions depends on the actual values of Em and Lm. Depending on these parameters given by velocity, wall pressure, length and radius of the cylinder three different centrifuge domains can be defined:

- "*Short*", if $1 < Lm < 1/\sqrt{Em}$. In this parameter range both an inviscid and viscous region develop

- "*Semi-long*", if $1/\sqrt{Em} \cong Lm < 1/Em$. Only a viscous region develops

- "*Long*", if $Lm > 1/Em$. There is only diffusive flow outside the Stewartson layers

These domains will be referred to later in this thesis by simply stating: "*Short*", "*Semi-long*" and "*Long*" centrifuges.

2.5.2 Stewartson layers

In rotating systems boundary layers along fixed walls develop. They were firstly analysed by Stewartson [11, [12]. Further analysis by Bark [5], Brouwers [3], [4], [42] and Matsuda [2] shows that two layers inside each other develop, the outer one with thickness O($Lm^{1/2}Em^{1/4}$) bringing the angular velocity and temperature from the values in the main compartment of the cylinder down to the wall values. The inner layer brings the stream function down to zero in a layer with a typical thickness O($Lm^{1/3}Em^{1/3}$) at mid plane (*z = 0.5*). Towards the corners with the end caps, the thickness is considerably reduced to O($Em^{1/2}$) where they fit to the Ekman layers.

The density is taken as constant in these analytical models. This assumption is only valid if the layers are thin compared to the scale at which the density reduces. This might not always be the case, according to Matsuda [2] and Brouwers [3], the thickness of the Stewartson layers is not always small compared to the scale at which the density decays.

The actual thickness of the Stewartson boundary layers is very thin, typically of the order of 0.5 mm, depending on the actual centrifuge parameters**.**

When a dimensionless temperature gradient of two is applied at the wall of the cylinder ($\nabla\theta = 2$), a strong flow develops inside the inner Stewartson layer. Brouwers [3] shows that the stream function in this layer can be estimated by:

$$\psi = \frac{1}{4}(LE)^{1/3} e^{-x} /(1+1/4Br) \tag{2.57}$$

and a thickness

$$x_s = O(A(LE)^{1/3}) \tag{2.58}$$

x_s Is the scaling factor for this boundary layer. The approximate solution of the Stewartson layer, as derived by Brouwers [3] indicates that the actual thickness of the Stewartson layer is $\approx 3\,x_s$.

2.5.3 Ekman layers

The Ekman layers are boundary layers along the end caps. In the layer at the top, gas is guided towards the corner of the end cap and cylinder wall. In the layer at the bottom, gas is guided from the corner of the cylinder wall and bottom end cap into the main compartment.

Further analysis by Brouwers [42] shows that the typical thickness of the Ekman layer in a compressible fluid is O($Lm^{-1}\ (Eme^{x})^{1/2}$). The expansion when moving towards the centre line (higher values of x) is due to the decreasing density. The stream function has a value O($(Eme^{-x})^{1/2}$).

Limited heat transfer at the end caps affects the Ekman layers strongly, as can be seen in Bark [5] and Matsuda [18]. It results in sub-optimally conditioned temperature of the gas in the Ekman boundary layer close to the end caps. This results in a reduced suction and consequently in a reduced gas flow through the main compartment.

Near the corner of cylinder wall and end cap, Ekman layers can become a few orders of magnitude thinner than the Stewartson layers. In terms of the dimensionless length, the Ekman layer can become of order of $\approx\ 10^{-6}$. This forms a challenge in the numerical approach. The thickness at the corner between cylinder wall and end cap is in physical dimensions the same as the thickness of the Stewartson layer at this location.

Further inwards the Ekman layer expands and joins the inner core regime where all flow is determined by diffusive behaviour. This happens for *x* values: $e^{x} > 1/Em$. The corresponding radial position along the x axis where $e^{x} = 1/Em$, will be referred to later in this thesis as $x = x_d$ with a corresponding thickness of the Ekman layer at this location:

$$\delta \sim 1/Lm$$

The Ekman layers generate suction or pumping effects, resulting in a flow through the main compartment of the gas centrifuge. The suction or pumping can be achieved by applying:

- a temperature difference at the end cap
- an angular velocity difference at the end cap
- injection / withdrawing gas at the end caps.

According to Brouwers [42], the combined suction effect of the temperature and angular velocity differences at the bottom and top end cap $F_b(x)$ and $F_t(x)$, can be expressed as:

- at *z = 0*, $F_b(x) = \omega_b(x) - \frac{1}{2}\theta_b(x)$
- at *z = 1*, $F_t(x) = \omega_t(x) - \frac{1}{2}\theta_t(x)$ (2.59)

Here $\omega_b(x)$ and $\omega_t(x)$ are the perturbations of the angular velocity at the bottom and top end cap, $\theta_b(x)$ and $\theta_t(x)$ the temperature at these locations.

Gas injection or withdrawal is not relevant for our application and not included in relation (2.59).

2.5.4 Calculating the flow efficiency

Applying the Ekman suction conditions to the various flow regions, as discussed in Section 2.5.3, Brouwers [42], finds the following results for the stream function outside the Ekman layer:

For the stream function in the inviscid area, between the Stewartson layer near the wall and $x = x_i$, as defined in eq. (2.55):

$$\psi = \frac{1}{4}(1-x/A)/(1+1/4Br(1-x/A))^{3/4}(Ee^{-x})^{1/2}(F_t - F_b) \tag{2.60}$$

There is no *z* dependence; this result indicates a constant flow from bottom to top.

For the viscous area between $x = x_{ic}$ and $x = x_c$, as defined in eq. (2.56):

$$\psi = \frac{1}{2}(1-x/A)/(1+1/4Br(1-x/A))^{3/4}(Ee^{-x})^{1/2}(z(F_b + F_t) - F_b) \tag{2.61}$$

This result indicates a linearly decaying flow from bottom to top. It is important to notice that if $F_t = -F_b$, then eqs. (2.60) and (2.61) result in exactly the same flow. This means that the viscous and inviscid regions behave the same as one integrated inviscid region.

These results will be used later in this thesis to verify the numerical model. The condition $F_t = -F_b$, will be referred to as anti symmetrical Ekman conditions.

In the core area a simple decaying radial profile of the stream function can be found. The problem is the transition area between the viscous area and the diffusive core. Furthermore this transition layer touches on the Ekman layers at the bottom and top end cap. For the calculation of the flow efficiency and flow strength as discussed in Chapter1, Section 1.4, this area is relevant. It contributes considerably to the overall flow in the main compartment of the gas centrifuge and to the flow efficiency factor.

Brouwers [42] derives an approximating solution applying a Pohlhausen method; the solution is valid for only specific sets of boundary conditions at the end caps.

The maximum flow efficiency can be achieved (at least theoretically) by selecting "Ideal" suction conditions for F_b and F_t in eq. (2.60) and eq. (2.61). These ideal conditions are:

$$F_t = -F_b = 2(1+1/4Br(1-x/A))^{3/4}(LEe^{x})^{1/2} \tag{2.62}$$

Further in this thesis, a boundary condition like eq. (2.62) with:

$$F_t = -F_b \sim (1+1/4Br(1-x/A))^{3/4}(e^x)^{1/2} \tag{2.63}$$

will be referred to as `Ideal Ekman conditions` or abbreviated as "*IBC*". If the Ideal Ekman suction condition is applied one-sided, meaning only at the top or bottom end cap then it will be abbreviated as "*Semi-IBC*".

Eqs. (2.62) and (2.63) implicate that the Ekman suction needs compensation towards the centreline to be equally effective along the radius. This compensation is required since the decreasing gas density results in an increasing thickness of the Ekman boundary layer. The actual compensation is increase of the temperature (or reducing the angular velocity) along the end cap at the bottom. The conditions at the top end cap should be inversely set: decreasing the temperature (or increase the angular velocity) towards the centreline. As a whole, the local suctions along the caps are now constant as can be seen by applying condition (2.62) to eq. (2.60) or eq. (2.61), resulting in:

$$\psi \sim (1-x/A) \tag{2.64}$$

This is the ideal profile as discussed in Chapter 1: a constant mass flow per area generated over an as large as possible area of the cross section. However this is only at the very bottom and top of the cylinder. Fluid dynamic behaviour away from the end caps in the main compartment of the cylinder might limit the ideal profile in this part of the centrifuge, which is exactly the reason why a fluid dynamic model is needed.

Brouwers [42] applies the approximating results for the Stewartson layer, for the inviscid and viscous transition layers and for the diffusive core to calculate the flow efficiency factor. This model is a very pragmatic tool for strategic studies in gas centrifuge design. This analytical model will be used as a benchmark for the results of the numerical model as will be developed in the coming chapters.

2.5.5 Discussion of fluid dynamic models

In the previous sections the full spectrum of mathematical models applicable to the fluid dynamics in a fast rotating cylinder has been reviewed, from analytical approximating solutions to full Navier Stokes solvers. As mentioned in Chapter 1 and reconfirmed by previous numerical studies, the optimal performance of a gas centrifuge is reached when only a relatively small amount of gas is flowing through the centrifuge. This allows for linearization of the equations. Furthermore the description in terms of ψ - ζ fits very well with the application of these models since the final wish is to calculate the flow efficiency and flow strength and these parameters are directly based on the stream function. In other words: to calculate these two parameters the stream function should be known. There is no direct need to have the primary variables available. The analytical work of Brouwers [42] is an excellent benchmark to test the final model, reversely the numerical model can be used to check some of the approximations in this model to increase the understanding of the gas flow in a fast

rotating cylinder. This is specifically applicable to the transition layer between the viscous flow region and the diffusive core, where insight in both the radial and axial profile of the stream function can be advanced.

The set of equations as given in Section 2.3 form a set of four non-linearly coupled partial differential equations of elliptic type. Incorporation of boundary conditions is straightforward. This set, as derived in full detail in Appendix A, is identical with the equations used by Dickinson and Jones [17] and Schroeder and Hanel [23].

It is relevant to discuss the presently derived model relative to Onsager's model as discussed in the previous section. Onsager's equation results from the present set by elimination of axial diffusion, algebraic terms in the radial coordinate and by resolving the end cap issues by incorporating Ekman boundary suction analytical solutions. The resulting equation is a 6^{th} order problem, where the full set of linear equations can be considered as an 8^{th} order problem. Although Onsager's approach is a very elegant one, the model equations of Section 2.3 have some additional advantages:

- the 8^{th} order approach does not complicate the solution as mentioned before. Accurate and stable solution methodologies can be developed for these elliptic partial differential equations
- inclusion of the various boundary values is more transparent and straightforward
- solution of the full set will automatically include full resolution of the Ekman and Stewartson boundary layers
- a main challenge is the resolution of the Ekman boundary layers. The extremely thin layers ($\sim 10^{-6}$ of the length of a centrifuge) need careful attention since they play a major role in determining the flow in the main compartment of the centrifuge
- including the algebraic terms is not a complication and even necessary to study some fluid dynamic behaviour in the Short domain.

As mentioned in Section 2.4, the classical Onsager approach is to develop a solution by combining eigenfunctions. This has proven to be a difficult task as is illustrated in the analytical work by Brouwers [42]. To resolve the gas flow pattern sufficient accurate, a very high number of eigenfunctions has to be included in the solution. Otherwise inaccurate and misleading results are produced. This is especially the case in the centrifuge parameter range for which various flow regions exist in parallel (viscous region, diffusive core), as is the case for the Semi Long domain. It is a less obvious problem in the parameter range for which radial effects fully dominate in a single flow region, as is the case in the Long domain where only a single or a few eigenfunctions are needed to describe the flow sufficiently.
In European literature based on the boundary layer and flow region approach, Brouwers [42], specific analytical solutions are developed per flow region by focussing on dominating terms in the set of equations. By applying this style of analytical modelling the insight is gained that a considerable increase in flow efficiency can be achieved relative to Long centrifuges by realising a viscous region as in the Semi Long centrifuge. In practice this can be achieved by increasing the gas pressure, resulting in a lower Ekman number. Obviously appropriate end cap boundary conditions have to be

applied to utilise this potential. This view on centrifuge design points at smaller, shorter and high performing (from a flow efficiency point of view) centrifuges versus centrifuges operating in the Long domain.

2.6 Problem definition

Many design and engineering parameters are being evaluated during strategic studies in overall separation plant design. An accurate model, easy and quick to use, is needed to verify the impact of those parameters on the characteristics of the individual centrifuge, since overall design of a separation plant depends strongly on the performance of the individual centrifuge. Once the main features of a centrifuge have been frozen, more detailed engineering issues have to be evaluated. Materials have to be chosen for some critical parts of the centrifuge as e.g. for the cylinder wall and the end caps. Some of the properties of these materials influence the performance of the centrifuge. Thermal properties of materials used for the end caps are such a property and it is a requirement of the model to enable modelling these details.

Separation theory shows that the performance of the centrifuge is strongly depending on the fine structure of vertical boundary layers developing in a heavy gas rotating at high angular velocities. Both the shape of the stream function and the strength of this internal flow are important. The overall mass flow of this internal flow can be manipulated by tuning parameters like temperature gradient, end cap temperature and mechanical drive performance. The shape of the stream function is strongly depending on fundamental engineering parameters and it needs an in-depth study how these parameters influence the shape and strength of the stream function. Detailed and computationally efficient modelling is required to quickly establish an overall view of important parameters. For this purpose a software package has been developed based on the following argumentation from a mathematical point of view:

- the use of full Navier Stokes solutions for this application is considered not necessary, therefore the final model will be based on linearised equations
- flow efficiency (E_f) and flow strength (m) are calculated from the stream function. This suggests to developed the model on the basis of the stream function formulation and not on the basis of the primary variables
- a major modelling challenge is the extremely thin Ekman layers and to a somewhat lesser extent the thin Stewartson layers. Dedicated efforts will be put in place to resolve these layers
- straightforward iterative schemes are hampered by the nature of the problem: the internal circulation and the coupling in boundary values of the $\psi - \zeta$ model. A stable numerical method will be developed to reach convergence of this set of equations.

The following considerations are taken into account from an overall model point of view:

- flow efficiency (E_f) and flow strength (m) as defined in Section 1.4 will be used as the main trackers to quantify the separation performance of a centrifuge
- the model will be designed to allow for a wide range of non symmetrical boundary conditions to enable simulation of practical situations
- some studies indicate that thermal properties of the end caps and cylinder wall material as well as the heat transfer by radiation to the environment can play an important role in the resulting internal flow field. Therefore the model will allow evaluation of these properties on the centrifuge performance.

In Chapter 5, 6 and 7 simulations will be reported utilising the model to increase the understanding in the following areas:

- the structure of the vertical boundary layers as predicted by analytical works e.g. Brouwers [3]
- the effect of very high velocities, > 750 m/s, on the resulting flow
- the effect of not axial symmetrical boundary conditions on E_f and *m*
- the influence of the thermal properties of the cylinder wall and end caps on E_f and *m.*

Chapter 3

The centrifuge model

Summary

The model centrifuge that will be developed is a rotating cylinder with closed end caps. The bottom end cap is allowed to rotate as a whole at a different angular velocity compared to the cylinder, thereby inducing the internal closed circulation as discussed in Chapter 1. The thermal conditions will impact the internal flow and the model will be designed to simulate these effects. The final model is a set of four nonlinear coupled partial differential equations of the elliptic type. In this chapter boundary conditions for these equations will be discussed. In Fig. 3.1 a schematic overview of the model and its boundary conditions is given.

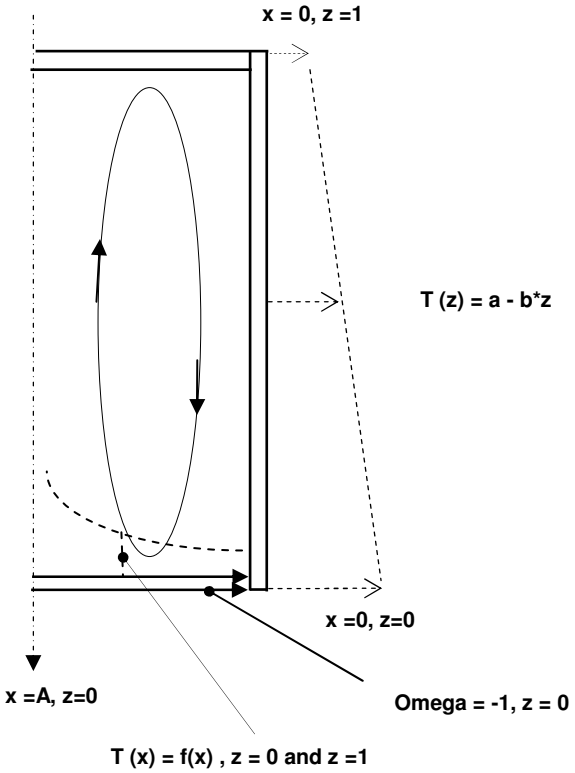

Figure 3.1: Centrifuge model indicating the domain and some boundary conditions.

The resulting model in this chapter is the basis for the numerical model that will be presented in Chapter 4.

3.1 Stream function boundary conditions

The stream function equation eq. (2.45), is formulated as:

$$\zeta(1-x/A)\ e^{-x} = 4A^2(1-x/A)e^{-x}\frac{\partial}{\partial x}\left(e^{x}\frac{\partial \psi}{\partial x}\right)+\frac{1}{L^2}\frac{\partial^2 \psi}{\partial z^2} \tag{3.1}$$

In the absence of sinks or sources of gas, the boundary value of the stream function is constant and to be set arbitrarily along the boundary of the domain. Here a value zero will be used:

$$\begin{aligned} &\psi = 0,\ 0 \le z \le 1; \quad x = A, x = 0 \\ &\psi = 0,\ 0 < x < A; \quad z = 0, z = 1 \end{aligned} \tag{3.2}$$

The equation for ψ is now fully defined. However, an extra set of boundary values is to be set for ψ, since the actual velocities at the cylinder wall, end caps and at the centreline are defined by this equation as well. This follows from it's definition, given in eq. (2.41) and eq. (2.42):

$$\frac{1}{L}\frac{\partial \psi}{\partial z} = -e^{-x}ur \tag{3.3}$$

$$\frac{\partial \psi}{\partial r} = wre^{-x} \tag{3.4}$$

Furthermore along the centre line, radial symmetry is applicable, resulting in:

$$\frac{\partial w}{\partial r} = 0\ ,\ 0 \le z \le 1;\ x = A \tag{3.5}$$

3.2 Vorticity boundary conditions

The elliptic eq. (3.1) can only partly satisfy all required boundary conditions eq. (3.2) to eq. (3.5). By selecting the boundary conditions for the vorticity equation in line with the extra conditions for ψ, both equations can be specified and all conditions can be satisfied.

Recalling the equation for the azimuthal component of the vorticity, eq. (2.44):

$$\frac{\partial}{L\partial z}(2\omega-\theta)e^{-x} = E\left[4A^2\frac{\partial^2(1-x/A)\zeta}{\partial x^2}+\frac{1}{L^2}\frac{\partial^2 \zeta}{\partial z^2}\right] \tag{3.6}$$

The definition of vorticity, (A66):

$$\xi\frac{a}{V_w} = \zeta r = \frac{\partial w}{\partial r}-\frac{1}{L}\frac{\partial u}{\partial z} \tag{3.7}$$

Eq. (3.7) shows that condition (3.5), radial symmetrical condition for the axial velocity w along the centreline, will be fulfilled by setting the vorticity at the centreline to zero since the radial velocity component u is zero all along the full length of the centreline. This results in:

$$\zeta = 0,\ 0 \le z \le 1;\quad x = A \tag{3.8}$$

Eq. (3.7) dictates as well that the vorticity should be zero in the corners between the rotating wall and both end caps since both derivatives are zero at these locations:

$$\zeta = 0.\ z = 1,\ z = 0\ ;\ x = 0 \tag{3.9}$$

At the rotating wall the boundary condition for vorticity can be calculated from eq. (3.1), substituting (3.2) and combining it with (3.5):

$$\zeta = 4A^2 \frac{\partial}{\partial x}\left(e^x \frac{\partial \psi}{\partial x} \right),\ \frac{\partial \psi}{\partial x} = 0\ ;\ 0 < z < 1; x = 0 \tag{3.10}$$

From the same equations and condition, a boundary condition for vorticity at both end caps can be found:

$$\zeta (1 - x/A)\ e^{-x} = \frac{1}{L^2} \frac{\partial^2 \psi}{\partial z^2},\ \frac{\partial \psi}{\partial z} = 0\ ;\ 0 < x < A; z = 0, z = 1 \tag{3.11}$$

Conditions (3.8) to (3.11) define fully and fulfil as well the extra conditions as set for the stream function equation in the previous section.

Schroeder and Hanel [23] refer to the set of equations (3.10) and (3.11) to be the causes for slow convergence in the numerical approach. In the next chapter a method will be developed and explained which eliminates this problem of slow convergence.

3.3 Temperature boundary conditions

The resulting equation for the temperature is given in eq. (2.46):

$$\frac{Br}{L} \frac{\partial \psi}{\partial z} = E\left[4A^2 \frac{\partial}{\partial x}\left((1 - x/A) \frac{\partial \theta}{\partial x} \right) + \frac{1}{L^2} \frac{\partial^2 \theta}{\partial z^2} \right] \tag{3.12}$$

Radial symmetry at the centreline along the length of the cylinder results in the condition:

$$\frac{\partial \theta}{\partial x} = 0\ ,\ 0 \le z \le 1;\quad x = A \tag{3.13}$$

The thermal model for the end caps and the cylinder wall defines the boundary conditions for the temperature along these elements of the centrifuge. For all three elements a formulation has to be developed including heat conduction in the material in the direction of the element, heat transfer by radiation to the surroundings and conduction of heat at the inside of the element, meaning energy transfer from the gas flowing along the surface to the material of the end cap/wall. Heat transfer by radiation will be the main transport phenomena to the surroundings since the cylinder has to turn in an almost perfect vacuum to prevent both material damage and/or excessive energy consumption due to friction. This model assumes that the wall and end caps are thin and well conducting, resulting in no temperature difference over the wall thickness.

The general equation governing the resulting phenomena reads:

$$\lambda_w \delta_w \frac{\partial^2 T}{\partial \eta^2} = -\lambda_g \left.\frac{\partial T_g}{\partial \xi}\right|_{wall} + h_s (T - T_s) \tag{3.14}$$

The left side of eq. (3.14) represents conduction of heat in the wall and the two terms on the right represents the conduction from the gas to the wall and the linearised radiation of heat from the wall to the surrounding. η and ξ are here arbitrarily chosen coordinates. η Is the coordinate along the wall and ξ is perpendicular to it. T_g is the gas temperature inside the cylinder, T_s the temperature on distance from the surrounding, h_s is the heat radiation coefficient in W/m^2K and δ_w the thickness of the wall. λ_w, λ_g are the heat conductivity coefficients of the wall material and of the gas in W/mK.

During the parameter studies the wall thickness and heat conductivity will be varied to analyse how this influences the overall flow efficiency (E_f). Modern materials like carbon fibres have very different (lower) heat conductivity $\lambda \approx 35\ W/mK$ compared to more classical materials like aluminium $\lambda \approx 300\ W/mK$.

Eq. (3.14) will be fully included in the numerical model.

For both end caps eq. (3.14) needs to be transformed into cylindrical coordinates:

$$\lambda_w \delta_w \frac{1}{r}\frac{\partial}{\partial r}\left(r \frac{\partial T}{\partial r} \right) = -\lambda_g \left.\frac{\partial T_g}{\partial z}\right|_{endcap} + h_s (T - T_s) \tag{3.15}$$

In terms of the dimensionless variables, as introduced in Section 2.1.1 and Section 2.1.2, equation 3.15 reads:

$$4A^2 \frac{\lambda_w \delta_w}{\lambda_g a} \frac{\partial}{\partial x}\left[(1-x/A)\frac{\partial \theta}{\partial x}\right] = -\frac{1}{L}\frac{\partial \theta_g}{\partial z}\bigg|_{endcap} + \frac{h_s a}{\lambda_g}(\theta - \theta_s) \qquad (3.16)$$

Eq. (3.16) will be used in the numerical models presented in Chapter 4.

The thermal model is coupled via the heat radiation transfer coefficient h_s to the thermal conditions outside the rotating cylinder, the enclosing container. By changing the temperature of these container walls and end caps, the wall temperature of the rotating cylinder as well as the temperature of the end caps can be changed. Examples are: a constant temperature along the end caps or a linearly varying temperature along the wall of the container as well as more complex conditions and profiles. They will be discussed later when actual numerical calculations are performed.

In Chapter 5 the fluid dynamics of a heavy gas in a fast rotating cylinder subjected to given thermal conditions at the wall and end caps will be studied. This is achieved by applying an artificially high heat transfer coefficient and low heat conductivity coefficient. This effectively results in specified temperatures at the wall and end caps of the rotating cylinder.

In Chapter 7 realistic values are used for the heat transfer coefficients and thermal properties of the wall and end caps to study how they influence the fluid dynamics.

3.4 Angular velocity boundary conditions

The equation for the angular velocity, eq. (2.47) reads:

$$\frac{-2}{(1-x/A)L}\frac{\partial \psi}{\partial z} = E\left[4A^2 \frac{\partial^2 (1-x/A)\omega}{\partial x^2} + \frac{1}{L^2}\frac{\partial^2 \omega}{\partial z^2}\right] \qquad (3.17)$$

The boundary conditions for the angular velocity at the rotating wall and top end cap are set to no slip conditions:

- at the wall $\omega = 0$, $0 \le z \le 1$; $x = 0$ (3.18)
- at the top end cap $\omega = 0$, $0 < x < A$; $z = 1$ (3.19)
- radial symmetry at the centre line results in

$$\frac{\partial \omega}{\partial x} = 0, \quad 0 \le z \le 1; \; x = A \qquad (3.20)$$

At the bottom end cap the gas can be slowed down by inserting a scoop in the gas or by other mechanical means. It is assumed that three-dimensional effects can be discarded.

The resulting boundary condition at the bottom end cap, as shown in Fig. 3.1:

- $\omega = -1$, $0 < x < A;\ z = 0$ (3.21)

Conditions (3.18) to (3.21) are sufficient boundary conditions to resolve eq. (3.17).

3.5 Modelling of boundary conditions

There are three different driving mechanisms for the internal flow:

- by realising a temperature difference between the top and bottom end cap. A simple driving mechanism is formed by having uniform, but different temperatures at the end caps of the cylinder ($\Delta\theta$ between top and bottom end caps). However, as has been discussed in Section 2.5, more complex temperature profiles (IBC or Semi-IBC) along the bottom and/or top end cap will result in higher flow efficiencies, see eq. (2.63)
- a temperature gradient along the cylinder wall
- the internal flow can be driven by mechanical means at the bottom end. This is modelled by a reduced angular velocity at this location.

A combination of these driving mechanisms can be applied as well. In the model the temperature boundary conditions are realised by specifying the dimensionless temperature θ for the environment along the end caps and cylinder wall. The actual temperature condition at the end caps and cylinder wall is realised via the heat transfer coefficients between the environment and the various elements of the rotating cylinder, eq. (3.16). If these heat transfer coefficients are sufficiently high, then the temperatures at the end caps and wall are the same as for the environment.

The flow efficiency (E_f) eqs. (1.6) and (A91) is independent of the absolute values of the stream function ψ and therefore independent of the Rossby number eq. (2.14). The flow strength (*m),* eqs. (1.7) and (A92), varies linearly with the Rossby number. Therefore eq. (A92) can be used to determine the absolute values of the Rossby number, subject to a given absolute value of *m*. Subsequently the absolute temperatures or angular velocity disturbances applied to drive the internal flow can be calculated using the definition of the Rossby number eq. (2.14). In the next chapters the intrinsic flow strength *m** will be reported as defined by eq. (A94):

$$m = \varepsilon\ m^* \qquad [-] \qquad (3.22)$$

Chapter 4

Numerical modelling

Summary

In this chapter the numerical method to resolve the model equations derived in Chapter 2 and Appendix A will be presented. In separate sections, the various aspects of the numerical method are explained:

- in Section 4.1 and 4.2, the transformation of the model equations to nonlinear coordinates will be explained
- in Section 4.3, the staggered mesh used to represent the discrete version of these equations is introduced
- Section 4.4 and 4.5, demonstrate the discretisation technique and matrix resolution.

Subsequently in Section 4.6, test results are provided by applying two different parameter sets, proving the validly of the approach by comparing calculated results with analytical models. In Section 4.7 the accuracy and convergence with increasing number of axial and radial grid points is reported and the convergence rate of the iterative scheme is discussed. Evidence that the model fulfils the boundary conditions as specified, is given in Section 4.8. Conclusions on the numerical modelling are given in Section 4.9.

The numerical approach is a direct integration of the four nonlinearly coupled partial differential equations applying finite discretisation on a staggered mesh. Challenges in this discretisation process are the extremely thin boundary layers; specifically the Ekman layers along the end caps and to some extent the Stewartson layers along the cylinder wall. The equations will be transformed to new coordinates both for x and z enabling to resolve boundary layers accurately. These transformations, specifically designed for this application and based on analytical knowledge of the underlying physics, will be presented. The fundamentals of this approach and mathematical methodology are based on the work of Kalnay De Rivas [41].

Another challenge is to achieve fast convergence. This is hampered by the coupling between the vorticity and stream function equations via the boundary values for the vorticity. An iteration scheme will be presented eliminating this issue. The philosophy behind this iteration scheme is:

The matrix resulting from the discretisation of the equations will be split into individual smaller matrices all representing a strip of cells; each strip consists of a number of radial cells but covers the full length of the cylinder. These individual sub matrices will be resolved by a direct method; LU decomposition. The results are immediately used as boundary values for the next, adjacent strip, until all sub matrices are solved. This is repeated until the convergence criterion has been reached. This eliminates the

convergence problem almost perfectly since all boundary values are constantly fully implicitly incorporated in the solution.

From a numerical accuracy point of view, maximal attention is paid to maintain second order spatial accuracy. This results in limited computational efforts making it possible to quickly and easily perform many computations to optimise a configuration.

The velocity parameter (*A)* reaches values between 15 and 75. This results in extremely low levels of local pressure and density towards the centreline. In order to maintain a constant mass flow per cross sectional area, Section 1.3, the low pressure towards the centre line has to be compensated by increasing the local axial gas velocity. However, it is unlikely that this low pressure can be compensated at high values of the radial coordinate *x*, which results in a diminishing gas flow in axial direction towards the centre of the centrifuge. Therefore not the full domain of the radial coordinate will be considered in the calculations but the domain will be limited to a fictitious centreline. For most applications the fictitious centreline will be positioned at $x = x_{cl} \sim 12$, meaning that the local density is e^{-12} of the wall density. The local density at this location is so low that it does not contribute to the mass transport in the centrifuge.

The flow efficiency (E_f), eq. (A92), is used to determine convergence of the algorithm. This parameter varies along the length of the centrifuge; therefore the averaged value will be calculated.

4.1 Transformation to stretched coordinates

In this chapter only the transformation for the vorticity equation will be presented. Details about the remaining three equations can be found in Appendix C.

The equation for vorticity is given by eq. (3.6):

$$\frac{1}{L}\frac{\partial}{\partial z}(2\omega-\theta)e^{-x} = E\left[4A^2\frac{\partial^2(1-x/A)\zeta}{\partial x^2}+\frac{1}{L^2}\frac{\partial^2\zeta}{\partial z^2}\right] \tag{4.1}$$

The new, stretched coordinates are defined as η and ξ:

$$\eta = \eta(x) \text{ and } \xi = \xi(z)$$

Applying these new coordinates, then Eq. (4.1) results in:

$$\frac{1}{L}\frac{d\xi}{dz}\frac{\partial}{\partial\xi}(2\omega-\theta)e^{-x} = E\left[4A^2\frac{d\eta}{dx}\frac{\partial}{\partial\eta}\left(\frac{d\eta}{dx}\frac{\partial(1-x/A)\zeta}{\partial\eta}\right)+\frac{1}{L^2}\frac{d\xi}{dz}\frac{\partial}{\partial\xi}\left(\frac{d\xi}{dz}\frac{\partial\zeta}{\partial\xi}\right)\right] \tag{4.2}$$

The functions $\eta = \eta(x)$ and $\xi = \xi(z)$ are chosen such that they stretch the coordinates *x* and z in the boundary layers. This is realised by selecting analytical mathematical functions with high derivatives close to the end caps and wall. The functions are smooth, to prevent unwanted sharp transitions which would disturb the numerical process.

Because of the effect that these functions have on the coordinates they are referred to as stretching functions.

Knowledge from analytical boundary layer theories is used to define the final set of stretching equations and parameters.

4.2 Designing the stretching functions

A first challenge in selecting a stretching function for the axial coordinate is that the Ekman boundary layers along the end caps expand towards the (fictitious) centreline as:

$$\delta(x) \sim L^{-1}(Ee^{x})^{1/2}$$

This relation indicates that the Ekman layer is expanding an order of magnitude in thickness between $x = 0$ and a fictitious centreline at e.g. $x = 12$. A single stretching function is deemed to be insufficient to deal with these different thicknesses. Therefore three stretching functions are applied of the same type but with different parameters to resolve the equations accurately close to the end caps where the Ekman layers develop. The parameters for the functions are calculated from the analytical estimates of the thickness of the Ekman layer at x = 0, at the fictitious centreline and halfway the fictitious centreline. This is still extremely thin compared to the overall length of the cylinder therefore two more stretching functions are applied to stretch the grid smoothly to cover the full length of the cylinder. These two functions again are of the same type. The parameters used for these functions are given in Section 4.2.1.

The stretching of the radial coordinate is somewhat easier since the Stewartson layers do vary in thickness along the height of the cylinder, but much less dramatically compared to the varying thickness of the Ekman layers at the end caps. The stretching for the *x* coordinate will be explained in Section 4.2.2. The same type of stretching functions will be used as for the axial coordinate, three functions prove to be sufficient for this problem. Parameters are selected utilising analytical estimates of the thickness of these layers.

4.2.1 Stretching functions for the z coordinate

In the model a series of exponential functions is used to transform both the *x* and *z* coordinates:

$$\xi = \xi(z) \text{ and } \frac{d\xi}{dz} = \gamma_z + \sum_{k=1}^{k=5} \alpha_k \beta_k e^{-\beta_k z} \tag{4.3}$$

The same transformation is used near the top end cap at *z* = 1 where a similar boundary layer develops.

The coefficients α and β are being set in such a way that they fit the respective scale of the Ekman boundary layer, the set of values calculated from the analytical theory is used as the default set:

- β_1 is determined from the relation $\beta_1 = \frac{2}{3\delta_0}$ with $\delta_0 = L^{-1}E^{1/2}$
- β_2 is determined from the Ekman layer thickness in the middle of the radial domain at $x = 0.5x_{cl;}$, $\beta_2 = \frac{2}{3\delta_c}$ with $\delta_c = L^{-1}(Ee^{0.5x_{cl}})^{1/2}$
- β_3 follows from the Ekman layer thickness at the centreline of the radial domain at $x = x_{cl}$, $\beta_3 = \frac{2}{3\delta_c}$ with $\delta_c = L^{-1}(Ee^{x_{cl}})^{1/2}$
- $\beta_4 = \beta_3 / 10$
- $\beta_5 = \beta_4 / 10$

The values for α_k represent the fraction of the axial coordinate to be compressed by the transformation. For $k = 1$ to $k = 4$ values of 0.05 are used, for $k = 5$ a value of 0.15. By selecting these parameters as presented some 10% of the axial coordinate *z* is stretched to 35% of the new scale ξ and about 1% at the scale of *z* is stretched to a fraction of some 20% at the scale of ξ. An example of these transformations is given in Appendix D.

4.2.2 Stretching functions for the x coordinate

For the transformation of *x*, the same approach is followed as for the *z* coordinate. The Stewartson boundary layer thickness, as discussed in Section 2.2.3, will be used to calculate the parameters:

$$\eta = \eta(x) \text{ and } \frac{d\eta}{dx} = \gamma_x + \sum_{k=1}^{k=2} \alpha_k \beta_k e^{-\beta_k x} \tag{4.4}$$

Typical thickness in the middle of the axial coordinate is, eq. (2.58), $\delta_s \sim A(LE)^{1/3}$ and the Stewartson boundary layer reaches the same thickness as the Ekman layers near the corners at $z = 0$ and $z = 1$. In terms of the radial coordinate x the thickness is:

$$\delta_1 \sim AE^{1/2}$$

Applying this scale then the same process as discussed for the axial stretching can be applied to the radial stretching of the coordinate x for the parameter $k = 1$ and $k = 2$ in eq. (4.4):

- $k = 1$, $\beta_1 = \dfrac{2}{3\delta_1}$ with $\delta_1 = AE^{1/2}$
- $k = 2$, β_2 is determined from the relation $\beta_2 = \dfrac{1}{4\delta_s}$ with $\delta_s = A(LE)^{1/3}$.

The value for α_1 is fixed at 5%, α_2 is set by applying the ratio of the thickness of the Stewartson layer at $z = 0.5$ and the fictitious centreline:

- $\alpha_2 = 10\dfrac{\delta_s}{x_{cl}}$.

The parameters γ_x and γ_z are selected to map the domain from the coordinates $x = 0$, $x = x_{cl}$ and $z = 0$, $z = 1$ into a domain $\xi = 0$, $\xi = 1$ and $\eta = 0$, $\eta = 1$.

The settings of the various parameters as discussed in this section should be considered to be a good indication. Critical evaluations of actual results remain necessary to prevent wrong interpretation of model results.

4.3 Staggered Mesh

Discretisation of the equations will be discussed in the next section. Before doing so, the mesh, which will be used in the model, will be discussed easing the explanation and understanding.

Discretisation of the four nonlinearly coupled elliptic equations will result in a set of four coupled algebraic equations. The numerical solution of this set of equations can include an unwanted oscillating solution. Although mathematically correct, these oscillating solutions only exist due to the discrete representation of the differential equations. These oscillations hide the actual desired solution of the physical problem. A solution to prevent the dominating occurrence of these unwanted solutions is to develop the discrete equation not on the same mesh but on a set of meshes, shifted relative to each other. When rightly chosen, a much more stable system of equations results and provides the desired solution. Mathematically it results in a series of linear algebraic equations with a higher condition number for the resulting matrix. This can be understood intuitively after reviewing the values in the diagonals of the matrix close or

at the main diagonal: choosing the mesh properly, a concentration of high values close to the main diagonal results. This is not the case if the discrete equations would have been developed on a single mesh.

A second advantage of the staggered mesh technique is that discretisation of the first derivative results in 2nd order accuracy, as will be shown in the next section.

The equations contain only first derivatives in the axial coordinate; therefore, only a staggering in axial direction is required. The mesh in Fig. 4.1 fulfils these criteria.

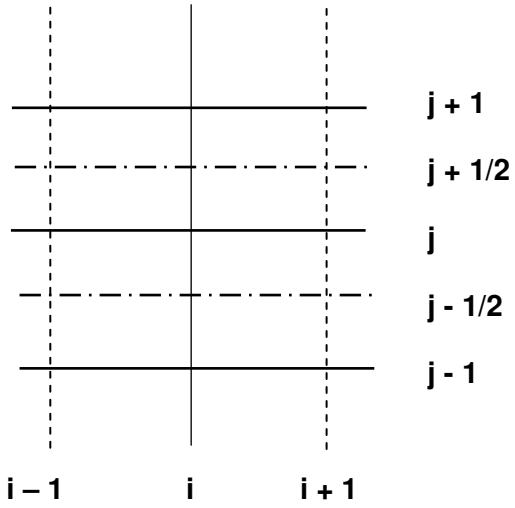

Figure 4.1: Staggered mesh. Discretisation of ψ and ζ is at i,j, ω at i,j+1/2 and θ at i,j-1/2.

The following has been selected to be the optimal mesh for the four equations:

- discretisation of ψ and ζ at the same mesh, i, j
- ω at a mesh lifted half a grid size in axial distance at i, ,j + 1/2
- θ at a mesh lowered half a grid size at i, j - 1/2.

The reasoning behind this choice is based on the effect that the first derivatives in the left side of the four elliptic equations have on the resulting matrix. In the following section it will be shown that selecting the mesh as introduced in Fig. 4.1 results in the same sign (negative) for the discrete formulation of all first derivatives at the diagonals close to the main diagonal. This contributes positively to the condition number of the resulting matrix.

Furthermore the four equations per grid point are placed in the resulting matrix in the order of $\omega, \zeta, \psi, \theta$. This concentrates high values on the sub diagonals as close as possible to the main diagonal.

In the model, the position of the mesh for ψ and ζ defines the full domain in axial and radial direction and the i,j grid points are positioned at the end caps, cylinder wall and fictitious centreline. As a result of the selected mesh, the equations for angular velocity and temperature are not directly positioned at the end caps but half a grid distance shifted in axial direction. To ensure that optimal accuracy is maintained, the discrete equations for these two variables are modified for the bottom and top layer to include a discretisation of half an axial grid size. This ensures that the boundary condition is modelled at exactly the end cap location.

4.4 Discretisation of model equations

In the model four coupled elliptic equations are solved simultaneously. This means that every grid point is represented by four linear discrete equations in the matrix. A traditional discretisation technique is used. In this section the discretisation of the equation for ζ and its boundary conditions is presented in detail. In Appendix C, the discrete form of the stream function, temperature and angular velocity equation has been given.

The equation for ζ reads, eq. (4.2):

$$\frac{1}{L}\frac{d\xi}{dz}\frac{\partial}{\partial\xi}(2\omega-\theta)e^{-x} = E\left[4A^2\frac{d\eta}{dx}\frac{\partial}{\partial\eta}\left(\frac{d\eta}{dx}\frac{\partial(1-x/A)\zeta}{\partial\eta}\right)+\frac{1}{L^2}\frac{d\xi}{dz}\frac{\partial}{\partial\xi}\left(\frac{d\xi}{dz}\frac{\partial\zeta}{\partial\xi}\right)\right] \tag{4.5}$$

The discretisation is central at i,j. The left hand side reflects this as well:

$$\left.\frac{1}{L}\frac{d\xi}{dz}\right|_j\left.\frac{\partial(2\omega-\theta)e^{-x}}{\partial\xi}\right|_{i,j} \sim \left.\frac{1}{L}\frac{d\xi}{dz}\right|_j\left[\frac{(2\omega|_{i,j}-\theta|_{i,j+1})}{\delta\xi}-\frac{(2\omega|_{i,j-1}-\theta|_{i,j})}{\delta\xi}\right]e^{-x}\Big|_i+O(\delta\xi^2) \tag{4.6}$$

$\delta\xi$ is defined as: $\delta\xi=\frac{x_{cl}}{(M-1)}$, where x_{cl} is the fictitious centreline and M the total number of radial grid points. Furthermore $\delta\eta=\frac{1}{(N-1)}$ will be used as the discrete distance between axial grid locations with *N* the total number of axial grid points.

In eq. (4.6) the effect of the shifted, staggered mesh is recognised: both ω and θ at i,j are present in the matrix with same sign (+).

The first term of the right hand side of eq. (4.5) follows by the same reasoning:

$$\left.\frac{d\eta}{dx}\right|_i \left\{\frac{\partial}{\partial\eta}\left[\frac{d\eta}{dx}\left(\frac{\partial(1-x/A)\zeta}{\partial\eta}\right)\right]\right\}\Bigg|_{i,j} \sim \left.\frac{d\eta}{dx}\right|_{i,j} \left\{\left.\frac{d\eta}{dx}\right|_{i+1/2,j}\left[\frac{(1-x_{i+1}/A)\zeta_{i+1.j}}{(\delta\eta)^2}-\frac{(1-x_i/A)\zeta_{i.j}}{(\delta\eta)^2}\right]\right\}$$

$$-\left.\frac{d\eta}{dx}\right|_{i,j} \left\{\left.\frac{d\eta}{dx}\right|_{i-1/2,j}\left[\frac{(1-x_i/A)\zeta_{i.j}}{(\delta\eta)^2}-\frac{(1-x_{i-1}/A)\zeta_{i-1.j}}{(\delta\eta)^2}\right]\right\} + O(\delta\eta^2) \qquad (4.7)$$

The second term at the right hand side results in:

$$\left.\frac{1}{L^2}\frac{d\xi}{dz}\right|_j \left\{\frac{\partial}{\partial\xi}\left[\frac{d\xi}{dz}\left(\frac{\partial(\zeta)}{\partial\xi}\right)\right]\right\}\Bigg|_{i,j} \sim \left.\frac{1}{L^2}\frac{d\xi}{dz}\right|_j \left\{\left.\frac{d\xi}{dz}\right|_{j+1/2}\left[\frac{\zeta_{i,j+1}}{(\delta\xi)^2}-\frac{\zeta_{i.j}}{(\delta\xi)^2}\right]\right\} -$$

$$\left.\frac{1}{L^2}\frac{d\xi}{dz}\right|_j \left\{\left.\frac{d\xi}{dz}\right|_{j-1/2}\left[\frac{\zeta_{i,j}}{(\delta\xi)^2}-\frac{\zeta_{i.j-1}}{(\delta\xi)^2}\right]\right\} + O(\delta\xi^2) \qquad (4.8)$$

Combining eqs. (4.6) - (4.8) results in the following equation for the discrete version of the ζ equation:

$$\left.\frac{d\xi}{dz}\right|_j \left.\frac{2}{\delta\xi}e^{-x}\right|_i \omega_{i,j-1} = a_1\omega_{i,j-1}$$

$$\frac{E}{L}\left.\frac{d\xi}{dz}\right|_j \left\{\left.\frac{d\xi}{dz}\right|_{j-1/2}\left[\frac{1}{(\delta\xi)^2}\right]\right\} \zeta_{i,j-1} = a_3\zeta_{i,j-1}$$

$$4A^2LE\left.\frac{d\eta}{dx}\right|_{i,j} \left\{\left.\frac{d\eta}{dx}\right|_{i-1/2,j}\left[\frac{(1-x_{i-1}/A)}{(\delta\eta)^2}\right]\right\} \zeta_{i-1,j} = a_7\zeta_{i-1,j}$$

$$-\left.\frac{d\xi}{dz}\right|_j \left.\frac{2}{\delta\xi}e^{-x}\right|_i \omega_{i,j} = a_9\omega_{i,j}$$

$$-LE\left\{\left.\frac{1}{L^2}\frac{d\xi}{dz}\right|_j \left[\left.\frac{d\xi}{dz}\right|_{j+1/2}\left(\frac{1}{(\delta\xi)^2}\right)\right] + 4A^2\left.\frac{d\eta}{dx}\right|_i \left[\left.\frac{d\eta}{dx}\right|_{i+1/2}\left(\frac{1-x_i/A}{(\delta\eta)^2}\right)\right]\right.$$

$$+4A^2\left.\frac{d\eta}{dx}\right|_i\left[\left.\frac{d\eta}{dx}\right|_{i-1/2}\left(\frac{1-x_i/A}{(\delta\eta)^2}\right)\right]+\left[\frac{1}{L^2}\left.\frac{d\xi}{dz}\right|_{j-1/2}\left(\frac{1}{(\delta\xi)^2}\right)\right]\left.\frac{d\xi}{dz}\right|_j\Bigg\}\ \zeta_{i,j}=a_{11}\zeta_{i,j}$$

$$-\left.\frac{d\xi}{dz}\right|_j\left.\frac{1}{\delta\xi}e^{-x}\right|_i\ \theta_{i,j}=a_{12}\theta_{i,j}$$

$$4A^2LE\left.\frac{d\eta}{dx}\right|_{i,j}\left\{\left.\frac{d\eta}{dx}\right|_{i+1/2,j}\left[\frac{(1-x_{i+1}/A)}{(\delta\eta)^2}\right]\right\}\ \zeta_{i+1,j}=a_{15}\zeta_{i+1,j}$$

$$\frac{E}{L}\left.\frac{d\xi}{dz}\right|_j\left\{\left.\frac{d\xi}{dz}\right|_{j+1/2}\left[\frac{1}{(\delta\xi)^2}\right]\right\}\ \zeta_{i,j+1}=a_{19}\zeta_{i,j+1}$$

$$\left.\frac{d\xi}{dz}\right|_j\left.\frac{1}{\delta\xi}e^{-x}\right|_i\ \theta_{i,j+1}=a_{20}\theta_{i,j+1}$$

this results in a single row in the matrix:

$$a_1\omega_{i,j-1}+a_3\zeta_{i,j-1}+a_7\zeta_{i-1,j}+a_9\omega_{i,j}+a_{11}\zeta_{i,j}+a_{12}\theta_{i,j}+a_{15}\zeta_{i+1,j}+a_{19}\zeta_{i,j+1}+a_{20}\theta_{i,j+1}=0 \tag{4.9}$$

In principle 20 elements can be addressed in each line: four variables multiplied by five grid points.

The same discretisation philosophy has been followed for the other three equations, resulting in four rows per grid point.

Eq. (4.9) is the general discretisation for a grid point not adjacent to a boundary of the domain, for each of the boundary conditions specific discretisations have to be developed.

Discretisation of the boundary condition at the wall results from eq. (3.10):

$$\zeta=4A^2\frac{\partial}{\partial x}\left(e^x\frac{\partial\psi}{\partial x}\right)\ \text{and}\ \frac{\partial\psi}{\partial x}=0\ ;\ 0>z<1;\ x=0 \tag{4.10}$$

or

$$\zeta_{1,j}=4A^2\left.\frac{d\eta}{dx}\right|_{i=1}\left\{\frac{\partial}{\partial\eta}e^x\left[\frac{d\eta}{dx}\left(\frac{\partial\psi}{\partial\eta}\right)\right]\right\}\Bigg|_{i=1}\ \sim$$

$$4A^2 \left.\frac{d\eta}{dx}\right|_{i=1} \left\{ e^{x_{i+1/2}} \left.\frac{d\eta}{dx}\right|_{i+1/2} \left[\frac{\psi_{i+1.j}}{(\delta\eta)^2} - \frac{\psi_{i.j}}{(\delta\eta)^2} \right] \right\} -$$

$$4A^2 \left.\frac{d\eta}{dx}\right|_{i=1} e^{x_{-1/2}} \left\{ \left.\frac{d\eta}{dx}\right|_{i-1/2} \left[\frac{\psi_{i.j}}{(\delta\eta)^2} - \frac{\psi_{i-1.j}}{(\delta\eta)^2} \right] \right\} + O(\delta\eta^2) \qquad (4.11)$$

Applying the boundary condition: $\frac{\partial \psi}{\partial x} = 0$, e.g. (4.6) results in the discrete equation:

$$\left\{ \left.\frac{d\eta}{dx}\right|_{i+1/2} \left[\frac{\psi_{2.j}}{\delta\eta} - \frac{\psi_{1.j}}{\delta\eta} \right] \right\} + \left\{ \left.\frac{d\eta}{dx}\right|_{i-1/2} \left[\frac{\psi_{1.j}}{(\delta\eta)^2} - \frac{\psi_{-1.j}}{(\delta\eta)^2} \right] \right\} = 0 \qquad (4.12)$$

Substituting the second term of eq. (4.8) into the last term of eq. (4.7) eliminates the fictitious grid point at i = -1, resulting in:

$$\zeta_{i,j} = 8A^2 \left.\frac{d\eta}{dx}\right|_{i=1} \left\{ \left.\frac{d\eta}{dx}\right|_{i+1/2} \left[\frac{\psi_{i+1.j}}{(\delta\eta)^2} - \frac{\psi_{i.j}}{(\delta\eta)^2} \right] \right\} + O(\delta\eta^2) \qquad (4.13)$$

Obviously this relation should be expressed in the equivalent of eq. (4.9) and subsequently included in the set of linear equations.

The same discretisation can be applied for the boundary condition at the end caps, eq. (3.11):

$$\zeta(1 - x/A)\, e^{-x} = \frac{1}{L^2} \frac{\partial^2 \psi}{\partial z^2} \text{ and } \frac{\partial \psi}{\partial z} = 0 \text{ ; } 0 > x < A; z = 0, z=1 \qquad (4.14)$$

Eq. (4.15) illustrates the resulting relation for the boundary condition at the bottom, j = 1:

$$\zeta_{i,1} = \frac{2e^{x_i}}{(1 - x_i/A)L^2} \left.\frac{d\xi}{dz}\right|_{j=1} \left\{ \left.\frac{d\xi}{dz}\right|_{j=+1/2} \left[\frac{\psi_{i.2}}{(\delta\xi)^2} - \frac{\psi_{i.1}}{(\delta\xi)^2} \right] \right\} + O(\delta\xi^2) \qquad (4.15)$$

Eqs. (4.13) and (4.15) reveal the reason why the multi-grid method applied by Schroeder and Hanel [23] suffered from instabilities, resulting in slow convergence as reported by the authors. Both equations show a relation between ζ at the wall and ψ inwards of the wall or end cap. This problem is circumvented in the developed numerical approach as will be discussed in the next section.

The boundary condition at the fictitious centreline is a trivial one:

$$\zeta_{M,j} = 0 \qquad (4.16)$$

4.5 Solving the matrix

Parameters used to define the grid are shown in Fig. 4.2. Each grid point results in four rows in the resulting matrix. A mesh with M radial grid points and N in axial direction, results in $\approx$ M*N*4 rows and in a bandwidth $\approx$ (2*M+1)*4.

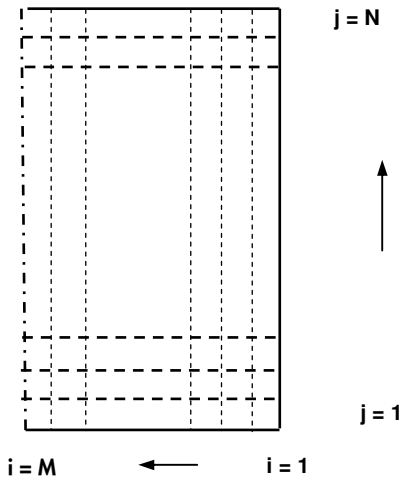

Figure 4.2: Numerical mesh parameters.

Although a direct method can be used to solve the resulting linear system of equations from the discretisation exactly, an iterative solution method has the clear advantage to reduce the required computer memory. The method developed for this specific application is based on the following two considerations:

- the four elliptic equations are strongly coupled close to the cylinder wall and hardly coupled towards the fictitious centreline as demonstrated in Section 2.2. It is of great advantage to solve the discrete equations directly, fully coupled, in this area since iterative schemes show in general slow convergence for strongly coupled equations
- the boundary values for the vorticity eq. (4.13) form a strong coupling of a different kind between the discrete versions of the ψ and ζ equations at the rotating wall. The same holds for the bottom and top end cap relations where ψ and ζ are again strongly coupled due to the axial boundary conditions for the vorticity. The couplings result in slow convergence as well, e.g. the article from Schroeder and Hanel [23] applying Multi-grid and iterative schemes. A direct method solving the coupled equation close to the wall and at the end caps would resolve this instability.

Both considerations suggest to solve the equations in a single strip close to the cylinder wall by a direct method, subsequently the whole domain is resolved strip by strip as is illustrated in Fig. 4.3.

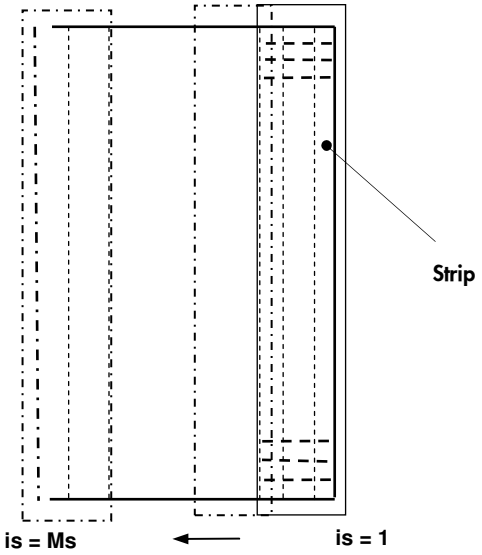

Figure 4.3: Schematic overview of the iterative scheme.

So the same direct technique used to resolve the layer close to the wall is repeated in adjacent strips till the centreline. Overlay between the subsequent strips provide the required boundary values for the next strip.

Fig. 4.3 shows that Ms strips cover the whole of the domain in radial direction. The number of grid points per strip is S, by definition, and the overlay form one strip to the other is io. The total number of radial grid points that is resolved per sweep is:

$$Mtot = (Ms-io-1)*S+1+io.$$

In most cases an overlay of only 1 or 2 grid points proves to be sufficient. The resulting matrix has a length $\approx$ N*S*4 and a bandwidth $\approx$ 2*(S+1)*4.

As can be understood, for is = 1, all the wall and end cap boundary conditions are fully implicitly included. The same holds for the end cap boundary conditions, if is >1. For is = Ms, all fictitious centreline boundary conditions are fully included as well as the end cap relations. As a result of this, fast convergence is reached without instabilities as reported by Schroeder and Hanel [23].

A number of sweeps from the wall to the centreline is repeated till convergence is reached.

4.5.1 Numerical Convergence

The speed of convergence is highly dependent on the centrifuge parameters, boundary conditions, selection of the number of strips and overlay of the strip as discussed in the previous section. To illustrate this, numerical convergence tests are presented for two different cases: a Long and a Semi-long centrifuge.

The iteration error is calculated for the four variables individually as the vector length of the change of the individual variable between two full sweeps: these are the individual variable error vectors. Subsequently the total error as reported in Fig. 4.4 and 4.6 is calculated as the vector length of the four individual variable error vectors.

The following parameter sets have been used during these simulations.

Parameters	Long centrifuge	Semi-long centrifuge
A	67	16
E	$4.2\ 10^{-8}$	$3.4\ 10^{-7}$
L	53	27
Nr. of strips	4	2
Grid points/strip	15	25
Overlay	2	1
Grid point Axial	99	99

Table 4.1: A parameter set for a Long and Semi-long centrifuge. These parameter sets are used to demonstrate the convergence of the numerical model with respect to the mesh size in radial and axial direction.

In Fig. 4.4 the total error is presented as function of the number of sweeps for the Long centrifuge and Fig. 4.5 presents the convergence of the flow efficiency. In Fig. 4.6 and Fig. 4.7 the same information is given for the Semi-long centrifuge.

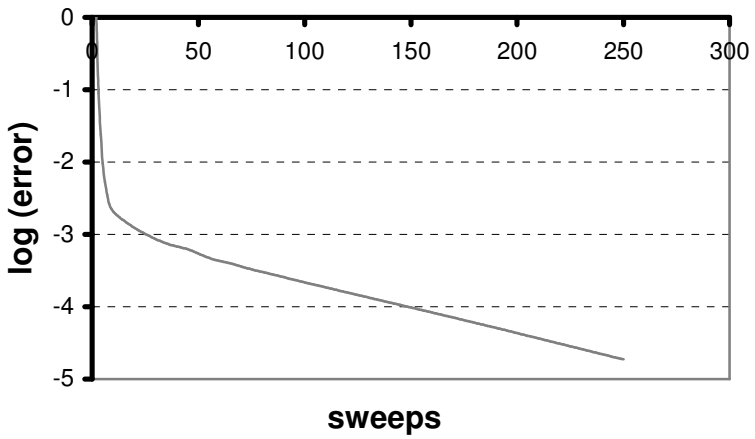

Figure 4.4: Iteration error for a Long centrifuge, see Table 4.1, versus the number of iterations.

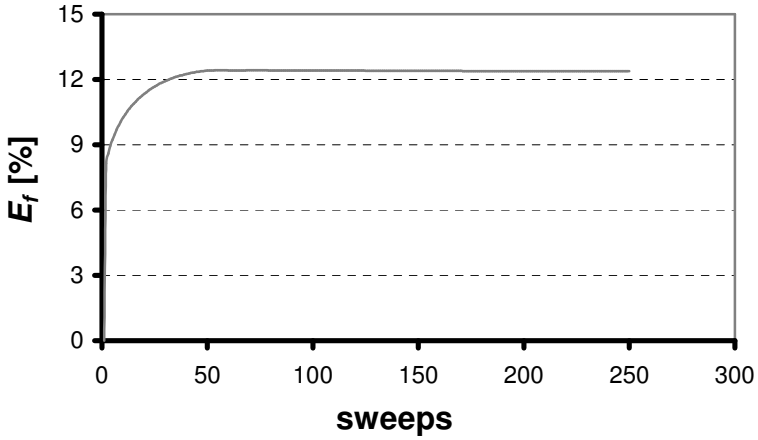

Figure 4.5: Convergence of the flow efficiency for a Long centrifuge, see Table 4.1, versus the number of iterations.

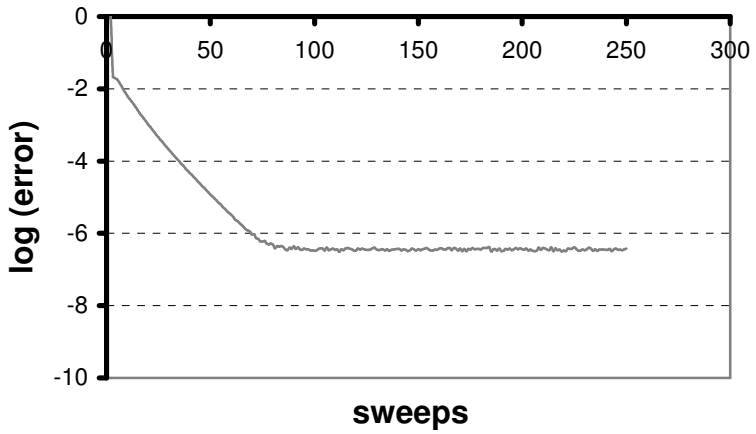

Figure 4.6: Iteration error for a Semi-long centrifuge, see Table 4.1, versus the number of iterations.

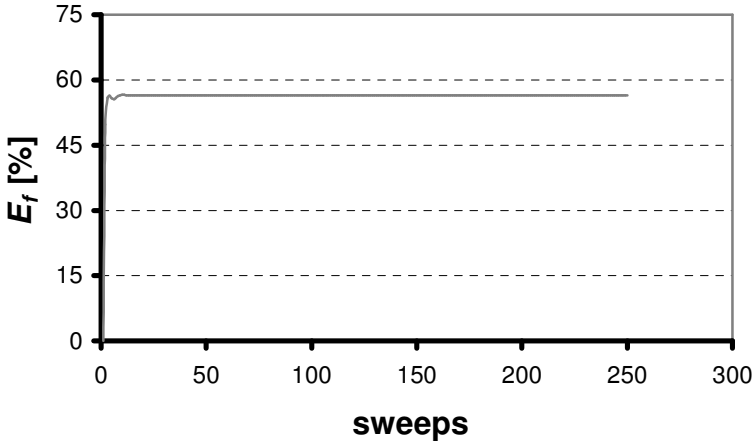

Figure 4.7: Convergence of the flow efficiency for a Semi-long centrifuge, see Table 4.1, versus the number of iterations.

These results illustrate that the flow efficiency calculation for the Long centrifuge converged after approximately 50 iterations, for the Semi-long centrifuge after $\approx$ 15.

A single simulation at a mesh of 50 radial and 100 axial grid points takes some 15 seconds on a personal computer, anno 2009.

4.6 Model and software testing

In this section results will be reported to verify the accuracy of the model by comparing actual calculations with analytical results. The parameter set defining a Semi-long centrifuge is given in table 4.2:

E	*L*	*A*	x_c
$6\ 10^{-8}$	28	21	4

Table 4.2: Parameter set for a Semi-long centrifuge to be used to demonstrate the effect of different fictitious centre lines on the calculated flow efficiency.

In this parameter set x_c is the location along the *x* - axis where the coupling between the equations relaxes as defined in eq. (2.56). It is the position where the viscous area ends and the diffusive core starts.

Some more characteristics of this centrifuge are:

- the inner Stewartson layer thickness at $z = 0.5$, eq. (2.58) is, x_s = O(0.25)
- the Ekman layer thickness at $x = 0$ is, δ = O(10^{-5})

A dimensionless temperature difference of two ($\Delta\theta = 2$) between top and bottom end cap together with a linear temperature gradient along the wall is applied to drive the internal flow. Heat conduction through end caps and cylinder wall is set to zero. By applying this driving mechanism for the internal flow, only a gas flow in a thin layer near the rotating wall will develop. The gas in the remaining cross sectional area of the cylinder will be virtually stagnant. Obviously a low flow efficiency factor will result. This driving mechanism is chosen since it forms a challenge for the numerical approach. Only a limited number of grid points will be located in this thin area near the wall where the gas flow develops. The majority of the grid points are located in the cross sectional area with the almost stagnant flow.

Ten calculations are reported in Table 4.3. The total mesh points ranges from $\approx$ 1500 to $\approx$ 15000 by varying the mesh size in both axial and radial direction. The domain is varied by assuming three different fictitious centrelines x_{cl} = 6, 9 and 12.

Grid points Axial	Grid points Radial	E_f x_{cl} = 6	E_f x_{cl} = 9	E_f x_{cl} = 12
[-]	[-]	[%]	[%]	[%]
49	29	-	-	8.5
49	47	7.2	-	7.8
49	65	7.2	7.5	7.6
49	83	-	-	7.5
49	101	-	-	7.4
49	119	7.2	7.5	7.4
49	137	-	-	7.4
49	157	-	-	7.4
99	101	-	7.4	7.5
159	101	7.2	-	7.5
89	83	-	7.5	7.5

Table 4.3: Grid points and calculated E_f for three different fictitious centre lines. The applied driving mechanism for the internal flow is a temperature difference of two ($\Delta\theta = 2$) between the end caps together with a linear temperature gradient ($\nabla\theta = 2$) along the wall.

Standard settings as discussed in Section 4.2 are used to stretch the axial and radial coordinate. From this challenging test it is concluded that the convergence relative to the number of grid points is evident. Applying approximately 50 grid points in radial direction results in an estimated absolute error in the calculated E_f of approximately 0.3%, which is an error of $\approx$ 4% relative. For the fictitious centreline it is concluded that $x_{cl} = 12$ is an appropriate value. The local density is $\approx 10^{-5}$ of the wall pressure at this radial position.

A comparable test, applying the ideal Ekman suction boundary values, eq. (2.62), results in calculated flow efficiencies and presented in Table 4.4.

Grid points Axial	Grid points Radial	E_f x_{cl} = 6	E_f x_{cl} = 9	E_f x_{cl} = 12
[-]	[-]	[%]	[%]	[%]
49	83	21.5	27.5	30.2
99	83	21.4	27.4	30
149	83	21.4	27.4	30
149	65	21.4	-	-
49	65	21.4	-	-
49	65	-	-	30.5
49	65	-	27.4	-
149	119	-	27.3	-

Table 4.4: Grid points and calculated E_f for three different positions of the fictitious centre lines. The applied driving mechanism for the internal flow is IBC.

Moving the fictitious centreline from x = 6 to x = 9 to x = 12 allows for more Ekman suction at the end caps towards the centre of the centrifuge when IBC is applied. Applying these boundary conditions results in approximately 4 times higher values of E_f compared to the previously reported simulations in Table 4.3. Since IBC compensates for the reducing density towards the centreline they result in high local temperatures or low local angular velocities at these high x values. In practice, the local temperature and local angular velocities are limited. Therefore x_{cl} = 12 is considered to be a practical limit for the numerical domain.

Convergence of the simulations, with respect to the grid size, for the three specific centrelines is evident. The results as presented in Table 4.4 indicate that 50 grid points in axial direction and in radial directions is sufficient. In the remainder of this thesis 100 grid points in axial direction will be applied. This higher number of axial grid points might not be required from a calculated flow efficiency accuracy point of view but this increasing resolution allows for more detailed study of the flow in the Ekman layer.

Most personal computers anno 2009 have memory capabilities such that this grid size can be executed directly; hence avoiding the iterative procedure to resolve the matrix equation.

4.7 Analytical versus numerical results

In this section numerical results will be compared with analytical results for the centrifuge as defined in the previous section. The driving mechanism for the internal flow is a dimensionless temperature difference of two ($\Delta\theta = 2$) between the end caps only.

In Fig. 4.8 and Fig. 4.9 the stream function at z = 0.5 is given versus the grid points and versus the x - coordinate.

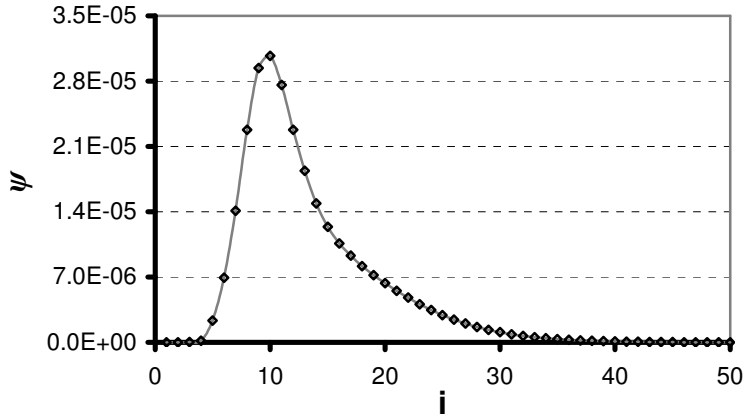

Figure 4.8: Radial distribution of the stream function ψ at z = 0.5 for a Semi-long centrifuge, see Table 4.2. The driving mechanism is a temperature difference $\Delta\theta = 2$ between the end caps. ψ is presented against the grid point i.

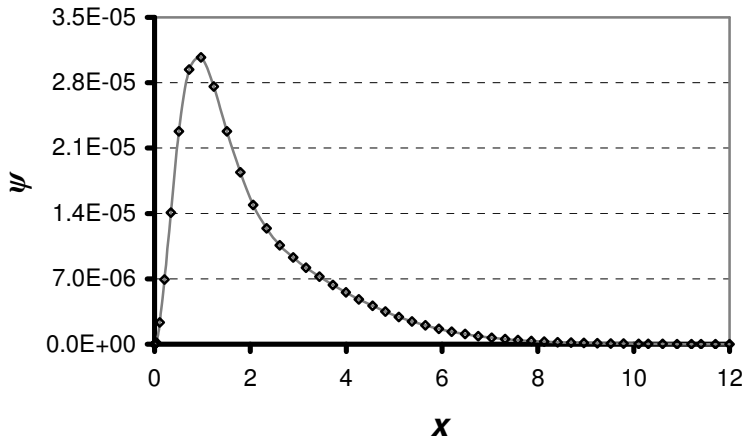

Figure 4.9: : Radial distribution of the stream function ψ at z = 0.5 for a Semi-long centrifuge. The driving mechanism is a temperature difference $\Delta\theta = 2$ between the end caps. ψ is presented against x.

The value of the stream function as predicted by the analytical results is calculated as follows:

$$\psi = 1/4(1-x/A)/(1+1/4Br(1-x/A))^{3/4}(Ee^{-x})^{1/2} \qquad (4.17)$$

resulting in $\approx$ 2.7 10^{-5} at x = 1, close ($\approx$ 10%) to the value calculated by the numerical model.

The Stewartson layer thickness has a thickness $\approx$ 1, approximately four times $O(x_s)$ with $x_s = A(LE)^{1/3}$, eq. (2.58). This is some 25% above analytical estimates from Brouwers [42], this is contributed to the inclusiveness of the reducing density in the layer, Dickinson and Jones [17]. Analytical models assume constant density in the layer.

In Fig. 4.10 and Fig. 4.11 the stream function along the axial grid point j and coordinate z is given at the radial position of the peak in Fig. 4.9, $x \approx 1$.

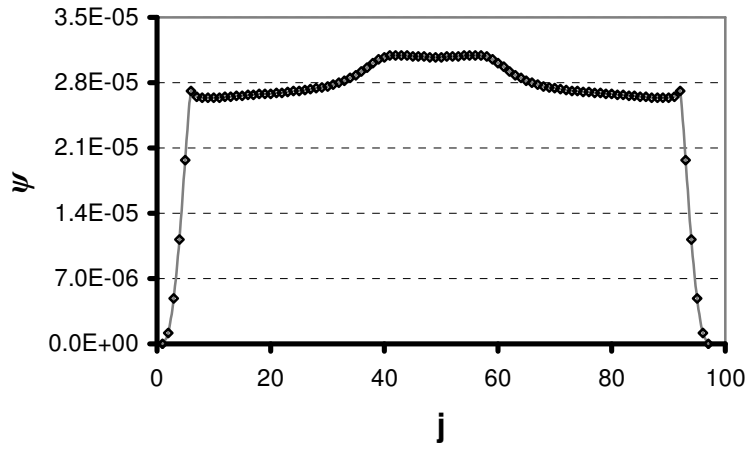

Figure 4.10: Axial distribution of the stream function ψ for a Semi-long centrifuge. ψ is presented against the grid point j at $x \approx 1$. The driving mechanism is a temperature difference $\Delta\theta = 2$ between the end caps.

In Fig 4.11, the same data is presented against the axial coordinate *z*.

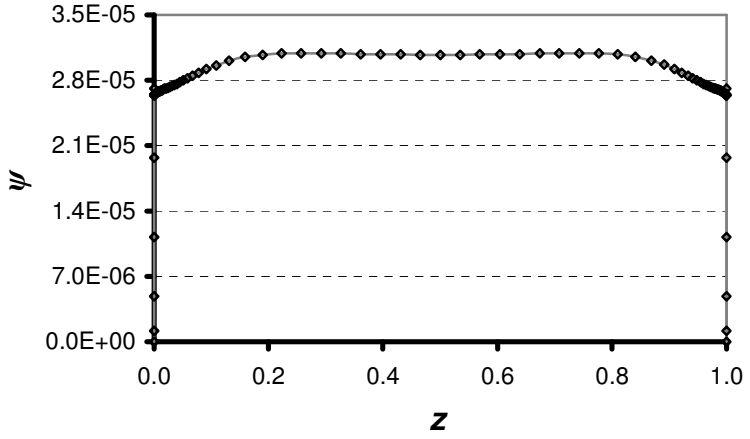

Figure 4.11: Axial distribution of the stream function ψ for a Semi-long centrifuge. ψ is presented against the axial axis z at $x \approx 1$. The driving mechanism is a temperature difference $\Delta\theta = 2$ between the end caps.

The results in Fig. 4.8 through Fig. 4.11 are given against the numerical grid position i,j and *x*, *z* to illustrate the effect of stretching the radial and axial coordinates. More details of the stretching of the coordinates are given in Appendix D.
As can be seen in Fig. 4.11, the Ekman layers are so thin that they are hardly visible when results are presented against the actual *z*-axis.

The Ekman layer is illustrated by presenting the stream function close to the bottom end cap in Figure 4.12 and 4.13.

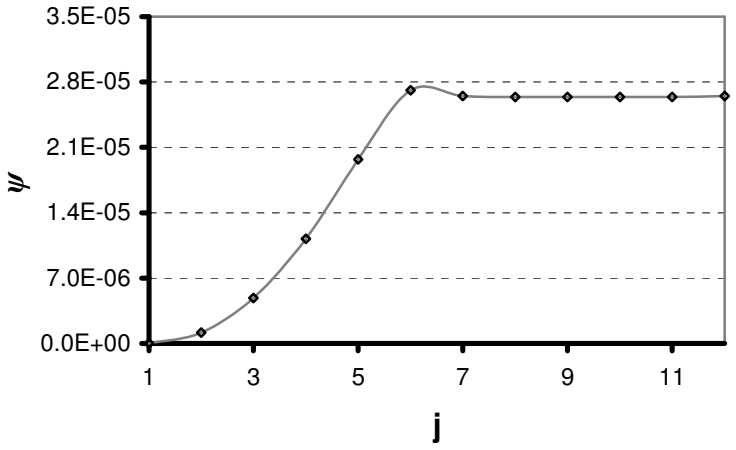

Figure 4.12: Axial distribution of the stream function ψ . ψ is represented against the grid point j, *near the lower end cap at $x \approx 1$, illustrating the Ekman boundary layer.*

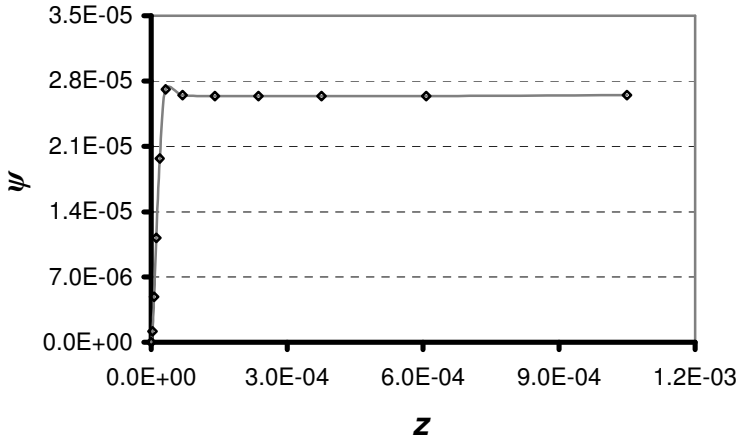

Figure 4.13: Axial distribution of the stream function ψ . ψ is represented against the axial axis z, *near the lower end cap at $x \approx 1$, illustrating the Ekman boundary layer.*

The Ekman layer thickness follows from:

$$\delta(x) \sim L^{-1}(Ee^{x})^{1/2}$$

Applying the actual data for E and *L* ($E = 6\,10^{-8}$ and $L = 28$) results in $\delta \sim 1.5\,10^{-5}$ at *x = 1* which is close to the observed thickness in Figure 4.13.

The following two figures are included to prove that the boundary values at the wall and end caps for ψ are fulfilled. In Fig. 4.14, $\frac{\partial \psi}{\partial x}$, representing the axial velocity at the rotating wall is clearly approaching zero. In Fig. 4.15 the same is presented for $\frac{\partial \psi}{\partial z}$, the radial velocity at an end cap.

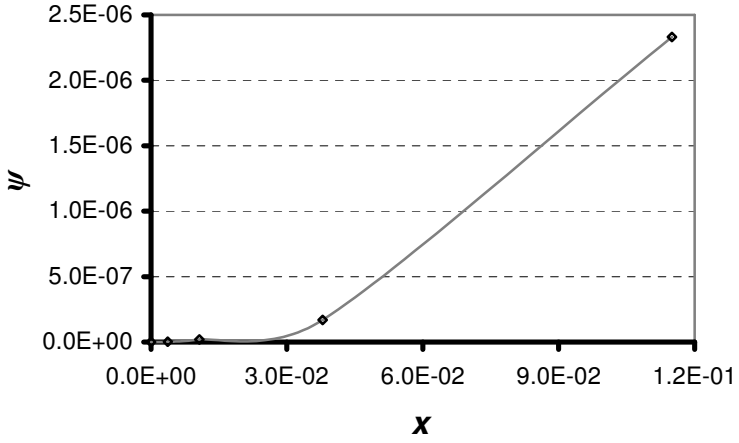

Figure 4.14: Radial distribution of the stream function ψ near the rotating wall, illustrating the correct boundary value: $\frac{\partial \psi}{\partial x} = 0$ at $x = 0$.

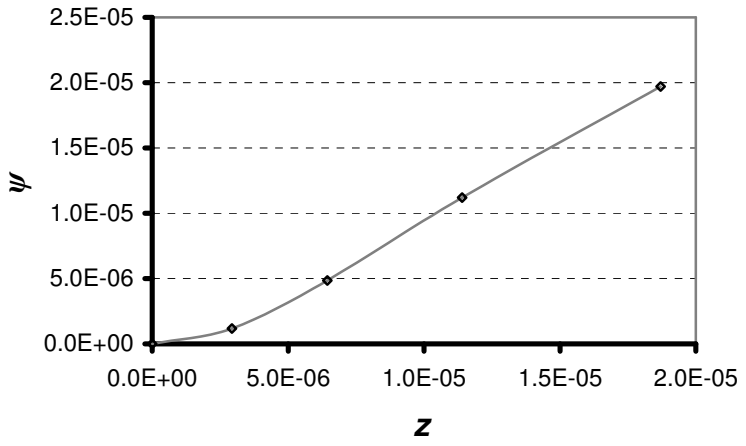

Figure 4.15: Axial distribution of the stream function ψ near the lower end cap, illustrating the correct boundary value: $\frac{\partial \psi}{\partial z} = 0$ at $z = 0$.

From the USEC webpage [40] it can be concluded that that a centrifuge can have a length of several meters, which means that the Ekman layer would have a thickness of $\delta \sim 10^{-2}$ mm when the parameters of Table 4.2 are applied. Furthermore from Fig. 4.9 it is concluded that ψ peaks at $x \approx 1$. By applying the definition for x, the radial position can be calculated as $r = \sqrt{(1-1/21)} \approx 0.98$. Assuming a centrifuge diameter of 0.2 m, Brouwers [3], then it follows that the peak in the stream function is about 2 mm from the rotating wall.

4.8 Comparing end cap and wall temperature drive

Analysis and previous numerical models predict large differences between stream function values obtained from end cap drive only and linear wall temperature gradient drive. To test the model and to illustrate this effect, two calculations applying different driving mechanisms for the internal flow are reported in this section:

- end cap drive only, applying a temperature difference ($\Delta\theta = 2$) between bottom and top end cap
- a linear temp gradient only, applying a temperature gradient of two along the wall ($\nabla\theta = 2$).

Centrifuge parameters as presented in Table 4.5 will be applied.

E	L	A	x_c
0.22 10^{-6}	28	40	1.0

Table 4.5: Parameter set of a Semi-long centrifuge to be used to compare numerical results versus analytical for both end cap and wall temperature gradient drive.

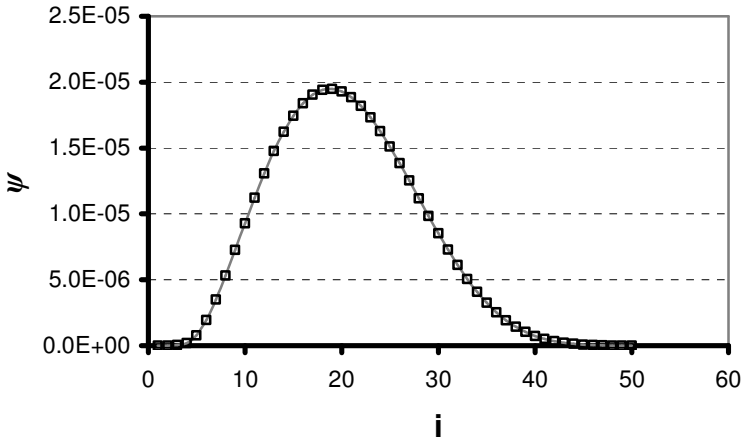

Figure 4.16: Radial distribution of the stream function ψ at z = 0.5 for a Semi-long centrifuge. The driving mechanism is a temperature difference $\Delta\theta = 2$ between the end caps.

Applying a temperature difference $\Delta\theta = 2$ between the end caps, results in a stream function as in Figure 4.16. The same analytical equation from Section 2.5.4, eq. (2.60) is applied to estimate the analytical result:

$$\psi = \frac{1}{4}(1 - x/A)/(1 + 1/4Br(1 - x/A))^{3/4}(Ee^{-x})^{1/2} \tag{4.18}$$

Substituting the centrifuge parameters in Table 4.5 and the fact that the peak is at $x \approx$ 1.7, a value of the stream function value of $\approx 2.510^{-5}$ can be calculated, which is somewhat higher compared to the numerical value. This can be explained by the fact that the peak value of the stream function as calculated by the numerical model is in the diffusive core which start at $x \approx 1$.

In the case of having no temperature boundary conditions applied at the end caps while applying a linear temperature gradient $\nabla\theta = 2$ at the centrifuge wall only, results in a stream function at $z = 0.5$ as given in Fig. 4.17.

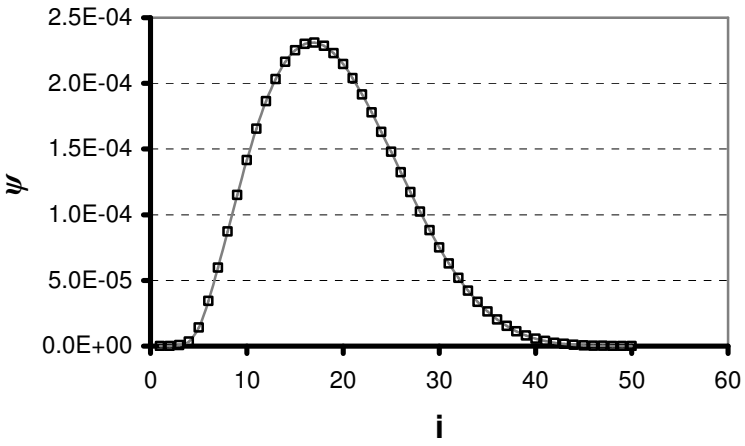

Figure 4.17: Radial distribution of the stream function ψ at z = 0.5 for a Semi-long centrifuge. The driving mechanism is a temperature gradient $\nabla\theta = 2$ along the rotating wall.

As mentioned in Chapter 2, the order of magnitude of the stream function in this case is O($A(LE)^{1/3}$), the full equation for this case reads, as indicated in Section 2.2.3:

$$\psi = 1/(4(1+1/4Br))*(LE)^{1/3}e^{-x} \tag{4.19}$$

Applying the parameters in Table 4.5 results in $\psi = O(510^{-4})$, at $x \approx 1.4$, approximately a 40% lower peak value.

Important to note is the order of magnitude difference in values of the stream function in Fig. 4.16 and 4.17.

4.9 Conclusions

Simulations show that a mesh 100*50 (100 in axial direction and 50 in radial direction) is sufficient and the fictitious centre line can be set at $x = 12$.

The Ekman layers as calculated by the model are in line with the thicknesses as predicted by the boundary layer theory. The calculated inner Stewartson layer has an actual thickness $\approx 4\,A(LE)^{1/3}$. This is in line with earlier publications. Applying full linear model calculations results in somewhat thicker layers compared to analytical theory e.g. Dickinson and Jones [17]. This is contributed to the reducing pressure in these calculations while analytical results are based on constant gas pressure in these layers.

The calculated absolute values of the stream function have been compared with analytical models and the results are comparable, both for end cap and wall drive applications.

Presented results show that the discretisation scheme fulfils the expected boundary conditions at the rotating wall and end cap.

The tests prove the validity of the numerical model and give confidence of accuracy and stability to use it for more complex boundary conditions where analytical models are less suitable or not suitable at all. In the following chapters several cases of more complex boundary values will be presented.

Chapter 5

Parameter study

Summary

In this chapter, numerical results applying the model and numerical method as introduced in previous chapters, will be presented and discussed. A main feature of the model is the flexible boundary condition settings, e.g. the boundary conditions for the dimensionless temperature θ at the top and bottom end cap as well as along the cylinder wall can be specified independent. Furthermore, the dimensionless angular velocity ω can be specified at the bottom end cap. This proves to be of great value in gaining new insights in centrifuge performance. The results will be compared with results from the analytical model as discussed in Chapter 2, based on Brouwers [42].

The analytical model is based on the assumption that the efficiency is mainly limited by the position of the diffusive core at $x = x_c$, as introduced in Chapter 2, eq. (2.56). Axial gas flow at $x > x_c$ is limited by the decreasing density, resulting in a reduced axial flow function along the radial coordinate towards the centreline. Application of Ideal Ekman conditions as given in, eq. (2.62) results in pumping gas by the Ekman boundary layer along the end caps into the main compartment (or reversibly sucking it out of the main compartment) at radial positions $x > x_c$. Hence there is an incompatibility: gas is pumped in or sucked out at radial positions where axial flow cannot be maintained. It is assumed in the analytical model that the gas is pumped by the Ekman layer in the main compartment and subsequently flows towards the rotating wall down to a radial position: $x = x_c$. From here the gas flows in axial direction only. As a result of this, the local efficiency, as follows from eq. (1.6), will be higher close to the end caps compared to its value in the middle section of the cylinder. Brouwers [42] suggests that E_f can be calculated from an averaged value of the position of the diffusive core according to:

$$x = x_c + 0.5$$

In Section 5.1 pulse tests are performed for centrifuges in the Semi-long and Short domain. They explicitly show the existence and the importance of the diffusive core. Furthermore a simulation for a centrifuge in the Short domain is presented and fluid dynamic details further analysed. The numerical results add an extra element to the behaviour of the flow in the inviscid region compared to analytical work: contrary to expectations, the boundary conditions at the end caps in the viscous and diffusive region influence the flow in the inviscid region.

A presentation of calculated flow efficiencies will be derived in Section 5.2 and applied in the remainder of this chapter. This presentation allows data gathered during a parameter study, for a specific set of boundary conditions, to be mapped in a single graph. This presentation of results visualizes the loss in performance due to in-ideal

boundary conditions and is a considerable improvement in comparison to earlier publications where a variety of graphs is used to present the same type of results.

In the next five sections the results of parameter studies on the flow efficiency is reported by varying the velocity parameter (*A)*, Ekman number (*E*) and dimensionless length (*L).* The selection of parameters results in centrifuges ranging from “Long” to “Short”. Furthermore the boundary conditions will be varied from “Ideal” to “Technically feasible”. The background of this is that the Ideal Ekman conditions result in a strongly increasing temperature towards the centreline and/or a strongly decreasing angular velocity. This might not be achievable in a real situation: too high temperatures at the end cap might result in unwanted mechanical issues. The temperature should be limited to acceptable values. This is simulated in Sections 5.6 and 5.7. Two models will be applied at the bottom end cap limiting the temperature increase towards the centreline. The resulting effect on the flow efficiency is presented accordingly.

Overall conclusions on the parameter study are summarised in Section 5.8

The thermal properties of the end caps and wall of the cylinder are set to such values that conduction of heat does not play a role in these elements. Additionally, the heat transfer coefficient is set at a significantly high value so that the temperatures of the centrifuge wall and end caps are equal to the temperature of the containing environment.

5.1 The existence of a diffusive core

The vertical boundary layer approach for gas centrifuges stems from geophysical theories and forms the basis for analytical models as discussed in Chapter 2. These vertical boundary layers are expected to develop and separate one flow region from the other. In the various regions different fluid dynamical effects play a role. Here the existence of one of these layers, the layer dividing the all diffusive core from the viscous region, will be proven.
This change in flow region develops along the x-axis as predicted by eq.(2.56).

$$\frac{e^{-x_c}}{LmEm} = 1 \tag{5.1}$$

In two numerical experiments, gas is pushed from the bottom end cap Ekman layer into the main compartment of the centrifuge at radial locations (far) in the diffusive region, meaning for x values larger than x_c as calculated from eq. (5.1). The gas is pushed only over a small area of the x-axis, between x = 8 and x = 10, into the main compartment; hence the term “pulse test”. According to the analytical models, it is expected that this gas will flow out of this region (a region with a very low local density) upwards, closer to the rotating wall. The stream function is expected to be influenced only by the end cap Ekman conditions in this region, not by other diffusive effects. Since the end cap conditions are anti symmetrical, this region behaves actually as an inviscid region, as discussed in Section 2.5.4. Two sets of results are presented: Table

5.1 gives the parameters for a centrifuge with a viscous region between the inner Stewartson layer and the all diffusive core (Semi-long centrifuge). Table 5.2 gives the parameters for a centrifuge with a fully developed inviscid region between the inner Stewartson layer and viscous region (Short centrifuge).

A	*E*	*L*	x_c	x_i
16.8	$3.37\ 10^{-7}$	26.7	3.2	-2.9

Table 5.1: A parameter set defining a Semi-long centrifuge to be used to verify the existence and position of the viscous core.

A	*E*	*L*	x_c	x_i
16.8	$3.37\ 10^{-8}$	6.7	6.8	2.2

Table 5.2: A parameter set defining a Short centrifuge to be used to verify the existence and position of the viscous core.

According to the analytical theory, see Section 2.5.1, if an inviscid region exists, then it is between the Stewartson layer and x_i a viscous region between x_i and x_c and the diffusive region for $x > x_c$.

The Semi-long centrifuge has a negative value for x_i and no inviscid region.

The said temperature pulse has been modelled at both end caps between *x* = 8 and *x* = 10. At the bottom end cap a temperature increase of +1 ($\theta = +1$) is defined between *x* = 8 and *x* = 10 and at the top end cap a temperature decrease of -1 ($\theta = -1$) is defined.

In essence, the Ekman boundary layer assumptions mean that locally the axial diffusion dominates over radial diffusion, Brouwers [42]. This is valid up to a radial position given by:

$$x_d << -\ln(A^2 E) .$$

For higher values of *x,* all diffusive terms (radial and axial) in the equations become important.

For the Semi-long simulation this results in $x_d \sim 9$ and for the Short centrifuge $x_d \sim 11$. This means that the pulse (between *x* = 8 and *x* = 10) in the Semi-long simulation is injected in the full diffusive area and in the simulation for the Short centrifuge in the Ekman layer itself.

The thickness of the inner Stewartson layer is of the order, eq. (2.58) x_s = O($A(LE)^{1/3}$). For the Short centrifuge this is ≈ 0.1 and ≈ 0.4 for the Semi-long, as is

indicated in Chapter 4. The real thickness is approximately four times this value at z = 0.5.

The stream function for the Semi-long simulation is presented in Fig. 5.1 at four positions along the axial axis: at z = 0.5, z = 0.1, z = 0.025 (this is well outside the Ekman layer) and just outside the Ekman layer near the bottom end cap at z = 0.0025. The same variables are reported in Fig. 5.2 for the simulation in the Short domain. Obviously, since the axial boundary conditions are symmetrical in this experiment, the same result holds for the top half of both centrifuges.

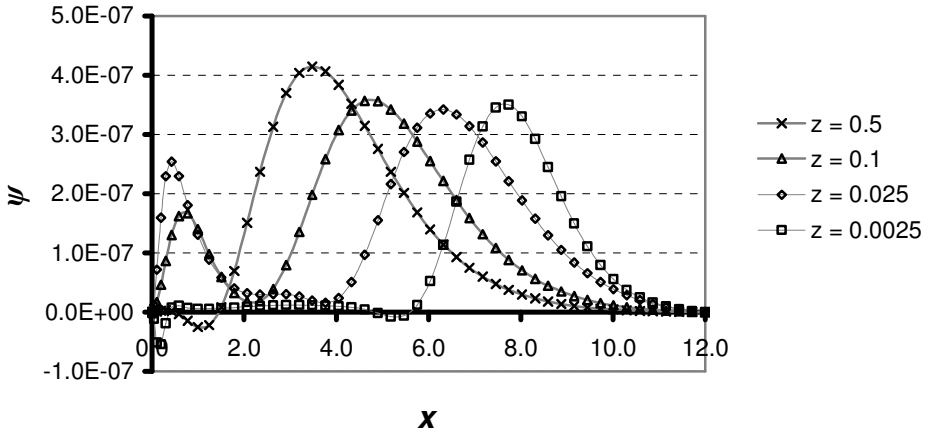

Figure 5.1: This figure illustrates the gas flow resulting from a local temperature increase at the bottom end cap between x = 8 and x = 10 and a decrease at the same location at the top end cap. The parameter set represents the case of a Semi-long centrifuge.

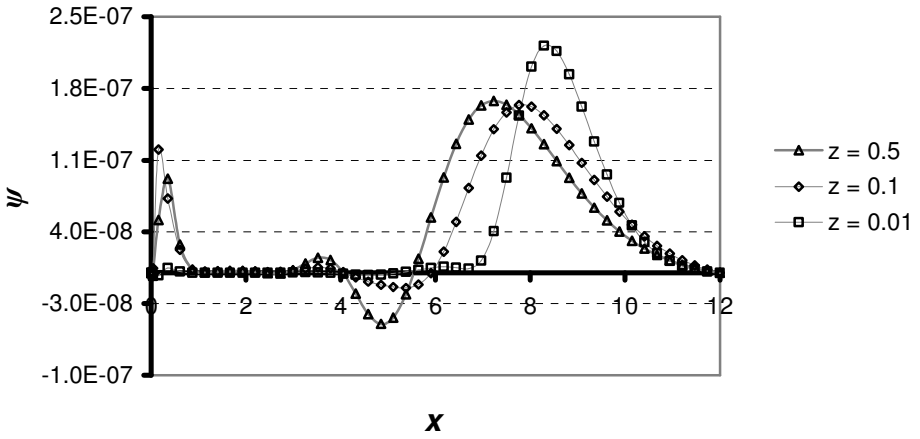

Figure 5.2: This figure illustrates the gas flow resulting from a local temperature increase at the bottom end cap between x = 8 and x = 10 and a decrease at the same location at the top end cap. The parameter set represents the case of a Short centrifuge.

In both graphs the shift of the pulse from the end cap towards $x = x_c$ is clearly visible, proving the suggestion made earlier on in this section that the gas flows preferably outside the all-diffusive core, through the viscous region.

The stream function for the Semi-long centrifuge peaks at $x \sim 3.5$, to be compared to the analytical value of $x_c = 3.2$, given in the parameter set for this simulation. The stream function peaks for the Short centrifuge at *x = 7.3*, to be compared to $x_c \sim 6.8$ in the parameter set.

Implicitly, these results are proof of the suggestion made by Brouwers [42] that the averaged (along the axial coordinate) x_c is higher than calculated from eq. (5.1) when applying Ekman suction conditions resulting in pushing gas into the main compartment at radial positions $x > x_c$.
When Ideal Ekman conditions eq. (2.62) are applied, Brouwers [42] suggests:

$$x_c^* = x_c + 0.5 \tag{5.2}$$

This implies that the averaged x_c is half an increment higher than calculated from eq. (5.1). It is this corrected core that is being used in his analytical model to calculate E_f .

In these pulse tests anti symmetrical end cap conditions were applied. According to analysis this results in behaviour of the viscous region which is very close to the behaviour of an inviscid region. This is visible in the reported pulse test for the Short

centrifuge in Fig. 5.2. The pulse does not move into the inviscid region in Fig. 5.2 but stays close to the diffusive core.
Analysis indicates that the application of anti symmetrical boundary conditions should result in the same stream function in both regions: the average of the Ekman suctions at the bottom and top, eq. (2.60) and (2.61). This is visible in the inviscid region and less clearly for the viscous region due to the pulse.

A difference in pulse width just outside the Ekman layer is visible when comparing both simulations. In Fig. 5.1, where the pulse is injected in the full diffusive region, it is already widening just outside the Ekman layer (z = 0.0025). In Fig. 5.2, with a pulse injected fully into the Ekman layer, this is much less visible (z = 0.01): radial diffusion is clearly less important at this radial position, which is the basic assumption for the Ekman layer approach.
Gas is returned from the top to the bottom along the cylinder wall via the inner Stewartson layer with a thickness ($\approx$ 0.5 and $\approx$ 1.6 at the radial *x* coordinate), very close to the values estimated earlier in of this section.

5.1.1 Flow regions in the Short centrifuge

In this section, the focus is on the flow regions in a Short centrifuge, specifically on the inviscid flow region, in between the Stewartson layer and the viscous region. Numerical results will be compared with analytical work by Brouwers [42].

A Short centrifuge will be modelled and non-symmetrical-boundary conditions will be applied by varying the temperature at the bottom end cap according to:

$$T(x) = \beta + \alpha(\sqrt{e^x}\,(1+1/4Br(1+x/A))^{3/4}\,/(1+0.25Br)^{3/4} - 1) \tag{5.3}$$

The temperature at the top end cap is assumed to be:

$$T(x) = 0$$

β is set to 1, which represents a constant temperature of +1 along the bottom end cap. The parameter α has been increased from 0 to 0.3 in three steps. Note that by applying $\beta = \alpha$ = 1 this would result in a (one sided) boundary condition driving an ideal flow according to eq. (2.60) and eq. (2.61).

The applied boundary conditions resulting from eq. (5.3) is illustrated in Fig. 5.3.

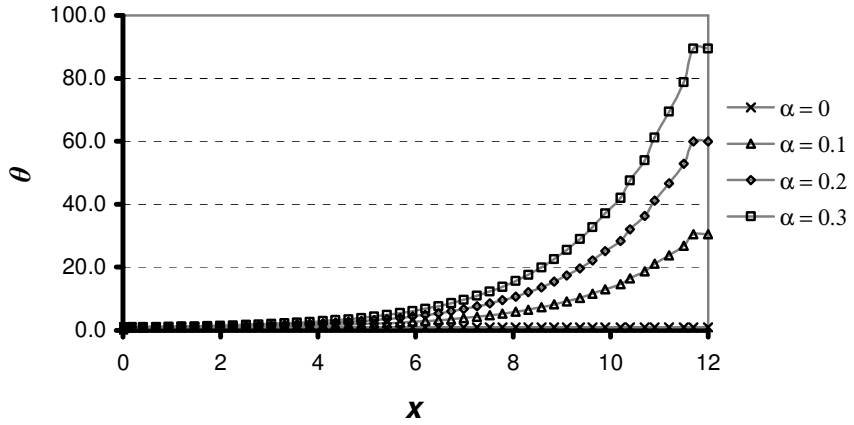

Figure 5.3: The temperature at the bottom end cap for four different boundary conditions.

In Table 5.3 the parameter set for this simulation is given:

A	*E*	*L*	x_c	x_i
16.8	$3.2\ 10^{-8}$	3.0	7.7	3.8

Table 5.3: This parameter set for a Short centrifuge will be used to demonstrate the dependence of the flow in the inviscid region on the boundary condition at the bottom end cap.

The Stewartson layer has a thickness, eq. (2.58), $x_c \sim A(LE)^{1/3} \sim 0.08$, which implies an actual layer thickness $\approx$ 0.3. The inviscid region is between this Stewartson layer and $x_i \approx 3.8$, subsequently the viscous region upto $x_c \approx 7.7$.

The radial distribution of the stream function at z = 0.5 is shown graphically in Fig. 5.4. The stream function in the inviscid region is increasing with higher values of α. The calculations imply that gas is pushed from the viscous core and from the inviscid region into the viscous region and flows mainly around the position where the core develops: $x_c = 7.7$.

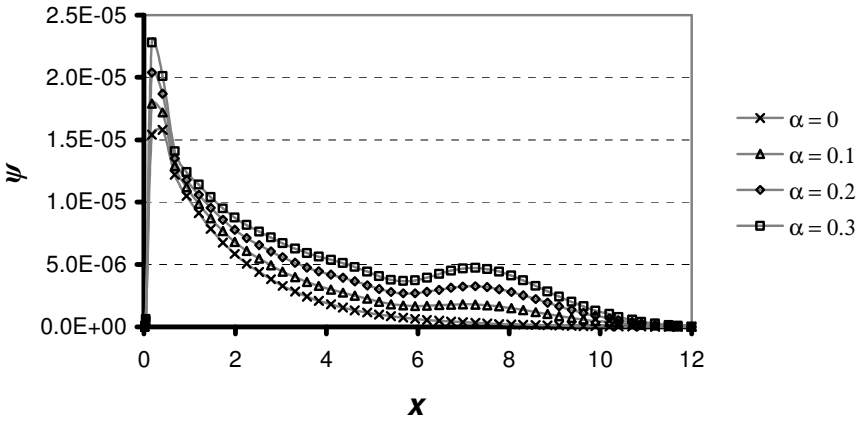

Figure 5.4: Radial distribution of the stream function ψ in a Short centrifuge at z = 0.5 resulting from four different boundary conditions at the bottom end cap.

The Stewartson layer, returning the flow from the top to the bottom along the wall is clearly visible.

The axial distribution of the stream function in the inviscid and viscous region along the *z* axis is presented In Fig. 5.5 and Fig. (5.6).

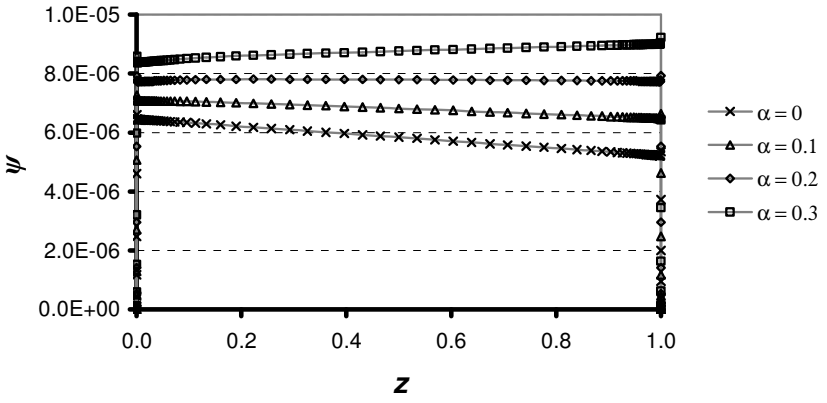

Figure 5.5: The axial distribution of the stream function ψ along *the z – axis at x ≈ 2, in the inviscid region, for four different bottom end cap boundary condition.*

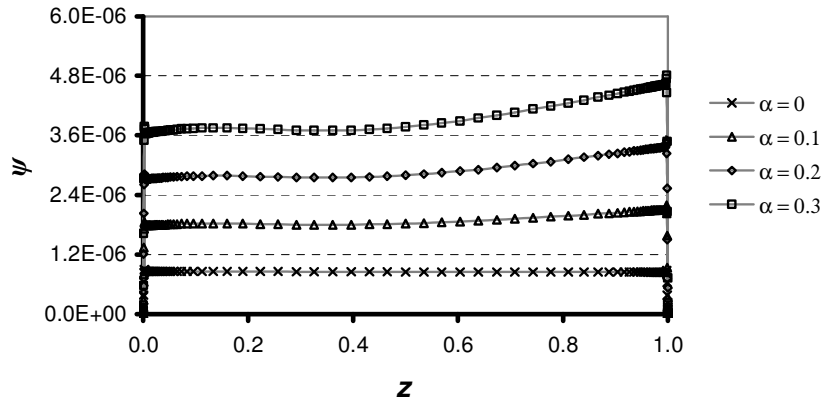

Figure 5.6: The axial distribution of the stream function ψ along *the z – axis at x ≈ 5.5, in the viscous region, for four different bottom end cap boundary condition.*

Fig. 5.5 illustrates increasing values of ψ along the axial coordinate when α increases. This implies negative values for the radial velocity u and means that gas flows from the inviscid region towards the viscous region. The increasing values of ψ along the axial coordinate in Fig. 5.6, implies negative values of the radial velocity u in the viscous region as well, indicating that the gas is pushed from this region towards the diffusive area. This flow pattern in the inviscid region is not in line with the analytical predictions, eq. (2.60). Contrary to the analytical predictions, ψ in the inviscid region is not constant along the axial coordinate but varies with varying boundary condition at the bottom end cap.

An explanation of this unexpected behaviour (compared to analytical predictions) can be found by presenting a combined parameter of the angular velocity and temperature, in line with the definition in eq. (2.59):

$$\chi(x) = \omega(x) - 0.5\theta(x) \tag{5.4}$$

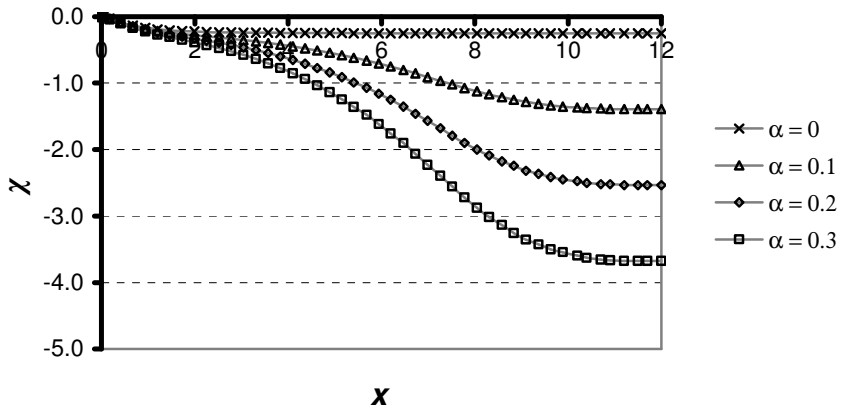

Figure 5.7: The radial distribution of the variable $\chi(x)$ *as defined in eq. (5.4) at z = 0.5 for four different boundary conditions.*

This combined parameter is given in Fig. 5.7 at $z = 0.5$. According to Brouwers [42] the second derivative to x of this parameter should be close to 0 in the inviscid region. The presented numerical data indicates that the second derivative of this variable in the inviscid region, $x \approx 0.3$ to $x \approx 3.7$, is not negligible as assumed in the analytical work: the data shows a convex or concave trend, depending on the boundary conditions at the bottom end cap. Adjusting the various flow parameters (stream function, angular velocity and temperature) in both flow regions is apparently spread over a significant radial distance and dominates the flow in both the inviscid and viscous region, resulting in increasing or decreasing stream function values in the inviscid flow region. Fig. 5.8 illustrates the gas flow in a Short centrifuge.

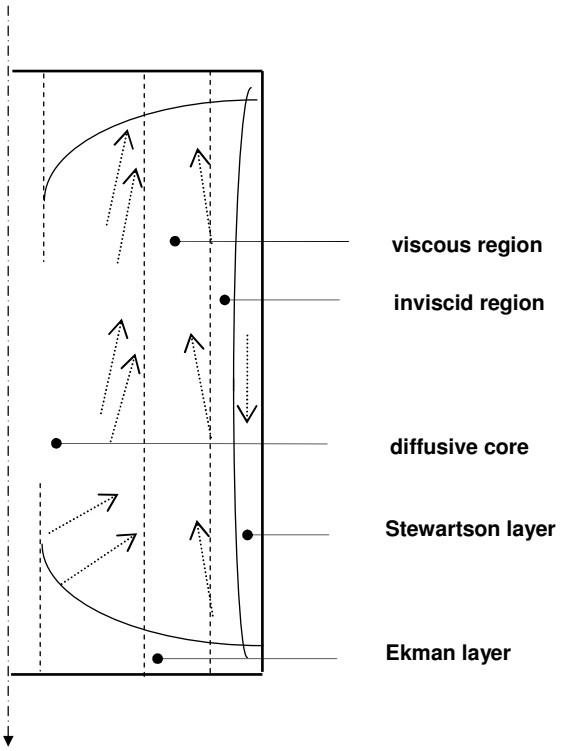

Figure 5.8: Illustration of the gas flow in a Short centrifuge relative to the flow regions, applying a one sided drive mechanism at the bottom end cap.

5.2 Mapping the numerical results

During the numerical experiments (as would be the case for real experiments), a number of physical parameters can and will be varied: the wall velocity, the wall pressure, the radius and the cylinder length. They are grouped in dimensionless variables: the velocity parameter (*A)*, the Ekman number (*E*) and the dimensionless length (*L*). The analytically calculated flow efficiency factor has been presented by Brouwers [42] in a two-dimensional graph: flow efficiency against *A* for different values of x_c . This is considered a breakthrough in centrifuge development and has contributed to the successful development of the centrifuge project in Europe.
Unlike previous graphical reporting of flow efficiency calculated against *A* for varying values of x_c , Brouwers [42] shows all important factors in a single, two-dimensional graph, rather than several interrelating plots. He clearly shows the high flow efficiency for Semi-long centrifuges compared to the Long designs. According to [47], the European design is a strong competitor in the separation market, anno 2009.

In this section, a different presentation will be introduced, resulting in a one-dimensional presentation of the flow efficiency versus dimensionless variables. Two new parameters are defined for this: E_f^* and x_{cc} . These definitions will be used to make calculated results less depending on the velocity parameter (A), enabling a simpler presentation of results compared to previous works, e.g. Brouwers [3].

The flow efficiency equation as presented in Appendix A, eq. (A92) is given:

$$E_f = \frac{2\left[\int_0^A \psi(x)dx\right]^2}{A\int_0^A \frac{[\psi(x)]^2}{(1-x/A)}dx} \qquad [-]$$

Initially, it is concluded that results are less depending on the velocity parameter (*A)* by defining a new variable:

$$E_f^* = E_f * A$$

This results in:

$$E_f^* = \frac{2\left[\int_0^A \psi(x)dx\right]^2}{\int_0^A \frac{[\psi(x)]^2}{(1-x/A)}dx} \qquad [-] \qquad (5.5)$$

E_f^* will be referred to as the “Scaled flow efficiency”. Furthermore, as can be seen from the right hand side term, the velocity parameter *A* has a secondary effect on the results as well: an increase of *A* will increase the calculated value of E_f^* in eq. (5.5) for what would otherwise be the same functions for ψ . To compensate for this effect, the position where the diffusive core develops: x_c , will be redefined. The core position x_c is expected to play a major role as discussed in the previous section:

$$x_c = -\ln(\ LmEm\ )$$

and is modified as follows:

$$x_{cc} = -\ln\left(LmEm\ /\ A\right) = -\ln(ELA^2) \qquad (5.6)$$

This empirical result proves to be a useful correction factor, as will be shown in the next sections where calculated results by eq. (5.5) will be presented versus this coordinate.

All calculations in the next sections were done by applying 50 radial and 100 axial cells and by setting the fictitious centreline to $x = 12$.

It should be noted here that this presentation of results is a simplification. However, a simple engineering tool emerges, as will be illustrated in the following sections. It helps us to focus on the main factors determining the efficiency of a centrifuge. In reality the three parameters: Ekman number (*E)*, velocity parameter (*A)* and the dimensionless length (*L)* as well as various combinations of these parameters play a role. Therefore, some spread or jigging in results is expected when presenting results as derived in this section. The strength of the approach is that it enables to estimate the separation efficiency of a centrifuge with an accuracy of 5 – 10%, subject to boundary conditions applied. Jigging or spread would be minimised if the corrected core position would be varied by only one parameter, e.g. the wall pressure.

5.3 Ideal Ekman suction conditions

In this section the results of an overall parameter study are presented by mapping the calculated flow efficiencies in a single line graph. E_f is calculated for a number of centrifuges applying the ideal Ekman suction condition at both end caps. The intrinsic flow strength (m^*) is calculated according to Eq. (A94). The flow efficiency (E_f) in the top three simulations in Table 5.4, which are Long centrifuges, has been calculated by assuming a linear wall temperature gradient drive and simple conditions along the end caps.

In Table 5.4 both the core and inviscid core positions are given.

A	E	L	x_c	x_i	E_f	m^*
[-]	[-]	[-]	[-]	[-]	[%]	[-]
67.2	$1.7\ 10^{-7}$	133.3	-1.9	-11	12.8	3.8
7.2	$1.7\ 10^{-7}$	53.3	-1.0	-9	12.9	9.1
67.2	$1.7\ 10^{-7}$	26.7	-0.3	-7.8	12.9	16
67.2	$1.7\ 10^{-8}$	133.3	0.4	-9	13.4	151
37.8	$2.2\ 10^{-7}$	26.7	1.1	-5.7	24.2	99
16.8	$6.7\ 10^{-7}$	26.7	2.5	-1.3	57.2	287
67.2	$3.4\ 10^{-8}$	26.7	1.3	-6.1	14.3	159
16.8	$3.4\ 10^{-7}$	26.7	3.2	-2.9	62.7	139
67.2	$1.7\ 10^{-8}$	26.7	2.0	-5.5	15.4	227
37.8	$2.8\ 10^{-8}$	26.7	3.2	-4.1	30.4	221
37.8	$2.2\ 10^{-8}$	26.7	3.4	-3.4	31.5	294
67.2	$1.7\ 10^{-8}$	6.7	3.4	-2.7	18.5	204
16.8	$3.4\ 10^{-8}$	26.7	5.5	-0.6	77	397
16.8	$3.4\ 10^{-8}$	13.3	6.2	0.8	80	396
16.8	$3.4\ 10^{-8}$	6.7	6.8	2.2	82.3	396

Table 5.4: A parameter set defining centrifuges in three domains. The calculated results of this set will be used to demonstrate the usefulness of eq. (5.5).

The simulations as presented in Table 5.4 represent a very wide parameter study from Long to Short centrifuges.

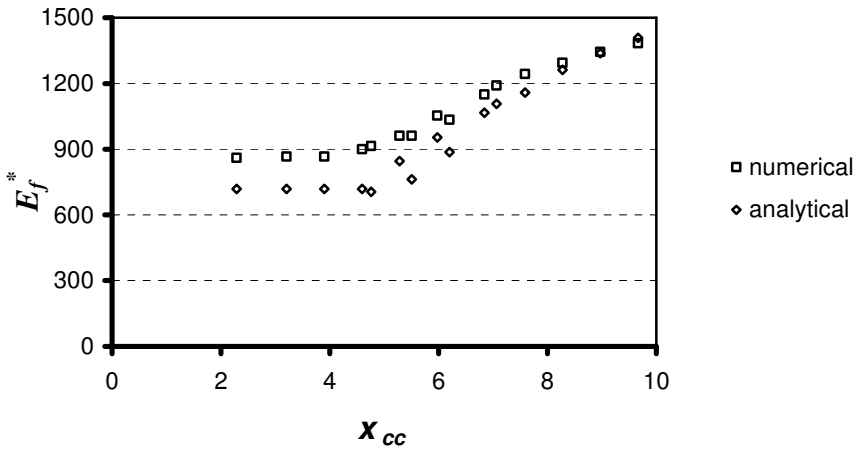

Figure 5.9: The Scaled flow efficiency, E_f^*, versus the corrected core position, x_{cc}. Results for Short, Semi-long and Long centrifuges are collected in one graph. A constant gradient along the wall for the Long centrifuge is applied and IBC in the Semi-long and Short domain.

Fig. 5.9 shows numerical results versus the analytical results of Brouwers [42]. The Scaled flow efficiency is constant up to approximately x_{cc} = 4 and subsequently increasing by some 100 units per increment. The comparison between the analytical model and the current results are good and improve even further at higher values of the corrected core position, which are the "Semi-long" and "Short" centrifuges.

Three calculations at the lowest x_{cc} values refer to Long centrifuges. In the analytical model only the lowest eigenfunction, eq. (B15) is used in this domain. It results in somewhat under predicting the flow efficiency, as illustrated in Fig. 5.9, by about 15%, compared to the numerical value. The plateau value of the Scaled flow efficiency in Fig. 5.9 is approximately 820, while the analytical limit case is 720, eq. (B17). The overall efficiency calculation of these three centrifuges is dominated by radial diffusion as can be seen from the calculated core values, x_c in Table 5.4, which show negative values. An example of the numerically calculated stream function versus the first eigenfunction, eq. (B15) is given in Fig. 5.10, assuming the parameter set given in Table 5.5.

A	E	L	x_c	x_i	E_f
[-]	[-]	[-]	[-]	[-]	[%]
67.2	0.0	133.3	-1.9	-11.0	12.8

Table 5.5: A parameter set defining a Long centrifuge. The data set is used to compare numerical calculated results versus analytical results applying only the first eigenfunction.

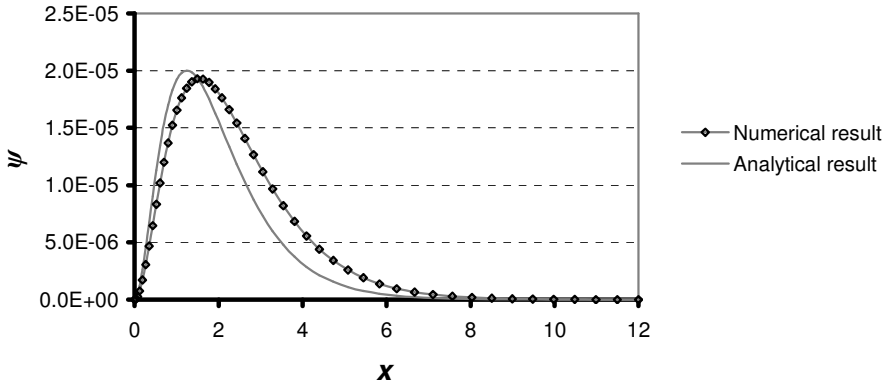

Figure 5.10: Radial distribution of ψ at z = 0.5 for a Long centrifuge. Analytical (lowest eigenfunction) and Numerical results are presented.

As can be understood from Fig. 5.10, the numerical model predicts a somewhat wider stream function profile, resulting in the higher flow efficiency compared to the analytical limit case. Three more simulations have been executed to confirm the plateau level and the effect of the wall velocity. The core position x_c is kept constant at ≈ -1, the velocity parameter (*A)* was varied from ≈16 to ≈ 67, see Table 5.6.

A	E	L	x_c	x_i	E_f	E_f^*	x_{cc}
[-]	[-]	[-]	[-]	[-]	[%]	[-]	[-]
67.2	$8.4\ 10^{-8}$	106.7	-1.0	-11.0	12.2	819.2	3.2
37.8	$2.2\ 10^{-7}$	240.0	-1.1	-11.0	21.3	805.2	2.6
16.8	$6.0\ 10^{-7}$	1000.0	-1.0	-11.0	45.5	763.9	1.8

Table 5.6: Three parameter sets, defining Long centrifuges. The data set is used to explicitly demonstrate the effect of A on E_f .

The overall effect on E_f^* is obvious, the plateau level at lower velocities approaches the analytical value of 720 and increases at higher values of *A*. This velocity effect is fully due to the term containing the velocity parameter *A* in the nominator of eq. (5.5). The overall differences between the analytical and numerical values are not dramatic, up to some 15% at very high velocity parameters (*A* ≈ 67). For simplification purposes an averaged plateau value for the scaled flow efficiency of 800 can be assumed for corrected core positions below x_{cc} ≈ 4, see Fig. 5.9.

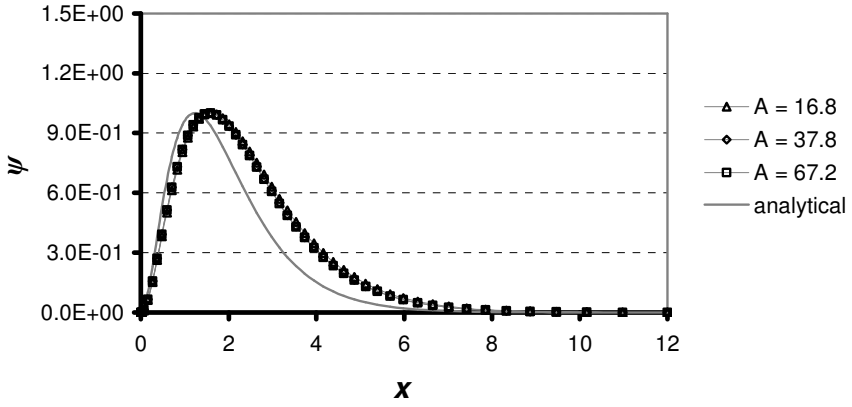

Figure 5.11: Radial distribution of ψ at z = 0.5, *for identical centrifuges in the Long domain, only A is varied.. The analytical result is the 1st eigenfuntion.*

The stream function for the three simulations given in Table 5.6 is presented in Fig. 5.11 and the axial profile of E_f in Fig. 5.12. The data has been normalised and is virtually identical, demonstrating that curvature effects are neither existent nor axial effects.

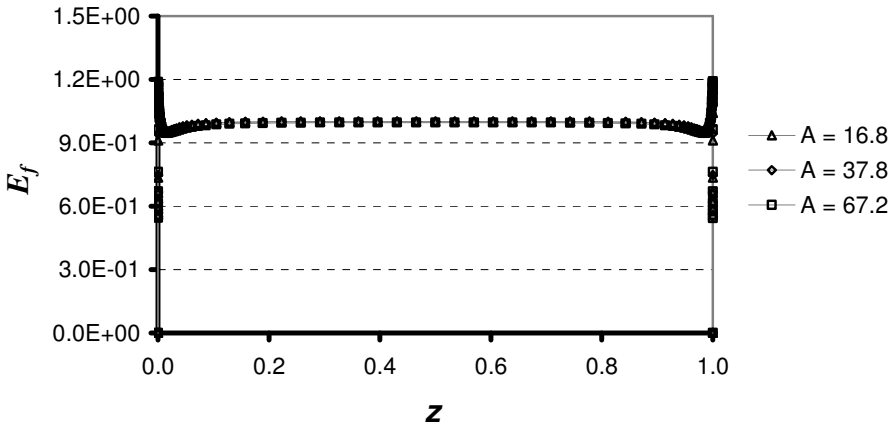

Figure 5.12: Normalised E_f along the z-axis for three values of A for otherwise identical centrifuges in the Long domain.

Considering all the simplifications that are included in presenting the results (the scaled flow efficiency versus corrected core position) in these figures, it is concluded that the correlation is very strong. Apparently these parameters are the dominating ones for these applications of a gas centrifuge and are sufficiently accurate to be used as an engineering tool. Accordingly, this style of presentation will be used in the next sections since it maps all calculated results sufficiently accurate (5 – 10 % accurately) in a single graph.

5.4 Semi Ideal Ekman suction conditions

In this section, a sub-optimal, but technically feasible, driving mechanism will be modelled and its simulated results presented.
The ideal model as discussed in previous sections has a drive characteristic proportional with $\sqrt{e^x}$, compensating for the reducing effectiveness of the Ekman layer suction, along the x - axis towards the centreline.
In reality, this drive model is very difficult to realise at the top end cap since it would mean a decreasing temperature towards the centreline and/or an increasing rotational velocity towards the centreline.

The same bottom end cap drive as introduced in the previous section is applied and a temperature (-1) at the top end cap. The parameter set given in Table 5.4 is applied.

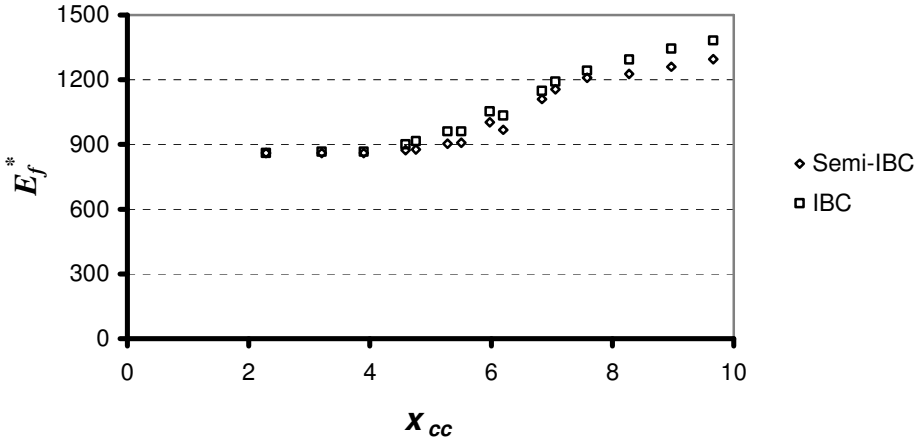

Figure 5.13: Parameter study comparing E_f^* for Semi-IBC and IBC (as in Fig. 5.9) results versus the corrected core position.

Fig. 5.13 shows the scaled flow efficiency, E_f^*, versus the corrected core position, x_{cc}, for Short, Semi-long and Long centrifuges while applying a constant gradient along the wall for the Long centrifuges and one-sided Ideal Ekman conditions at the bottom end cap for the others. The results are compared with the numerical IBC results as presented in Fig. 5.9. At higher values of the corrected core position, slight discrepancies are observed due to the less than ideal Ekman suction conditions. The flow in the Long centrifuges is fully driven by the temperature gradient along the cylinder wall. Obviously, this is not influenced by changing the Ekman suction conditions along the end caps, for these centrifuges there is no change in calculated efficiency.

5.5 Simple Ekman suction conditions

Fig. 5.14 shows the results of simulations of simulations for which a simple end cap drive, SBC, is applied: constant temperatures at the bottom end cap (+1) and top end cap (-1). The results are compared with the simulations from 5.9.

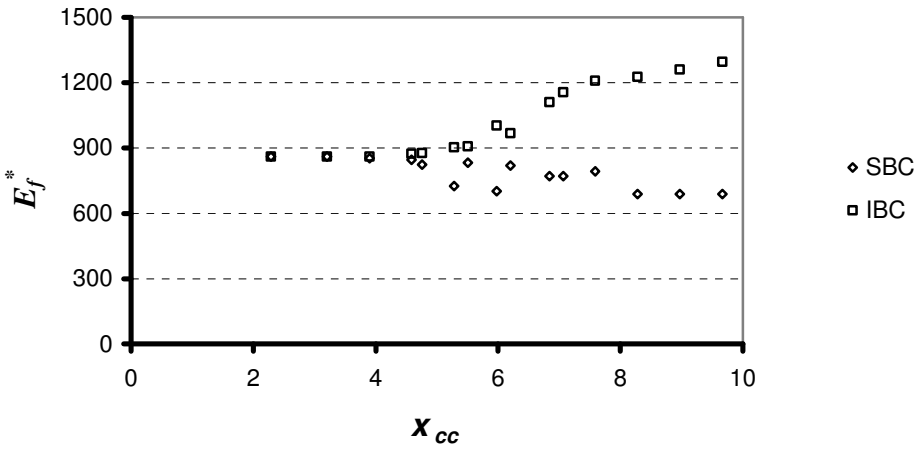

Figure 5.14: Parameter study comparing E_f^* for Short, Semi-long and Long centrifuges. The driving mechanism for the internal flow is SBC: $\Delta\theta = 2$ between the end caps, results are compared with IBC, Fig. 5.9.

Here, a widening gap between the Ideal drive conditions, IBC, and the calculated results is observed towards higher x_{cc} values. The statement in Section 5.4 concerning Long centrifuges is here applicable as well.

5.6 Reduced Semi ideal Ekman suction conditions

The Ideal Ekman suction at the bottom end cap results in very high temperatures towards the centreline. In this section, this profile will be moderated and the effect on E_f studied.

A	*E*	*L*	x_c	x_i	E_f
[-]	[-]	[-]	[-]	[-]	[%]
16.8	$3.37\ 10^{-8}$	26.7	5.5	-0.6	41

Table 5.7: Parameter set defining a Semi-long centrifuge and applying SBC. The data set is used to demonstrate the effect of less than ideal Ekman suction conditions on E_f .

In Fig. 5.9, a series of simulations are reported whereby the temperature profile at the bottom end cap has been varied according to:

$$T(x) = \beta + \alpha((e^{x})^{1/2}(1+1/4Br(1+x/A))^{3/4}/(1+1/4Br)^{3/4} - 1) \tag{5.7}$$

The temperature at the top end cap is:

$$T(x) = -1$$

β is set to 1, which represents a constant temperature of + 1 along the bottom end cap and the parameter α has been varied between 0 to 1 in four steps. All other parameters for these simulations are presented in Table 5.7. The results for E_f are given in Fig. 5.15.

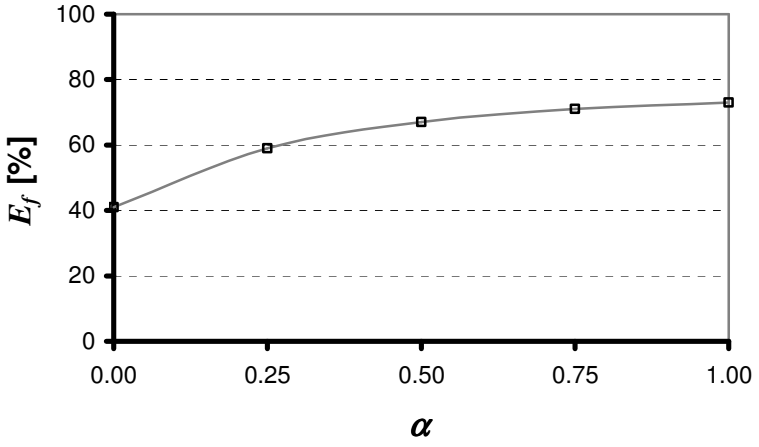

Figure 5.15: E_f for a Semi-long centrifuge as a function of the drive mechanism. In four steps the drive mechanism is approaching a Semi-IBC. The temperature at the top end cap is: $\theta|_{z=1} = -1$.

The results clearly indicate a substantial improvement when the bottom conditions approach the ideal profile to some extent.

In the next section, a second modified drive model will be applied. The same centrifuge parameters will be applied.

5.7 Cut Off Semi Ideal Ekman suction

In the previous section, a reduced Ideal Ekman suction was applied to the bottom end cap. Approaching the ideal profile at the bottom end cap to some extent reveals most of the potential flow efficiency. However, the exponential temperature profile at the bottom end cap as given by eq. (5.7) results in high values close to the centreline.

In this section, the ideal Ekman suction profile will be applied as in the previous section, eq. (5.7) with α and β both set to 1; however, a hard cut-off at some temperature level will be applied. If the local dimensionless temperature, as calculated from eq. (5.7) exceeds a given value, then the temperature is kept at this level for the remaining section of the end cap. The cut-off levels have subsequently been set at values 5, 10, 20, 40, 80 and 160.

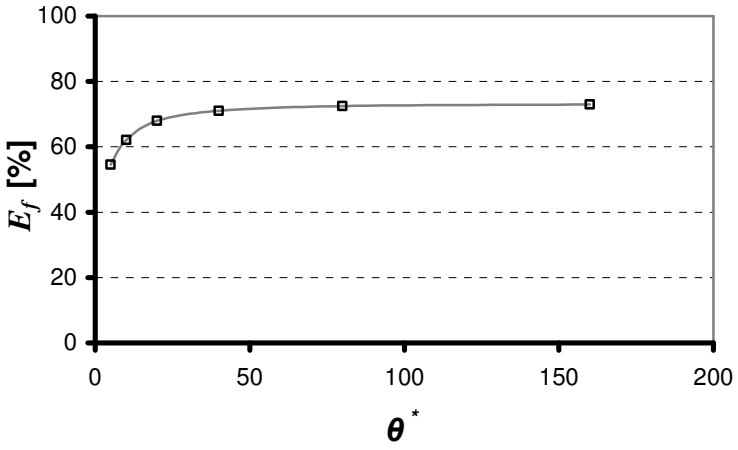

Figure 5.16: E_f for a Semi-long centrifuge as a function of the drive mechanism. The drive mechanism is a Semi-IBC, cut off at a certain temperature: θ^*. The temperature at the top end cap is $\theta|_{z=1} = -1$.

Fig. 5.16 indicates the potential for this Semi-long centrifuge to achieve a significant performance improvement by applying an appropriate drive at the bottom end cap. If the drive mechanism is not performing optimally, then a considerable drop in performance compared to the maximum obtainable flow efficiency is observed. This makes the design of a centrifuge operating in this parameter range much more challenging than a centrifuge operating in the Long domain.

5.8 Conclusions

Applying a pulse test, Section 5.1, to a Semi-long and Short centrifuge reveals and proves the existence of the core as predicted by analytical work of Brouwers [42].

Further analysis of the flow structures in a Short centrifuge reveals that the resulting flow in the inviscid region is not only determined by its Ekman conditions as well as by the boundary conditions outside the inviscid region as well e.g. in the viscous and diffusive region.

Next, a new presentation of calculated flow efficiency is developed. It shows all calculated results in a single line graph. Comparing the analytical and numerical model shows good agreement for the Ideal Ekman suction drive cases, specifically in the Semi-long and Short domain.
For IBC, the scaled flow efficiency is constant up to a corrected core position of $\approx$ 4.5 and subsequently increases $\approx$ 100 units per increment of the corrected core position.

Deviating from the ideal case: Semi-ideal, and subsequently, simple Ekman drive models such as constant temperatures between the end caps, show a gap in the predicted efficiency. This demonstrates that it will be difficult for these designs to realise the full or near full potential in terms of separation power, unless specific design measures are taken.

A considerable loss of performance is observed as well when the temperature at the bottom end cap is cut off at realistic values.

The analytical model, Brouwers [42], applies only the first eigenfunction, in the Long domain. This approach undervalues the performance in terms of E_f by some 10% compared to numerically calculated values.

Chapter 6

The effect of the Brinkman number in the Semi-long domain

Summary

The resulting set of linear fluid dynamic equations for a gas rotating at a high speed is very symmetrical in terms of temperature and angular velocity, Appendix A, eq. (A79) and (A80). The symmetry is both in terms of the equations for these variables themselves as well as how they appear in the equation for vorticity, eq. (A77). This symmetry deteriorates at higher wall velocity since *Br* and *A* both scale with v_w^2 . The effect of the velocity parameter on E_f in the Long domain has been discussed in the previous chapter. In this chapter the focus is specifically on the effect of the Brinkman number on E_f in the Semi-long domain.

Wall velocities at 500m/s correspond to *Br* ≈ 2 and at a velocity of 1000 m/s correspond to *Br* ≈ 8. In the Ekman suction equation a compensation for the value of the Brinkman number is imbedded according to eq. (2.60) and eq. (2.61), the Ekman suction condition for the inviscid area:

$$\psi = \frac{1}{4}(1-x/A)/(1+1/4Br(1-x/A))^{3/4}(Ee^{-x})^{1/2}(F_t - F_b) \tag{6.1}$$

Here, Ft and Fb are the boundary values for temperature and for angular velocity along the end caps. In the coming sections a temperature distribution at the bottom end cap is modelled according to the suction condition $\theta \sim \sqrt{e^x}$, with no angular velocity distribution. No driving mechanism is modelled at the top end cap. Applying eq. (6.1), this choice of the boundary value at the bottom end cap results in an Ekman suction relation represented as follows:

$$\psi(x) = 1/4E^{1/2}(1-x/A)/(1+1/4BR(1-x/A))^{3/4} \tag{6.2}$$

The Ekman suction approach is valid up to the radial coordinate where all diffusive terms become important, which is according to Brouwers [3]: $x_d \sim -\ln(A^2E)$. The Ekman boundary layer has a thickness at this radial coordinate of $\delta \approx 1/AL$.

In this chapter, two series of results are reported to study the effect of the Brinkman number:

- In Section 6.1, centrifuges will be modelled and the Brinkman number will be set at 1 and respectively 10. The Brinkman number mathematically relates to the velocity parameter (*A)*, here it will be set to these values in order to be able to focus directly on the effect that this parameter has on the resulting flow efficiency and flow strength

- In Section 6.2, a series of calculations will be performed by applying a simple mechanical drive model (the bottom end cap rotating at a lower angular speed) and a simple thermal drive model (the bottom end cap increased in temperature). The Brinkman number again is set at 1 and 10. This will reveal if, at high Brinkman numbers, temperature and angular speed drive are still interchangeable in terms how they affect the internal flow.

6.1 Model simulations

In this section, numerical calculations are reported to study the effect of the Brinkman number. All other dimensionless parameters will be kept constant during this study.

The thermal parameters are set in such a way that there is no conduction of heat in the cylinder wall or end caps and the heat transfer parameters are set at very high values.

The numerical domain is stretched to x = 12, the fictitious centreline, and the standard numerical model is applied as defined in Chapter 4.

The parameters applied to model a Semi-long centrifuge as well as the simulation results are given in Table 6.1. The intrinsic flow strength m^* has been calculated according to eq. (A94).

Simulation	*A*	*E*	*L*	Br	x_c	E_f	*m**
[-]	[-]	[-]	[-]	[-]	[-]	[%]	[-]
1	16.8	$3.9\ 10^{-7}$	40	1	2.6	53.8	119
2	16.8	$3.9\ 10^{-7}$	40	10	2.6	54.6	54
3	16.8	$3.9\ 10^{-8}$	40	1	2.6	69.2	302
4	16.8	$3.9\ 10^{-8}$	40	10	2.6	69.5	153
5	16.8	$3.9\ 10^{-7}$	10	1	4	14.8	281
6	16.8	$3.9\ 10^{-7}$	10	10	4	15.3	117

Table 6.1: Parameter set defining Semi-long centrifuges. The data set is used to demonstrate the effect of varying the Brinkman number on both E_f and m.*

From these results it can be concluded that:

- the Brinkman number has a marginal effect on E_f. Higher Brinkman numbers result in a somewhat higher E_f
- the Brinkman number has a very strong effect on *m**. Higher Brinkman numbers results in much lower values for m^*.

In the following sections, the results of simulations 1 and 2 given in Table 6.1 will be analysed in greater detail.

6.1.1 High and low Brinkman number simulations

The parameter set of simulation 1 and 2 given in Table 6.1 result in the following characteristics for a Semi-long centrifuge:

- Stewartson inner layer thickness, eq. (2.58): $x_s \approx 0.4$
- Ekman layer thickness at $x = 0$ $\approx$ 1.510^{-5}
- the validity of the Ekman layer ends at $x = x_d = -\ln(A^2 E) \approx 9$
- an inviscid area would exist between the Stewartson layer at the wall and a location given by $x_i = -\ln(EL^2 A^4) \approx -3.9$, meaning that no inviscid area exists, in these simulations
- the radial position where the diffusive core starts is $x_c = -\ln(ELA^3) \approx 2.6$. This is in the Semi-long domain. Analytical models predict that ψ will vary linearly along the *z*- axis.

6.1.2 Ekman suction

In Fig. 6.1 the results of the numerical calculations and the analytical Ekman suction equation for high and low *Br* numbers are presented.

The numerical results are presented at the axial coordinate position $z = 10^{-3}$, which is approximately the thickness of the Ekman layer at x = 9, where, the validity of the analytical results end.

The results show a strong correlation between the numerical and analytical values. They are well ($\approx$ 10% accuracy) in line with each other. The effects of diffusion are visible from $x \approx 7$ onwards, about 2 increments before the mentioned criterion.

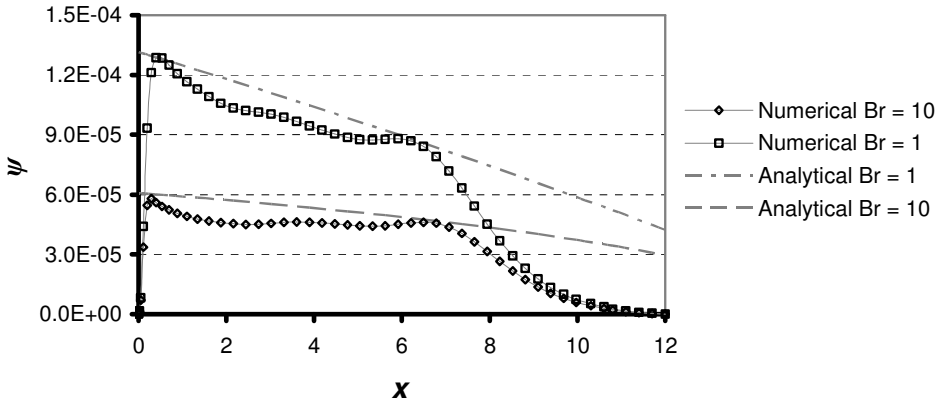

Figure 6.1: Analytical Ekman layer results and numerically calculated values for high and low Brinkman numbers. The parameter sets given in Table 6.1, simulations 1 and 2, have been applied

The effect of diffusion on the Ekman suction is simulated by varying the Ekman number by more than one order in magnitude. Three cases are considered, which are given in Table 6.2.

Simulation	*A*	*E*	*L*	x_d	x_s	x_c
[-]	[-]	[-]	[-]	[-]	[-]	[-]
1	67.2	$1.9\ 10^{-7}$	10	7	0.84	0.5
2	16.8	$3.9\ 10^{-7}$	40	9	0.42	2.6
3	16.8	$4.8\ 10^{-8}$	40	11	0.21	4.7

Table 6.2: Parameter set defining Semi-long centrifuges. The data set is used to compare numerically and analytically calculated Ekman layers for high and low Brinkman numbers.

As can be seen from the values of x_c and x_s, the three cases are very different in nature:

- the thickness of the Stewartson layer follows from $x_s = A(LE)^{1/3}$. As discussed before the real thickness is ≈ 4 times this parameter. As can be seen in Table 6.2, the layer thickness is expected to vary a factor four in these three simulations
- simulation 1 represents the case of a Semi-long centrifuge although it is close to the Long domain since x_c = 0.5. This is well within the Stewartson layer, which extends up to *x* ≈ 3 at the mid plane. A stream function profile is

expected to develop close to the one as shown in Fig. 5.6. The second centrifuge is within the Semi-long domain. It has still a very thick Stewartson layer at $z = 0.5$, up to $x \approx 1.6$, almost touching the core position at $x \approx 2.6$. The third centrifuge is expected to develop a clear Stewartson layer up to $x \approx 1$ near the wall and a strong flow close to the core position, at $x \approx 4.7$.

ψ values, just outside the Ekman layer, are given in Fig. 6.2. The effectiveness of the Ekman suction reduces systematically for $x > x_d - 2$.

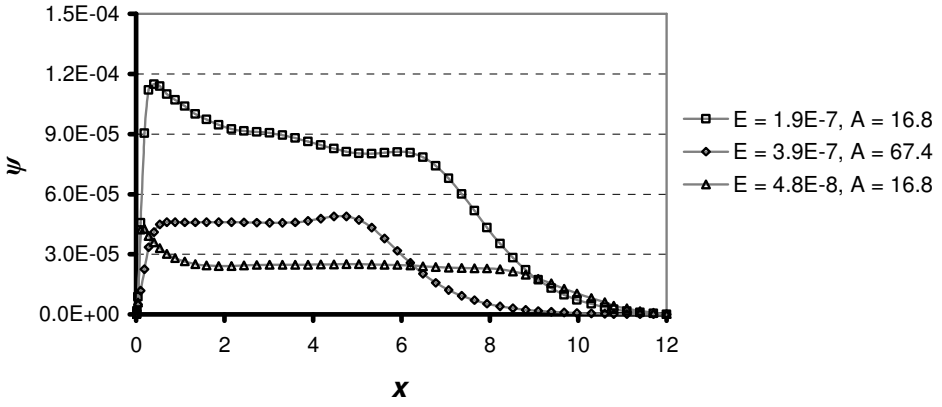

Figure 6.2: Numerical results illustrating the Ideal Ekman suction for three different Ekman numbers, at z = 0.0015, just outside the Ekman layer.

The maximum thickness of the Ekman layer is predicted by analysis: $\delta \approx 1/AL \approx$ 0.0015. This is the same for all three simulations. To prove that the layer is not further expanding in radial direction, at higher values of the axial coordinate, the results of the same simulations have been repeated in Fig. 6.3 at four times the thickness of the Ekman layer $z \approx 0.006$. As can be seen from this figure, the profiles do not extend to higher values along the radial position. The all-diffusive core prevents further growth of the Ekman layer towards the centreline. The ψ profiles develop in a different pace for the three simulations, depending on the position of the core. The “Longest” centrifuge develops fastest, the “Shortest” slower.

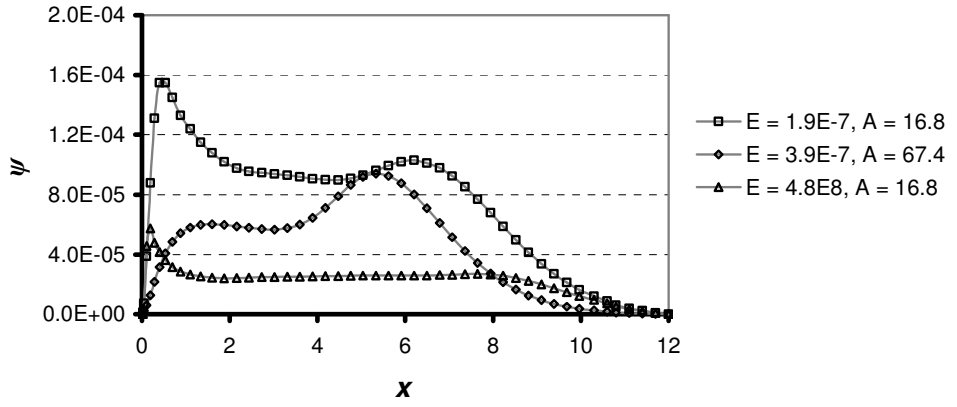

Figure 6.3: ψ profiles *resulting from Ideal Ekman suction for three different Ekman numbers, at z = 0.006, some distance from the Ekman layer.*

In Fig. 6.4 the results are presented at the mid plane position, $z = 0.5$, to illustrate the very different nature of the three centrifuges in these simulations:

- the two centrifuges with the low velocity parameter (*A)* develop a ψ profile with a peak value at the the core position. Simulation 3 shows this very clearly, since the peak is far from the Stewartson layer, at $x \approx 4.7$
- the high velocity centrifuge develops a ψ profile close to the one presented before in Fig. 5.11.

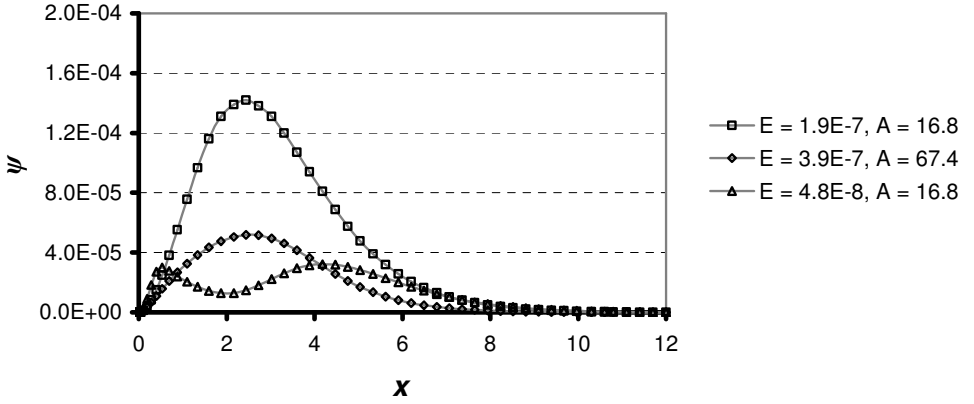

Figure: 6.4, ψ profiles *resulting from Ideal Ekman suction for three different Ekman numbers, at z = 0.5.*

6.1.3 Flow efficiency and flow strength

The calculated flow efficiency E_f and intrinsic flow strength *m** are presented as a function along the *z* axis in Fig. 6.5 and Fig. 6.6. Fig. 6.5 shows the decrease in E_f from the bottom end cap upwards. The gas flow is directed into the main compartment by the Ideal Ekman suction over a large area of the radial axis close to the bottom end cap. Subsequently it is forced to flow closer to the wall in a region between the inner Stewartson layer and viscous core, as discussed in Chapter 5. There is hardly any difference in E_f for both Brinkman numbers.

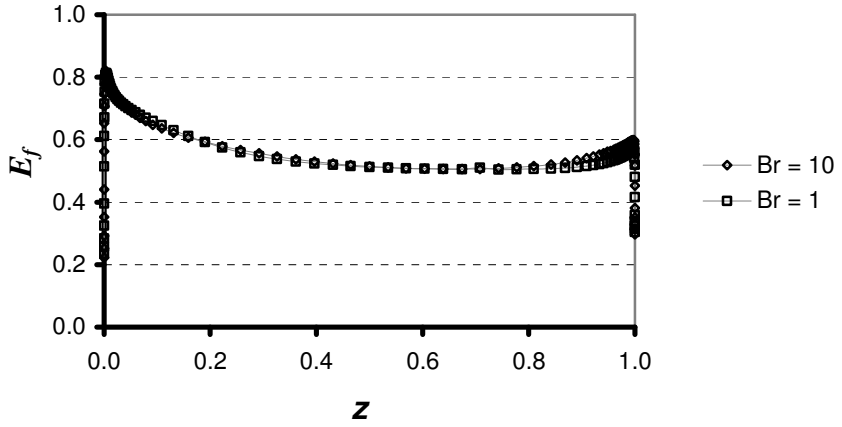

Figure 6.5: Axial distribution of the flow efficiency E_f along the z- axis for high and low Brinkman numbers. The drive mechanism is Semi-IBC at the bottom and no drive at the top end cap. The parameter sets given in Table 6.1, simulations 1 and 2, have been applied

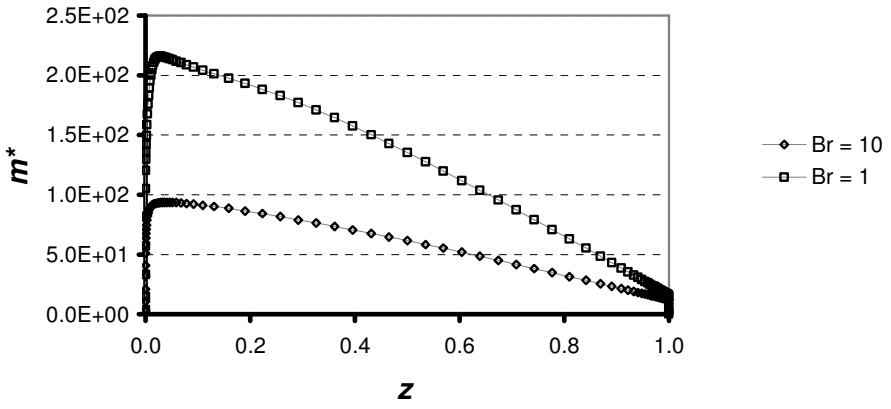

Figure 6.6: Axial distribution of the intrinsic flow strength m along the axial axis for high and low Brinkman numbers. The drive mechanism is Semi-IBC at the bottom and no drive at the top end cap.*

Calculated values for *m* are given in Fig. 6.6, they indicate a strongly decreasing internal flow. This decreasing internal flow can be explained by applying insights from the analytical models. The area between the inner Stewartson layer and the viscous core ($x_c \approx 2.6$) is the viscous region, Brouwers [3]. Analytical results show that in this area the stream function is expected to vary linearly along the *z* - axis between the values dictated by the Ekman layers at the top and bottom end cap. For the simulation considered, it should result in half of the bottom end cap values at mid plane since there is no Ekman suction condition at the top end cap. The results presented in Fig. 6.6 confirm this, they indicate a reduction of the flow strength approximately linear along the axial axis. The stream function will be analysed further in the next section.

6.1.4 Stream function

The change in profile of ψ is clearly visible by comparing Fig. 6.1 and 6.7. The profile resulting from the Ekman suction is reduced to a much narrower profile at *z* = 0.5, which obviously implies reduced E_f and *m* values as mentioned in the previous section. Because the gas is pushed from the viscous core towards the wall, a considerably higher peak in the stream function develops (for the *Br* = 1 case: $\approx 1.6\ 10^{-4}$ at *z* = 0.5 compared to $\approx 1\ 10^{-4}$ at the Ekman layer), compared to the values as predicted by the analytical theory.

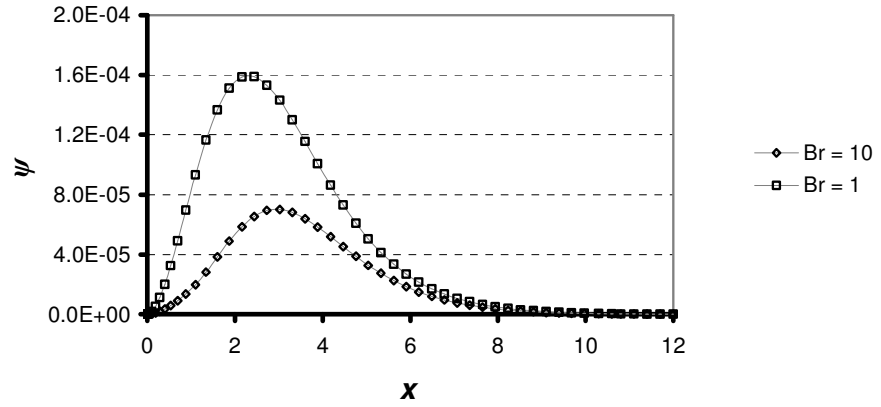

Figure 6.7: Radial distribution of the stream function ψ at z = 0.5, for a high and a low Brinkman number. A Semi-IBC drive mechanism is applied.

ψ peaks for *Br* = 1 roughly at the radial position where the core begins $x_c \sim 2.6$. For *Br* = 10 this peak appears at a somewhat higher *x* value. Results for ψ of the same simulations at *z* = 0.99 are given in Fig. 6.8.

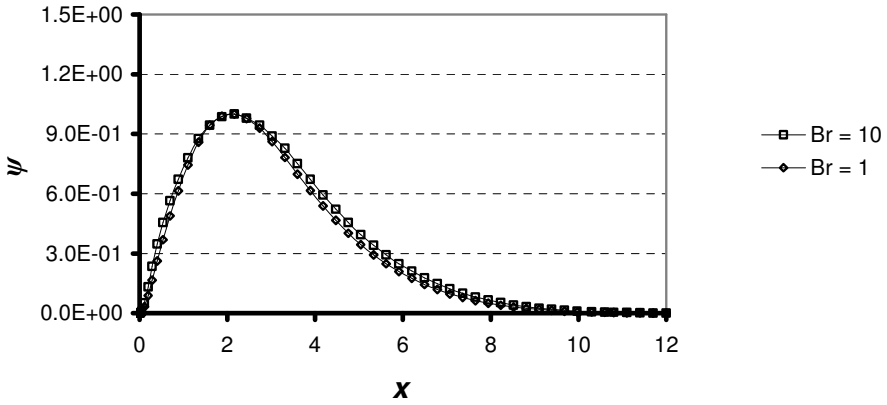

Figure 6.8: Radial distribution of the stream function ψ at z = 0.99, for a high and a low Brinkman number. A Semi-IBC drive mechanism is applied. The results are normalised to the same peak value, 1, to facilitate comparison of the shapes of the graphs.

Clearly, the peak for the high Brinkman case moved somewhat closer towards the wall if compared with Fig. 6.7.

The corresponding temperature profile at z = 0.01 is shown graphically in Fig. 6.9. From Fig. 6.9 it can be concluded that the temperature outside the Ekman layer is only a fraction higher in the low Brinkman case.

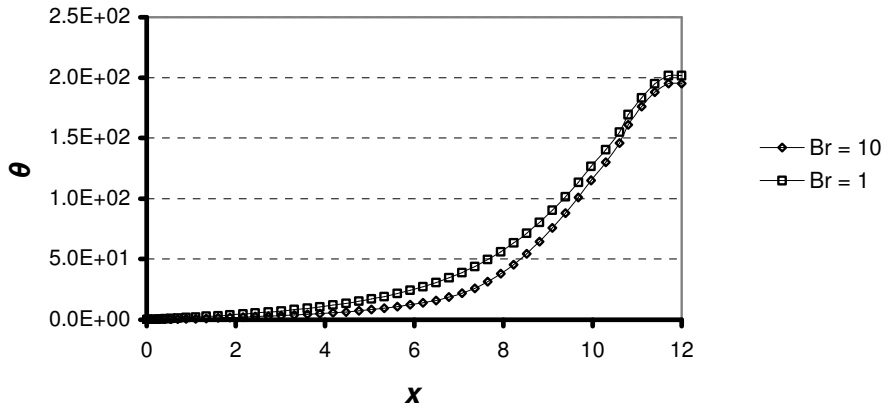

Figure 6.9: This figure Illustrates the difference in temperature profile in the Ekman bottom layer for high and low Brinkman numbers, Semi-IBC drive at the bottom end cap is applied.

6.2 Comparing mechanical and thermal drive

A series of calculations is reported applying a simple mechanical drive model (the bottom end cap rotating at a lower angular speed $\omega|_{z=0} = -1$) or a simple thermal drive model (the bottom end cap increased in temperature integrally to: $\theta|_{z=0} = +1$. The Brinkman number again is set at the values of 1 and 10, respectively, see Table 6.3.

Simulation	*A*	*E*	*L*	Br	Drive	E_f	*m**
[-]	[-]	[-]	[-]	[-]	[-]	[%]	[-]
1	16.8	$4.8\ 10^{-8}$	10	1	T	41.6	83
2	16.8	$4.8\ 10^{-8}$	10	1	M	42.2	160
3	16.8	$4.8\ 10^{-8}$	10	10	T	42.9	40
4	16.8	$4.8\ 10^{-8}$	10	10	M	43.3	78
5	16.8	$4.8\ 10^{-8}$	40	1	T	42.2	78
6	16.8	$4.8\ 10^{-8}$	40	1	M	42.6	153
7	16.8	$4.8\ 10^{-8}$	40	10	T	43.6	38
8	16.8	$4.8\ 10^{-8}$	40	10	M	43.6	75
9	16.8	$4.8\ 10^{-7}$	40	1	T	44.6	20
10	16.8	$4.8\ 10^{-7}$	40	1	M	44.9	39
11	16.8	$4.8\ 10^{-7}$	40	10	T	44.0	10
12	16.8	$4.8\ 10^{-7}$	40	10	M	44.2	20
13	67.2	$3.0\ 10^{-8}$	10	1	T	12.4	42
14	67.2	$3.0\ 10^{-8}$	10	1	M	12.5	81
15	67.2	$3.0\ 10^{-8}$	10	10	T	12.2	21
16	67.2	$3.0\ 10^{-8}$	10	10	M	12.3	41
17	67.2	$4.8\ 10^{-8}$	40	1	T	12.8	14
18	67.2	$4.8\ 10^{-8}$	40	1	M	12.8	26
19	67.2	$4.8\ 10^{-8}$	40	10	T	12.7	10
20	67.2	$4.8\ 10^{-8}$	40	10	M	12.7	20

Table 6.3: Parameter set defining Semi-long centrifuges. The data set is used to demonstrate the effect on E_f and m* *at high and low Brinkman numbers by applying mechanical (M) or thermal (T) drive mechanisms for the internal flow.*

The results as tabulated in Table 6.3 lead to the following conclusions:

- the mechanical drive results in approximately two times higher flow strength in all cases, compared to the results from the thermal drive, as predicted by analytical models
- the impact of the Brinkman number can be considered as a second order effect, leading to only a marginal impact if at all
- the mechanical drive results in a marginally higher efficiency in most cases.

6.3 Conclusions of the Br-effect in the Semi-long domain

The analytical Ekman suction relation adequately predicts the effect of the Brinkman number Br on the flow in the main compartment of the cylinder.

Diffusion effects limit the effectiveness of the Ekman layer close to the centreline. The effectiveness of the Ekman suction reduces systematically for $x > x_d - 2$, with x_d the analytically predicted values where diffusion dominates.

The impact of the Brinkman number Br on flow efficiency is shown to have a secondary effect in the Semi-long domain.

Chapter 7

Numerical results including a thermal model

Summary

In this chapter the numerical results of the combined fluid dynamic and thermal model as introduced in Chapters 3 and 4 will be presented and discussed. The main features of the presented model in this thesis, compared to previously published studies, are:

- the flexibility in applying a variety of boundary conditions
- simulation of the effects that thermal material properties have on the fluid dynamics.

The model is used in Chapter 5 to explain the gas dynamics when realistic, technically feasible boundary conditions for the fluid dynamics are applied. These features are combined in this chapter with those of the thermal model. It makes it possible to model centrifuges and study its performance for more realistic boundary conditions. The first three sections of this chapter are explanatory and provide the basis for undertaking this study. Section 7.4 deals with a pragmatic case:

In Section 7.1, the thermal model as boundary condition for the energy equation is explained. Results for three different materials (from a thermal conductivity point of view) are presented. These clearly show the effect of material properties on temperatures and internal flow.

In Section 7.2, a model centrifuge in the Semi-long domain is defined and the impact of the heat transfer from the end caps is varied from a pure insulation state to one with very high heat transfer coefficients. A mechanical drive at the bottom end cap is used to drive the internal flow.

Section 7.3, the same model centrifuge is used to simulate the effect of different material properties for the top end cap. Temperatures along the end cap and wall are presented.

In Section 7.4, a Semi-long domain centrifuge will be simulated. Materials with limited thermal conductivity for the end caps and the wall will be assumed as well as a limited but realistic heat transfer from the wall to the environment. A limited heat transfer from the wall can be desirable from an overall energy balance point of view. Depending on the wall pressure a high average temperature of the cylinder might be required preventing the gas from sublimating as discussed in Chapter 1. Limiting the loss of energy to the containing environment can be achieved by reducing the wall heat transfer coefficient. This reducing heat transfer coefficient affects in turn the fluid dynamics.

7.1 Evaluation of the thermal model

The thermal model for the wall and end caps is directly integrated into the mathematical model. This in turn is included into the resulting matrix containing the discrete version of all model equations. This means that a different energy equation for all grid points at x = 0, z = 0 and z = 1 (the wall and end cap locations) is required compared to the energy equation in the main compartment. The governing equation in the main compartment is a discrete version of the energy equation for the gas as derived in Appendix A.

The character of the boundary condition for the energy equation is the same for all three elements (top, bottom end caps and wall) and three terms are included in the equation:

- heat transfer from the gas to the element
- thermal conduction in the length of the element
- heat transfer by radiation to the containing environment.

For the wall, R = a, this results in the following equation:

$$-\lambda_g \left.\frac{\partial T_g}{\partial R}\right|_{R=a} + \lambda_w \delta_w \frac{\partial^2 T}{\partial Z^2} - h_w (T - T_w) = 0 \tag{7.1}$$

For the bottom end cap, Z = 0:

$$\lambda_g \left.\frac{\partial T_g}{\partial Z}\right|_{Z=0} + \lambda_b \delta_b \frac{1}{R}\frac{\partial}{\partial R}\left(R\frac{\partial T}{\partial R}\right) - h_b (T - T_b) = 0 \tag{7.2}$$

T_g is the gas temperature, λ_g, δ_w are respectively the thermal conductivity coefficient and thickness of the wall. h_w is the heat transfer coefficient by radiation between the wall and the environment. T_w is the temperature of the environment. The subscript b in eq. (7.2) refers to the same parameters of the end cap.

A similar equation holds for the top end cap, Z = 1.

Applying the definitions for the dimensionless radial coordinate x and axial coordinate z and dimensionless temperature θ, eq. (7.1) and (7.2) become:

$$-2A\frac{\lambda_g}{\lambda_w} L^2 \frac{a}{\delta_w} \left.\frac{\partial \theta_g}{\partial x}\right|_{x=0} + \frac{\partial^2 \theta}{\partial z^2} - \frac{h_w}{\lambda_w}\frac{L^2 a^2}{\delta_w}(\theta - \theta_w) = 0 \tag{7.3}$$

$$-\frac{\lambda_g}{\lambda_b}\frac{1}{L}\frac{a}{\delta_b} \left.\frac{\partial \theta_g}{\partial z}\right|_{z=0} + 4A^2 \frac{\partial}{\partial x}(1 - x/A)\frac{\partial \theta}{\partial x} - \frac{h_b}{\lambda_b}\frac{a^2}{\delta_b}(\theta - \theta_b) = 0 \tag{7.4}$$

The heat flux from the gas depends on the respective boundary layer thickness, at the end caps the Ekman layers and the outer Stewartson layer along the wall. The typical thickness of these layers follow from analytical theories as discussed in Chapter 2. At the wall, the outer Stewartson layer, this results in:

$$\left.\frac{\partial \theta_g}{\partial x}\right|_{x=0} \sim \frac{1}{AL^{1/2}E^{1/4}}$$

For the Ekman layer along the end caps:

$$\left.\frac{\partial \theta_g}{\partial z}\right|_{z=0} \sim \frac{L}{\sqrt{E}}$$

Application of these scaling rules results for the first term in eq. (7.3). and (7.4) in:

$$2\frac{\lambda_g}{\lambda_w}\frac{L^{3/2}}{E^{1/4}}\frac{a}{\delta_w} \tag{7.5}$$

$$\frac{\lambda_g}{\lambda_b}\frac{1}{E^{1/2}}\frac{a}{\delta_b} \tag{7.6}$$

Substituting $\lambda_g \sim O(10^{-2})$, $\lambda_w \sim O(10^2)$, $\lambda_b \sim O(10^2)$, $L \sim O(10^2)$, $a \sim O(10^{-1})$, $E \sim O(10^{-8})$ and $\delta_w \sim O(10^{-3})$ then eq. (7.5) indicates that the heat transfer of the gas to the wall is dominating over the axial conductivity. . Furthermore it indicates that at the cylinder wall the heat transfer by radiation dominates over the heat conductivity in the wall material at heat transfer coefficients > 1 W/m^2K. At the end caps, conductivity in the end cap material dominates the other terms in the equation.

7.2 Impact of the end cap heat transfer coefficient

In this section results are presented from simulations whereby the heat transfer coefficient by radiation for the top and bottom end cap to the environment, h, is varied from 1 to $10^5 W/m^2K$ in steps of a factor of 10.

A Semi-long centrifuge is modelled applying the parameter set given in Table 7.1.

A	*E*	*L*
67.2	$4.22\ 10^{-8}$	53.3

Table 7.1: Parameter set defining a Semi-long centrifuge. This data set is used to demonstrate the influence of thermal material properties of the end cap material on E_f and *m*.*

Wall and end cap thickness are set at 1 mm. The heat transfer coefficient by radiation from the wall to the environment is set at $5W/m^2K$ and the thermal conductivity at $20W/mK$, representing a Carbon fibre type of material. The material properties for the end caps are assumed to provide perfect insulation, thus diffusion is set to zero.

A mesh with 50 radial and 100 axial grid points is used. A simple mechanical drive is applied at the bottom end cap: $\omega = -1$.

Table 7.2 gives for varying heat transfer coefficients at the outer wall the flow efficiency E_f and intrinsic flow strength *m** as defined by eq. (A94):

h	E_f	*m**
$[W/m^2K]$	[%]	[-]
1	12.4	0.6
10	12.4	2.5
100	12.4	12
1000	12.4	27
10000	12.4	31

Table 7.2: Calculated values of E_f and *m* for different heat transfer coefficients between the end caps and the environment.*

The shape of the internal gas flow apparently does not change significantly, the amount of gas pumped around is decreasing with decreasing ability to exchange heat via the end cap. This results in cold gas at the bottom and hot gas at the top thereby contra acting to the mechanical drive mechanism.

7.3 Impact of the top end cap thermal conductivity

In this section results of three simulations are presented applying the parameter set as given in Table 7.3.

A	*E*	*L*	x_c
16.7	$3.4\ 10^{-8}$	273	5.5

Table 7.3: Parameter set defining a Semi-long centrifuge. The data set is used to demonstrate the influence of thermal material properties of the end cap material on E_f and *m.*

This parameter set represents the case of a Semi-long centrifuge. The thermal conductivity for the top end cap are varied from λ = 1 to 20 to 200 W/mK. This represents the full range of technical materials. The heat transfer by radiation from the wall to the environment is set at 1 W/m^2K, a wall thermal conductivity coefficient of 20 W/mK has been applied and a material thickness of 1 mm. The heat transfer from the top end cap to the environment is set at 20 W/m^2K. The drive at the bottom is represented by an Ideal Ekman thermal drive only.

In Fig. 7.1 the temperatures at the top end cap are given.

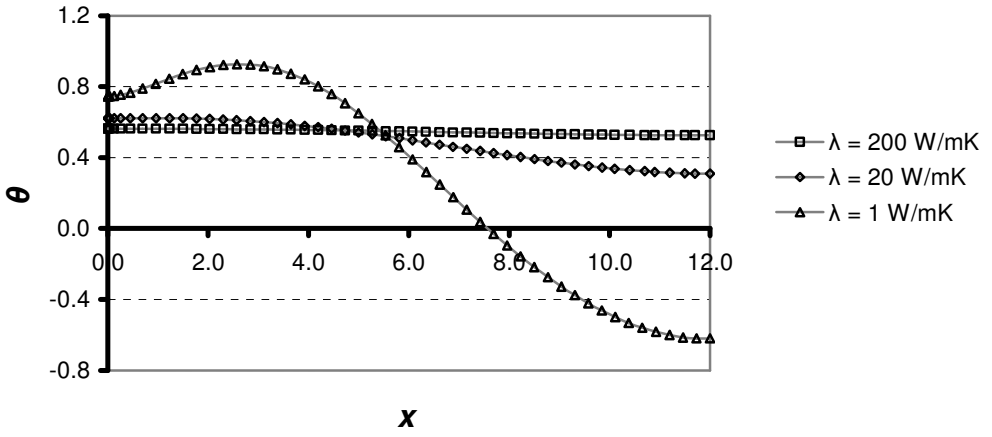

Figure 7.1: Top end cap temperatures for three different thermal conductivity coefficients. Semi-IBC drive is applied at the bottom end cap and a constant, one degree negative, temperature at the top end cap.

For these three simulations the flow efficiency and intrinsic flow strength are calculated and given in Table 7.4.

λ	E_f	m*
$[W/mK]$	[%]	[-]
1	70	269
20	71	285
200	71	290

Table 7.4: Calculated values of E_f and *m* for different end cap thermal conductivity coefficients.*

This strong flow strength is resulting from the exponential increase of the temperature along the *x* axis at the bottom end cap, induced by the ideal Ekman drive assumption.

The resulting wall temperatures for these simulations are presented in Fig. 7.2 and are virtually the same.

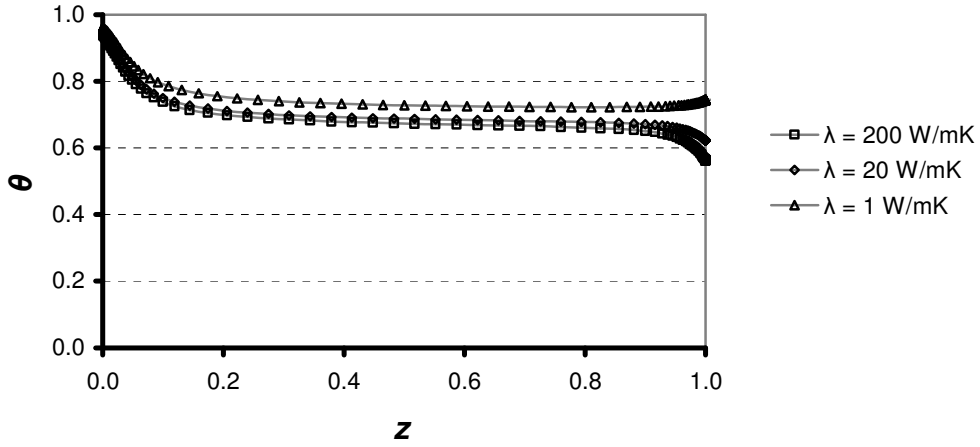

Figure 7.2: Axial distribution of the wall temperature for three different thermal conductivity coefficients, illustrating a small temperature gradient developing along the wall and steeper gradients near the bottom end cap.

The conclusion is that the material choice of the top end cap has minor impact on the flow in the main compartment.

7.4 Impact of the heat transfer between the wall to the environment

The same Semi-long centrifuge parameters as in the previous section will be used. In this section, the heat transfer coefficient between wall and environment, h, will be varied from very low to $10\,W/m^2K$ in steps of a factor of 10. The results are shown in Fig. 7.3 and 7.4. The top end cap and wall have thermal conductivity coefficients of $20\,W/mK$, thicknesses of 1 mm, ideal Ekman boundary conditions are assumed at the bottom. The wall temperature significantly decreases with increasing heat radiation as may be expected. The absolute temperature difference between Ekman boundary layers changes considerably as well.

In Table 7.5 the calculated flow efficiency and intrinsic flow strength are given.

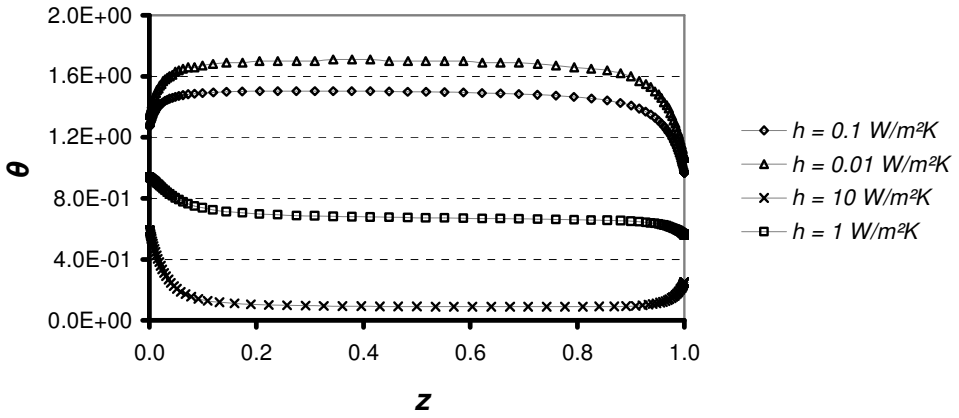

Figure 7.3: Axial distribution of the wall temperature, x = 0, by applying different heat transfer coefficients between wall and environment.

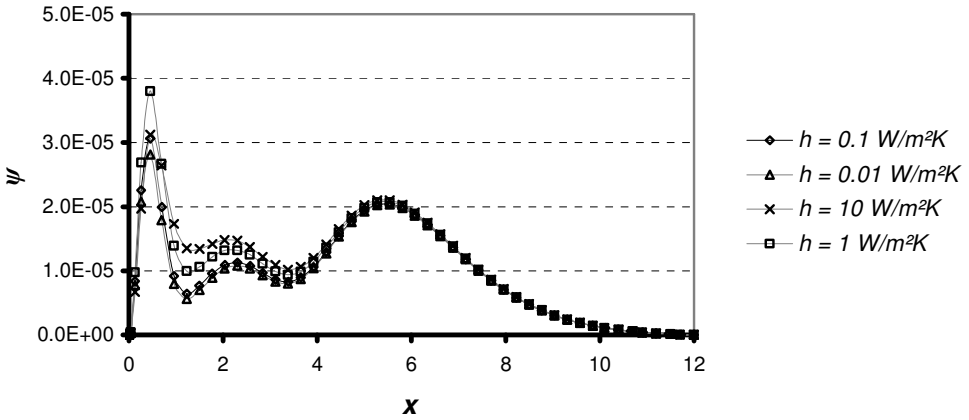

Figure 7.4: Radial distribution of ψ at z = 0.5, for different heat transfer coefficients between the wall and environment.

h	E_f	m*
$[W/m^2K]$	[%]	[-]
0.01	57	285
0.1	61	282
1	71	290
10	70	301

Table 7.5: Calculated values of E_f and m for different heat transfer coefficients between wall and environment.*

The results in Fig. 7.4 indicate that the overall radial shape of the internal gas flow is not significantly changing except close to the wall. An internal Stewartson circulation is observed depending on the temperature gradient developing in the wall material. Since the flow generated by a wall temperature gradient is considerably stronger compared to the flow generated by the end cap conditions, as shown in Chapter 4, an effect on the flow efficiency E_f may be expected and this is indeed observed.

When an Ideal Ekman condition is applied, this results in a high energy load at the bottom end cap. Therefore three simulations have been added. In these simulations an Ideal Ekman condition at the bottom end cap however the driving mechanism is reduced by not allowing the temperature (dimensionless) to exceed $\theta = 5$. The results are presented in Fig. 7.5.

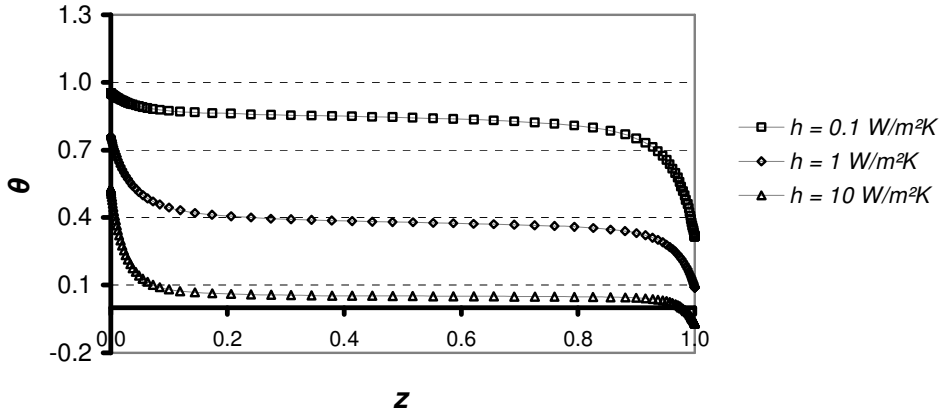

Figure 7.5: Axial distribution of the wall temperature, x = 0, for different heat transfer coefficients between wall and environment by applying a limited (cut off) Semi-IBC condition at the bottom end cap and a constant, one degree negative, temperature at the top end cap.

Clearly less energy is radiated by the wall, as can be seen from the lower temperature levels compared to Fig. 7.3. In Table 7.6 E_f and *m** are given for this simulation.

h	E_f	*m**
$[W/m^2K]$	[%]	[-]
0.1	48	220
1	50	232
10	55	218

Table 7.6: Calculated values of E_f and m for different heat transfer coefficients between wall and environment. A modified Ideal Ekman boundary condition is applied at the bottom end cap. The maximum temperature has been limited.*

A reduction of some 20 % in the flow efficiency is observed compared to IBC. Furthermore the disturbing effect of the increasing linear temperature gradient at decreasing heat transfer coefficients is clearly visible in these figures.

7.5 Conclusions on thermal model simulations

Summarising the simulations as presented in the previous sections, the following is observed and concluded for the Semi-long centrifuge under consideration:

- decreasing the end cap heat transfer coefficients and applying a constant wall to environment heat transfer coefficient results in a strongly reduced internal flow in the centrifuge
- the thermal conductivity coefficients of the end caps have a limited effect on the flow efficiency E_f and intrinsic flow strength *m**
- thermal properties of wall and end caps have limited effect on E_f
- increasing the heat losses from the wall to the environment by increasing the heat transfer coefficient has significant impact on E_f and a limited impact on *m*
- the main effect of the heat transfer coefficient between the wall and the containing environment results from the temperature gradient developing along the wall. Relatively small changes in temperature gradients in the wall results in strongly changing gas flows in the Stewartson layer and impacts E_f .

Discussion and conclusions

In the introduction of this thesis, available analytical and numerical models to predict the flow of a heavy gas in a rotating cylinder and subsequently the isotope separation performance have been reviewed and discussed. This review results in a number of questions and shortcomings of published approaches so far. Furthermore, in the first two chapters of this thesis the basic principles of a gas centrifuge, how to model the gas flow in realistic configurations is explained. A mathematical model is developed, the features explained and discussed. In chapters 5 to 7 this model is used to resolve observed issues in previous works.

The numerical model developed and applied in this thesis is based on the ψ-ζ formulation and results in four non-linearly coupled, partial differential equations of elliptic type. The advantage of this formulation is a reduction of the number of equations: four equations compared to six in the primary variables formulation. Stable and proven techniques are available to resolve sets of these elliptic equations. A dedicated software package has been developed and programmed in C++. This software package efficiently resolves the matrix equation and the resulting computer time on an average PC or laptop, anno 2009, applying a grid of 50 by 100 cells is about 15 seconds. There are some serious challenges in developing a numerical model for this physical problem: a first one is related to the Ekman layers and a second one is related to convergence problems in the ψ- ζ formulation. Both problems have been resolved in this study:

- the Ekman boundary layers are extremely thin, $\sim O(10^{-5})$ of the axial coordinate and these layers can increase up to two orders in thickness along the end caps of a gas centrifuge. It is a challenge for numerical models to make sure that sufficient resolution of these important boundary layers is achieved. In this thesis a transformation based on a series of exponential functions has been designed and applied. Five functions for the axial coordinate and two for the radial coordinate. These transformations prove to fit very well with this problem. The parameters used in this transformation are selected such that they can be calculated directly from analytical models, see Section 4.2

- a direct resolution of the matrix containing the discrete version of the model equation can be used up to numerical grids of approximately 50 radial and 100 axial cells. Applying larger grids then an iterative procedure has to be used to resolve the resulting matrix with discrete equations. From literature it is known that this set of equations creates convergence problems since the equation for vorticity is coupled to the equation for the stream function via the boundary values. This problem is fully eliminated by the developed iterative procedure specifically designed for this application as part of the research reported in this thesis. The iterative scheme is based on sweep wise solving all equations fully implicitly in adjacent strips. Each strip is overlapping with the previously calculated strip by at least one grid point. Per strip a number of cells in radial

direction and all cells in axial direction are included, the boundary conditions in radial direction are estimated values of the previously calculated strip or from the next to come strip. This method proves to intrinsically eliminate the mentioned instabilities caused by the coupling in boundary conditions, Section 4.5.

In Chapter 5 a numerical “pulse test” is successfully applied to prove the existence and position of a vertical boundary layer separating the viscous area and the core as predicted by analytical theories, see Brouwers [42]. The numerical model has been used to study the core position for two very different parameter sets, representing a Long and a Semi-long centrifuge. The results prove that the position of the core is virtually exactly as predicted by the analytical approach, Section 5.1. The numerical simulations furthermore show that the gas, directed by the Ekman layer into the core area, is flowing sideways into the viscous region in a pattern very close as approximated by Brouwers [42], applying a Pohlhausen approach. The flow efficiency factors, as predicted by this analytical model, approach the numerical results in this thesis for Ideal anti symmetrical Ekman boundary conditions closely. In the Long domain a difference is observed in the predicted value of the flow efficiency between the analytical model and the numerical simulations. The predictions from the analytical models in this domain are based on the lowest eigenfunction of the Onsager equation and they under value the flow efficiency factor of gas centrifuges systematically by some 10 to 15%, depending on the wall velocity, see Section 5.3.

Careful review of the calculated stream function in a centrifuge in the Short domain reveals an unexpected effect of the boundary conditions on the flow in the inviscid region. The flow in the inviscid region of a Short Gas centrifuge is not only determined by the Ekman layers as commonly assumed. Gas pumped by the local Ekman layers into the viscous and diffusive core region is pushed from these regions sideways into the inviscid region. This results in an almost linearly increasing stream function value along the axial axis. This is contrary to analytical theories which predicts a constant stream function along the axial axis, see Section 5.1.

The numerical model sheds clarity on the issue about the effect of “Less than ideal” boundary conditions as well. It shows that gas centrifuges in the Semi-long domain show high potential with respect to the flow efficiency factors by applying Ideal anti symmetrical Ekman conditions. They loose some of this potential under less ideal boundary values conditions. Several sets of boundary conditions are used to prove this point, see Sections 5.4 and 5.5.

The effect that the thermal properties of the wall and end caps have on the flow efficiency factor and flow strength has been studied. In three sets of simulations the thermal properties of the wall and end cap materials have been varied, the heat transfer coefficients between end cap and enclosure and lastly the heat transfer coefficient between the wall and enclosure. It proves that the material properties have a limited effect of the flow efficiency factors. The heat transfer coefficients between end caps and environment have a strong effect on the flow strength, it affects the flow efficiency less. Depending on the bottom boundary conditions, a temperature gradient

along the wall can develop which can adversely affect the flow efficiency, see Chapter 7.

The effect of the wall velocity on the flow efficiency and flow strength has been studied by varying the velocity parameter a factor of four (from $A \approx 16$ to $A \approx 65$). This results in a higher Brinkman number, which scales the production of heat and its diffusion, since this dimensionless number is linear with the velocity parameter. A parameter study shows that although the equations for energy and angular momentum loose their symmetry, thermal and mechanical drive are still interchangeable in the Semi-long domain up to wall velocities of at least 1000 m/s. The simulations prove that the correction for increasing values of the Brinkman number in the Ekman suction conditions is very accurate. While studying the effect of the Brinkman number, it became evident that the radial position where Ekman layers loose their specific character is well predicted by analytical theories. The numerical calculations show the radial diffusion effects to start at some lower values (about 2 increments) along the radial x axis, see Chapter 6.

During strategic studies, engineers like to have a simple tool to estimate quickly the effect that major design parameters have on performance. In this study, a new graphical representation for the flow efficiency is introduced. It enables to condense the results of parameter studies on the flow efficiency factor into a single graph, subject to the boundary conditions at the bottom end cap. The resulting graph is easy to use and can be expressed in a few simple equations, the scaled flow efficiency E_f^*, eq. (5.5), versus the corrected viscous core position x_{cc}, eq. (5.6):

$$E_f^* = 800 \ , \ x_{cc} < 4 \text{ and } E_f^* = 800 + \gamma(x_{cc} - 4), x_{cc} \geq 4$$

The parameter γ depends fully on the effectiveness of the driving mechanism for the internal flow, which is mainly determined by the boundary condition at the bottom end cap, see Chapter 5. The two extremes are:

- $\gamma = 100$, by applying Ideal Ekman suction conditions at the end caps
- $\gamma = -30$, by applying simple drive mechanisms like constant temperatures along the end caps.

The plateau level $E_f^* = 800$, as applied above is a pragmatic choice. The analytical limit for this plateau level of the Scaled flow efficiency E_f^* is 720, eq. (B.17), and is based on applying only the lowest eigenfunction solution. The numerical model obviously does not limit the solution to this lowest eigenfunction and predicts systematically a 10 to 15% higher level. A higher wall velocity results in a higher plateau level $E_f^* \sim 830$ at wall velocities of 1000 m/s, Section 5.3. This higher plateau level is due to the curvature term in the equation for E_f^*, eq. (5.5).

From a somewhat philosophical point of view it should be mentioned that the analytical approach in European literature in the 70-ties is fundamentally different from e.g. the North American approach: Boundary layer and flow region approach versus eigenfunctions. Gained insight as published by the European industry in the open literature clearly suggests to focus on Semi-long designs, see Brouwers [42]. It is not clear that the eigenfunction approach has lead to the same insight: possibly not, or much later in time. All indications are that the North American approach has been focusing on centrifuge development in the Long domain. This might be explained by the eigenfunction approach, this approach does not easily reveal the potential in terms of flow efficiency in the Semi-long domain. This is due to the inherently slowly converging solution and potentially misleading results. The boundary layer approach does indicate these potentially high flow efficiencies in this domain. The European design is currently being implemented in 2 out of 3 new separation plants in the USA, see [47].

Literature

[1] Los, J. & Wind, J. *Ultracentrifuges for the separation of a gas mixture in 2 components.* Patent CA 665505.

[2] Matsuda, T. 1975 Isotope separation by thermally driven countercurrent gas centrifuge. *J. Nucl. Sci. Tech*. **12,** 512 - 518.

[3] Brouwers, J.J.H. 1978 On compressible flow in a rotating cylinder. *J. Eng. Maths*. **12**, 265 - 285.

[4] Brouwers, J.J.H. 1976 *On the motion of a compressible fluid in a rotating cylinder*. Ph.D. thesis, Twente Univ. of Technology, Enschede, The Netherlands.

[5] Bark, F.H. & Bark, T.H. 1976 On vertical boundary layers in a rapidly rotating gas. *J. Fluid Mech*. **78**, 749 - 761.

[6] Cohen, K. 1951 *The theory of isotope separation as applied in large scale production of U235*. Mc Craw-Hill.

[7] Soubbaramayer. 1979 Centrifugation in uranium enrichment. *Topics in Appl. Phys. **35** (ed. S.* Villani).. Berlin, Springer Verlag. 183.

[8] von Halle, E. 1979 The optimum axial flow taper in a countercurrent gas centrifuge. *US Department of Energy, contract* W-7405 eng 26.

[9] Olander D. 1971 U.S. AEC Report UCRL-20506.

[10] Hirschfelder, J.O. 1960 *Molecular theory of gases and liquids*. John Wiley & Sons, New York

[11] Stewartson, K. 1957 On almost rigid rotations. *J. Fluid Mech*. **3**, 17 - 26.

[12] Stewartson, K. 1966 On almost rigid rotations, Part 2. *J. Fluid Mech*. **26**, 131 - 144.

[13] Bird, R.D., Stewart, W.E. and Lightfoot, E.N. 1960 *Transport phenomena*. John Wiley & Sons, New York.

[14] Nakayama, W. & Usui S. 1974 Flow in rotating cylinder of a gas centrifuge. *J. Nucl. Sci. Tech.* **11**, 242 - 262.

[15] Kai, T. 1983 Theoretical analysis of ternary UF_6 gas isotope separation by centrifuge. *J. Nucl. Sci. Tech.* **20**, 491 - 502.

[16] Matsuda, T., Tamura, N., Sawada, T. 1989 Three-dimensional numerical simulation of flows past scoops in a gas centrifuge. *J. Fluid. Mech*. **201**, 203 - 221.

[17] Dickinson, G.J. & Jones, I.P. 1981 Numerical solutions for the compressible flow in a rapidly rotating cylinder. *J. Fluid. Mech*. **107**, 89 - 107.

[18] Matsuda, T. & Hasimoto, K. 1976 Thermally, mechanically or externally driven flows in a gas centrifuge with insulated end plates. *J. Fluid. Mech.* **78**, 337 - 354.

[19] Pereira, L.M., Perez Geurrero, J.S., Brazao, N., Cotta, R.M. 2002 Compressible flow and heat transfer in ultracentrifuges: hybrid analysis via integral transforms. Int. J. Heat and Mass Transfer **45**, 99 - 112.

[20] Lopez, S. 1982 About the flow field in a mechanically driven ultracentrifuge for Uranium enrichment. *Meccanica* **19**, 15 - 24.

[21] Gunzburger, M.D. Wood, H.G., Jordan, J.A.. 1984 A finite element method for gas centrifuge flow problems. *SIAM Journal* **5**, 78 - 94.

[22] Wood, H.G. & Morton, J.P. 1980 Onsager's pancake approximation for the fluid dynamics of a gas centrifuge. *J. Fluid. Mech*. **101**, 1 - 31.

[23] Schroeder, W. & Hanel, D. 1985 *Multigrid solutions of the Navier-Stokes equations for the flow in rapidly rotating cylinders*. Proc. Ninth Conference on Numerical Methods in Fluid Dynamics, 487 - 491.

[24] Sakurai, T. & Matsuda, T. 1974 Gas dynamics of a centrifugal machine. *J. Fluid. Mech.* **62**, 727 - 736.

[25] Ying, C., Guo, Z., Wood, H.G. 1996 Solution of the diffusion equation in a gas centrifuge for separation of multi component mixtures. *Separation Science and Techn*. **31**, 2455 - 2471.

[26] Vicelli, J.A. 1993 Exponential difference operator approximating for the sixth order Onsager equation. J. Comput. Phys. **50**,162 - 170.

[27] Bourn, R., Peterson, T.E., Wood, H.G. 1999 Solution of the pancake model for flow in a gas centrifuge by means of a temperature potential. *Comp. Methods in Applied Mechanics and Engineering* **178**, 183 - 197.

[28] Migliavacca, S.C.P., Rodrigues, C., Nascimento, C.A.O. 2002 Analysis and optimisation of Gas centrifugal separation of uranium isotopes by neural networks. *Brazilian J. Chem. Eng*. **19**, 299 - 306.

[29] Makihara, H. & Ito, T. 1988 Separation characteristics of gas centrifuges. *J. Nucl. Sci. Tech*. **25**, 649 - 660.

[30] Parker, H.M. & Mayo, T.T. 1963 Counter-current flow in a semi-infinite gas centrifuge - Preliminary results. *Univ. of Virginia, Charlottesville, Rep.* E1-4422-279-630.

[31] Ging, J.L. 1962 Countercurrent flow in a semi-infinite gas centrifuge: axially symmetric solution in the limit of high angular velocity. *Univ. of Virginia, Charlottesville, Rep*. EP-4422-198-62S.

[32] Park, J.K. & Hyun, J.M. 1990 Numerical solutions for thermally driven compressible flows in a rapidly rotating cylinder. *Fluid Dyn. Res.* **6,** 139 - 153.

[33] Andrada, M.C.V. , Nascimento, C.A.O., Migliavacca, S.C.P. 2005 Detection of outliers in a gas centrifuge experimental data. *Brazilian J. Chem. Eng*. **22**, 389 - 400.

[34] Kai, T. & Hasegawa, K. 2000 Numerical calculation of flow and isotope separation for SF6 gas centrifuge. *J. Nucl. Sci. Tech*. **37**, 153 - 165.

[35] Harada, I. & Koyama, K. 1980 On the split of the compressible Stewartson layer due to a surface mounted obstacle. *J. Phys. Soc. Jpn*. **49**, 2425 - 2426.

[36] Los, J. 1963 *De scheiding van zware isotopen in een centrifugaal veld*. PhD thesis University Leiden, The Netherlands.

[37] Borisevich, V.D. & Yupatrov, S.V. 1990 Circulating rarefied gas flow in a rotating cylinder with a stationary upper end face. Mekhanika **3**, 492 - 494.

[38] Merten, A. & Hanel, D. 1982 *Navier Stokes Solution for compressible flows in a rotating cylinder.* Proc. of the Fourth Conf. on Num. Methods in Fluid Mechanics. 5. Vieweg-Verlag, Braunsweig.

[39] Tarbeyev., Yu et al. 1994. Scientific, engineering and metrological problems in producing pure Si and growing single crystals. *Metrologia* **31**, 269 - 273.

[40] USEC. 2009 United States Ultracentrifuge program. http://www.usec.com/

[41] Kalnay de Rivas, E. 1972 On the use of non-uniform grids in finite difference equations. *J. Comput. Phys.* **10**, 202 - 210.

[42] Brouwers, J.J.H. 1978 On compressible flow in a gas centrifuge and its effect on the maximum separative power. *Nuc. Tech*. **39**, 311 - 322

[43] Mol, C.A. 2002 Production of stable isotopes at Urenco: 10 years of progress*. Proc. 4th International Conference on Isotopes. Cape Town, South Africa*.

[44] Wood, H.G., Glaser, A. and Kemp, R.S. 2008 The gas centrifuge and nuclear weapon proliferation. www.physics today.com.

[45] Charles, D. 1992 Iraqi centrifuge mystery solved. *New Scientis* ***1847***, 8.

[46] Dewitt, R. 1960 *Uranium Hexafluoride: A survey of the physico-chemical properties.* Report 280, Goodyear Atomic Corporation.

[47] Zuidema, T. 2009 Nieuwe verrijkingsinstallaties in VS. *Technisch Weekblad* Maart 2009, 4.

[48] Steenbeck, M. 1958 Erzeugung einer selbstkaskadierenden Axialströmung in einer langen Ultrazentrifuge zur Isotopentrennung. *Kernenergie* **1**, 921 - 928.

[49] Greenspan, H.P. 1968 *The theory of rotating fluids*. Cambridge University Press.

Appendix A

Mathematical formulation

Introduction

In this appendix, a mathematical model will be developed to describe the axisymmetrical flow and temperature distribution in a gas centrifuge as discussed in Chapter 1.

It is assumed that the fluid has constant material properties such as

- the dynamic viscosity, thermal diffusion and the specific heat at constant pressure C_p are constant and e.g. not depending on temperature
- the gas behaves according to the ideal gas equation of state.

The mathematical model is based on the following equations, here for simplicity given in vector notation, Bird [13]:

Navier Stokes

$$\rho\left(\frac{\partial \underline{v}}{\partial t}+\underline{v}.\nabla\underline{v}\right)=-\nabla P+\mu\nabla^2\underline{v}+f+(\ \mu/3+\mu^V\ )\nabla(\nabla.\underline{v}) \tag{A1}$$

continuity equation

$$\frac{\partial(\rho)}{\partial t}+\nabla.(\rho\underline{v})=0 \tag{A2}$$

energy equation

$$\rho C_p\left(\frac{\partial T}{\partial t}+\underline{v}.\nabla T\right)=-\frac{T}{\rho}\left(\frac{\partial\rho}{\partial T}\right)_p\underline{v}.\nabla P+\lambda\nabla^2T+\Phi \tag{A3}$$

equation of state for an ideal gas

$$P=\rho\frac{R_0T}{M} \tag{A4}$$

The equations are defined in a fixed coordinate system, $\underline{v}$ is the absolute velocity, P,T the absolute pressure and temperature, respectively. R_0, M are the general gas constant and molecular mass. ρ is the density and f is a body force (e.g. the gravitational force).

An ideal gas will be considered, this allows removal of the bulk viscosity and to simplify the energy equation since:

$$-\frac{T}{\rho}\left(\frac{\partial \rho}{\partial T}\right)_p = 1 \tag{A5}$$

for such a gas. Body forces are extremely small compared to the rotational forces in this application and are neglected as well. For steady flow, the set of equations is rewritten and applying the assumptions mentioned:

$$\rho(\underline{v}.\nabla)\underline{v} = -\nabla P + \mu(\nabla^2 \underline{v} + \frac{1}{3}\nabla(\nabla.\underline{v})) \tag{A6}$$

continuity equation

$$\nabla.(\rho \underline{v}) = 0 \tag{A7}$$

energy equation

$$\rho C_p(\underline{v}.\nabla T) = \underline{v}.P + \lambda \nabla^2 T + \Phi \tag{A8}$$

In Section A1 the equations will be transformed to dimensionless form. In sections A2 to A7 first order linear approximations for this set of equations will be derived for the individual components of the Navier-Stokes equation and for the temperature. Subsequently a model in stream function and vorticity will be derived.

A1 Dimensionless equations

In this section two strategies to further analyse the above presented equations are discussed:

- a first strategy is based on non-dimensionalising the equations in a fixed coordinate system
- a second strategy is based on non-dimensionalising the equations in a rotating framework.

Following this non-dimensionlisation, linearization of the resulting set of equations has to be carried out applying a perturbation method. Depending on the chosen strategy, an appropriate set of perturbations for the variables has to be defined. This is the subject of Section A2 through A7.

A1.1 Dimensionless Navier-Stokes equations in a fixed framework

The momentum equation as given in eq. (A1) is:

$$\rho(\underline{v}.\nabla)\underline{v} = -\nabla P + \mu(\nabla^2 \underline{v} + \frac{1}{3}\nabla(\nabla.\underline{v})) \tag{A9}$$

This equation is non-dimensionilsed by introducing the following dimensionless variables:

$$\underline{v}^* = \frac{\underline{v}}{v_w}, \rho^* = \frac{\rho}{\rho_w}, T^* = \frac{T}{T_0}, P_t^* = \frac{P}{\rho_w v_w^2} \tag{A10}$$

and a dimensionless length scale

$$r = \frac{R}{a}, \; z = \frac{Z}{l} \tag{A11}$$

here

$$v_w = \Omega a$$

is the wall velocity and ρ_w is the density at the wall, a is the radius of the cylinder, Ω is the angular velocity of the rotating cylinder. Furthermore the following dimensionless length ratio will be used:

$$L = \frac{l}{a} \tag{A12}$$

L will be referred to as the aspect ratio of the cylinder and ρ_w is the density at the wall.

Incorporating these variables in eq. (A1), the Navier-Stokes equation takes the following form:

$$\rho^* \left(\underline{v}^* . \nabla^* \right) \underline{v}^* = -\nabla^* P_t^* + \frac{1}{Re} (\nabla^{*2} \underline{v}^* + \frac{1}{3} \nabla^* (\nabla^* . \underline{v}^*)) \tag{A13}$$

where

$$Re = \frac{\rho_w a v_w}{\mu} \tag{A14}$$

is the Reynolds number. This non-dimensional number represents the ratio of non-linear advection and viscous terms:

$$Re = \frac{[\rho(\underline{v}.\nabla)\underline{v}]}{[\mu(\nabla^2 \underline{v} + \frac{1}{3}\nabla(\nabla.\underline{v}))]} = \frac{\rho_w a v_w}{\mu} \tag{A15}$$

A1.2 Dimensionless Navier-Stokes equations in a rotating framework

In view of the overall rotation of the system, it may be preferable to describe the flow in terms of a relative velocity $\underline{v}$ with respect to a co-rotating coordinate system. Such a description implies additional terms in the equation of motion, namely those associated with the Coriolis acceleration and the centrifugal acceleration.

The Navier-Stokes equation for the relative motion in a steady state is:

$$\rho(\underline{v}.\nabla)\underline{v} + 2\rho\underline{\Omega}\times\underline{v} - \rho\underline{\Omega}\times\underline{\Omega}\times\underline{r} = -\nabla P + \mu(\nabla^2\underline{v} + \frac{1}{3}\nabla(\nabla.\underline{v})) \tag{A16}$$

with $2\rho\underline{\Omega}\times\underline{v}$ the Coriolis term and $\rho\underline{\Omega}\times\underline{\Omega}\times\underline{r}$ representing the centrifugal forces acting on the fluid. The gravitational force can be presented as a potential force, the resulting equation then reads like:

$$\rho(\underline{v}.\nabla)\underline{v} + 2\rho\underline{\Omega}\times\underline{v} - \rho\nabla(\frac{1}{2}\Omega^2 r^2) = -\nabla P + \mu(\nabla^2\underline{v} + \frac{1}{3}\nabla(\nabla.\underline{v})) \tag{A17}$$

Here a “reduced pressure” is defined as

$$\nabla P_r = \nabla P - \rho\nabla(\frac{1}{2}\Omega^2 r^2) \tag{A18}$$

a result that can be used to simplify eq. (A17)

$$\rho(\underline{v}.\nabla)\underline{v} + 2\rho\underline{\Omega}\times\underline{v} = -\nabla P_r + \mu(\nabla^2\underline{v} + \frac{1}{3}\nabla(\nabla.\underline{v})) \tag{A19}$$

To non-dimensionalize this equation, the non-dimensional variables as defined in eqs. (A10) - (A12) are applied with exception for the velocity and pressure, these are defined as:

$$\underline{v}^* = \frac{\underline{v}}{U} \text{ and } P^* = \frac{P_r}{\rho_w \Omega a U} \tag{A20}$$

with U a small typical velocity in the rotating fluid, not being the velocity of the rotating frame work and $\begin{bmatrix} v_r^* \\ v_\theta^* \\ v_z^* \end{bmatrix}$ are the components of $\underline{v}^*$.

The equation of motion now becomes:

$$\varepsilon\rho^*(\underline{v}^*.\nabla^*)\underline{v}^* + 2\rho^*\underline{k}\times\underline{v}^* = -\nabla^* P^* + E(\nabla^2\underline{v}^* + \frac{1}{3}\nabla^*(\nabla^*.\underline{v}^*)) \tag{A21}$$

with $\underline{k} = \frac{\underline{\Omega}}{|\underline{\Omega}|}$ is the unit vector in axial direction. Furthermore:

- $\varepsilon = \frac{U}{\Omega a}$ is the Rossby number

- $E = \dfrac{\upsilon}{\Omega a^2}$ the Ekman number with $\upsilon = \dfrac{\mu}{\rho_w}$.

The Rossby number is a measure of the ratio of Coriolis and inertial forces in eq. (A21) since:

$$\varepsilon = \frac{\left[(\underline{v}.\nabla)\underline{v}\right]}{\left[\underline{\Omega}\times\underline{v}\right]} = \frac{U^2/a}{\Omega U} = \frac{U}{\Omega a} \tag{A22}$$

whereas the Ekman number describes the relative importance of viscous forces relative to the Coriolis forces:

$$E = \frac{\left[\upsilon\nabla^2\underline{v}\right]}{\left[\underline{\Omega}\times\underline{v}\right]} = \frac{\upsilon U/a^2}{\Omega U} = \frac{\upsilon}{\Omega a^2} \tag{A23}$$

In this study ε is determined by the driving mechanism of the internal flow; e.g.: if the flow is driven by an end cap rotating at a somewhat different angular velocity compared to the cylinder wall i.e. at an angular velocity of $\Omega + \Delta\Omega$ or has a temperature $T_0 + \Delta T$, then ε follows from:

$$\varepsilon = \frac{\Delta\Omega}{\Omega} \text{ or } \varepsilon = \frac{\Delta T}{T_0} \tag{A24}$$

Obviously both driving mechanisms can be combined and ε should be calculated accordingly.

Alternatively a temperature gradient along the wall can be applied, resulting in the same definition of ε.

Applying the definitions of $\underline{v}^*$ and $\underline{k}$, then the Coriolis force in eq. (A21) appears to results in two components:

$$\underline{k}\times\underline{v}^* = \begin{bmatrix}0\\0\\1\end{bmatrix}\times\begin{bmatrix}v_r^*\\v_\theta^*\\v_z^*\end{bmatrix} = \begin{bmatrix}-v_\theta^*\\v_r^*\\0\end{bmatrix} \tag{A25}$$

and the centrifugal forces acting on the fluid in the radial direction:

$$\nabla\left(\frac{1}{2}\Omega^2 r^2\right) = \Omega^2 a\nabla^*\left(\frac{1}{2}r^2\right) = \Omega^2 a\begin{bmatrix}r\\0\\0\end{bmatrix} \tag{A26}$$

Assuming a very small Rossby number, $\varepsilon << 1$, eq. (A21) can be simplified by neglecting the inertial forces which results in:

$$2\rho^* \underline{k} \times \underline{v}^* = -\nabla^* P^* + E(\nabla^2 \underline{v}^* + \frac{1}{3}\nabla^*(\nabla^* . \underline{v}^*)) \tag{A27}$$

This equation is the basis for the linearization as will be executed in the next sections

A1.3 Calculation of the iso-thermal rigid body rotation

A radial pressure gradient present in static equilibrium ($\underline{v} = 0$) can be calculated from eq. (A.18) by:

$$-\rho_s \nabla(\frac{1}{2}\Omega^2 r^2) = -\nabla P_s \tag{A28}$$

with P_s, ρ_s the pressure and density in static equilibrium.

Substituting the ideal gas relation and the definition for the density and wall velocity yields:

$$P_s \frac{M}{R_0 T_0} v_w^2 r = \frac{\partial P_s}{\partial r} \tag{A29}$$

Integration of this equation and by applying the boundary condition: $P_s(r=1) = P_w$ respectively $\rho_s(r=1) = \rho_w$ results:

$$P_s(r) = P_w e^{-x} \text{ and } \rho_s(r) = \rho_w e^{-x} \tag{A30}$$

In this equation x is defined as a new radial coordinate:

$$x = A(1 - r^2) \tag{A31}$$

and

$$A = \frac{1}{2}\frac{M v_w^2}{R_0 T_0} \tag{A32}$$

The coordinate *x* fits the physics of the problem better than the radial coordinate *r*, which is just a geometrical dimension. By applying *x,* all equations can be scaled relative to the exponential pressure decrease.

Eqs. (A30) are the pressure and density distribution in iso-thermal rigid rotation. In dimensionless form these are defined as:

$$\overline{P}(r) = e^{-x} \text{ and } \overline{\rho}(r) = e^{-x} \tag{A33}$$

A2 Defining Perturbations

The linearization of the equations, as defined in the Section A1, will be based on the perturbation method. The approach is valid as long as the perturbations are small variations of the individual variables around a chosen main flow. For a gas centrifuge, the main flow is chosen to be the isothermal rigid body rotation of an ideal gas and $\varepsilon << 1$ as defined in section A1.

The following definitions for the perturbations will be used:

$$\begin{aligned} P &= P_s (1 + \varepsilon P^{**}) \\ \rho &= \rho_s (1 + \varepsilon \rho^{**}) \\ T &= T_0 (1 + \varepsilon \theta) \end{aligned} \tag{A34}$$

and the components of $\underline{v}^*$ are:

$$\begin{aligned} v_r^* &= u(r,z) \\ v_\theta^* &= r\omega(r,z) \\ v_z^* &= w(r,z) \end{aligned} \tag{A35}$$

In eqs. (A34) $P^{**}, \rho^{**}, \theta$ are the perturbations. P_s, ρ_s and T_0 are the pressure, density and temperature of an ideal gas in a rigid body rotation. The perturbations are used to determine the reduced pressure by substituting them in eq. (A18) and applying eq. (A20):

$$\frac{\partial P^*}{\partial r} = \frac{P_w}{\rho_w \Omega^2 a^2} \frac{\partial (e^{-x} P^{**})}{\partial r} - e^{-x} \rho^{**} r \,. \tag{A36}$$

By defining :

$$\frac{\partial P_r^{**}}{\partial r} = \frac{P_w}{\rho_w \Omega^2 a^2} \frac{\partial (e^{-x} P^{**})}{\partial r}$$

eq. (A36) can be presented as:

$$\frac{\partial P^*}{\partial r} = \frac{\partial P_r^{**}}{\partial r} - e^{-x} \rho^{**} r \tag{A37}$$

This density variation in the right hand side of eq. (A37) can be expressed in temperature variations by applying the equation of state for an ideal gas:

$$\left.\frac{\partial \rho}{\partial T}\right|_P = -P\frac{M}{R_0 T^2} \tag{A38}$$

By applying the perturbation definitions eq. (A34), eq. (A38) can be represented as:

$$\left.\rho_s \rho^{**}\right|_P = -P_s \frac{M}{R_o T_0}\theta \tag{A39}$$

Substituting the ideal gas relation to eliminate ρ_s reveals:

$$\left.\rho^{**}\right|_P = -\theta \tag{A40}$$

Applying eq. (A40) is a simplification since the pressure effect on the density is neglected. This simplification is firstly applied by Onsager in the 1950's and later by Steenbeck [48], Brouwers [4], Schroeder & Hanel [23] and others. This simplification is applied to separate the ideal gas equation fully from the linearised conservation equations. This simplification is not included in the works of Dickingson and Jones [17] and Merten & Hanel [38]. The later article confirms explicitly that this simplification has no major consequences on the results, ref. Schroeder & Hanel [23]. Intuitively the simplification likely will result in overstating the effectiveness of mechanical and or thermal drive of the internal flow since the pressure effect on the density will counteract these effects somewhat. This would mean that in a practical situation a somewhat higher temperature difference between the end caps would be needed to drive the flow sufficiently as compared to the calculated one. Quantitatively it is expected that it will be a very small effect.

Subsequently eq. (A37) results in:

$$\frac{\partial P^*}{\partial r} = \frac{\partial P_r^{**}}{\partial r} + e^{-x}\theta r \tag{A41}$$

This is the radial component of $\nabla^* P^*$ in eq. (A27).

A3 Linearization of the radial component of the Navier-Stokes equation

The radial component of the momentum equation can be derived from eq. (A27) and eq. (A35) as:

$$-2r\omega\rho^* = -\frac{\partial P^*}{\partial r} + E\left[\frac{\partial}{\partial r}\left(\frac{1}{r}\frac{\partial ru}{\partial r}\right) + \frac{1}{L^2}\frac{\partial^2 u}{\partial z^2} + \frac{1}{3}\frac{\partial}{\partial r}\left(\nabla^* . \underline{v}^*\right)\right] \tag{A42}$$

Substitution of eq. (A33) and eq. (A41), results in the $O(\varepsilon)$ equation for the radial velocity:

$$-2\bar{\rho}\omega r + e^{-x}\theta r = -\frac{\partial(P_r^{**})}{\partial r} + E\left[\frac{\partial}{\partial r}\left(\frac{1}{r}\frac{\partial ru}{\partial r}\right) + \frac{1}{L^2}\frac{\partial^2 u}{\partial z^2} + \frac{1}{3}\frac{\partial}{\partial r}\left(\nabla^* . \underline{v}^*\right)\right] \tag{A43}$$

or

$$r(\theta - 2\omega)e^{-x} = -\frac{\partial(P_r^{**})}{\partial r} + E\left[\frac{\partial}{\partial r}\left(\frac{1}{r}\frac{\partial ru}{\partial r}\right) + \frac{1}{L^2}\frac{\partial^2 u}{\partial z^2} + \frac{1}{3}\frac{\partial}{\partial r}\left(\nabla^* . \underline{v}^*\right)\right] \tag{A44}$$

with

$$\nabla^* . \underline{v}^* = \left[\frac{1}{r}\frac{\partial ru}{\partial r} + \frac{1}{L}\frac{\partial w}{\partial z}\right] \tag{A45}$$

Coriolis and centrifugal forces are balanced by a radial pressure gradient and viscous diffusion of the radial velocity.

A4 Linearization of the azimuthal component of the Navier-Stokes equation

The azimuthal component of the momentum equation can be derived from eq. (A27) as:

$$2\rho^* u = E\left[\frac{\partial}{\partial r}\left(\frac{1}{r}\frac{\partial r^2\omega}{\partial r}\right) + \frac{1}{L^2}\frac{\partial^2 r\omega}{\partial z^2}\right] \tag{A46}$$

Applying the perturbations as defined in eq. (A34) in the left hand side term of eq. (A46) and neglecting the $O(\varepsilon^2)$ term, results in:

$$\frac{2ue^{-x}}{r} = E\left[\frac{1}{r}\frac{\partial}{\partial r}\left(\frac{1}{r}\frac{\partial r^2\omega}{\partial r}\right) + \frac{1}{L^2}\frac{\partial^2\omega}{\partial z^2}\right] \tag{A47}$$

The left hand side is a term resulting from the Coriolis force, balanced by viscous diffusion of angular velocity.

A5 Linearization of the axial component of the Navier-Stokes equation

The axial component of the momentum equation can be derived from eq. (A27) and eq. (A35) as:

$$0 = -\frac{1}{L}\frac{\partial P^*}{\partial z} + E\left[\frac{\partial}{\partial r}\left(\frac{1}{r}\frac{\partial rw}{\partial r}\right) + \frac{1}{L^2}\frac{\partial^2 w}{\partial z^2} + \frac{1}{3L}\frac{\partial}{\partial z}\left(\nabla^* . \underline{v}^*\right)\right] \tag{A48}$$

Substituting the perturbations eq. (A34) for the pressure results in:

$$0 = -\frac{1}{L}\frac{\partial(P_r^{**})}{\partial z} + E\left[\frac{\partial}{\partial r}\left(\frac{1}{r}\frac{\partial rw}{\partial r}\right) + \frac{1}{L^2}\frac{\partial^2 w}{\partial z^2} + \frac{1}{3L}\frac{\partial}{\partial z}\left(\nabla^* . \underline{v}^*\right)\right] \tag{A49}$$

with

$$\nabla^* . \underline{v}^* = \left[\frac{1}{r}\frac{\partial ru}{\partial r} + \frac{1}{L}\frac{\partial w}{\partial z}\right] \tag{A50}$$

A6 Non-dimensionalising and linearization of the energy equation

The energy equation as given in the introduction of this appendix, eq. (A8) is:

$$\rho C_p\left(\underline{v}.\nabla T\right) = \underline{v}.\nabla P + \lambda\nabla^2 T + \Phi \tag{A51}$$

In this equation Φ represents an internal (in the gas) heat source due to dissipation and is of the order:

$$\Phi \sim \mu(\nabla \underline{v})^2 . \tag{A52}$$

Applying the dimensionless variables as defined in eqs. (A10) - A(12) and eq. (A20), then this equation can be written as:

$$\varepsilon a\rho_w C_p v_w T_0 \rho^*\left(\underline{v}^* . \nabla^* T^*\right) = \varepsilon a v_w^3 \rho_w \underline{v}^* . \nabla^* P_t^* + \lambda T_0 \nabla^{*2} T^* + \varepsilon^2 \mu v_w^2 \Phi^* \tag{A53}$$

with

$$\Phi^* \approx (\nabla^* \underline{v}^*)^2 \tag{A54}$$

Rearranging terms in eq. (A53) results in:

$$\varepsilon \frac{Pr}{E}\rho^*\left(\underline{v}^* . \nabla^* T^*\right) = \varepsilon \frac{Br}{E}\underline{v}^* . \nabla^* P_t^* + \nabla^{*2} T^* + \varepsilon^2 Br\Phi^* \tag{A55}$$

where

$$Br = \frac{\mu v_w^2}{\lambda T_0} \text{ and } Pr = \frac{\mu C_p}{\lambda} \tag{A56}$$

Br is the Brinkman number, *E* is the Ekman number as defined in eq. (A23). *Br* is a non-dimensional number representing the ratio of heat production and diffusion terms:

$$Br = \frac{[\Phi]}{[\lambda \nabla^2 T]} = \frac{\mu v_w^2}{\lambda T_0} \tag{A57}$$

Pr is the Prandtl number, for most gasses $Pr \approx 1$. In this study it is assumed that *Br* can reach values up to ≈ 10.

Applying eq. (A33) and the perturbations as defined in eqs. (A34) then eq. (A55) results in:

$$\varepsilon^2 \frac{Pr}{E} \rho^* \left(\underline{v}^* . \nabla^* \theta \right) = \varepsilon \frac{Br}{E} \underline{v}^* . \nabla \frac{P_s}{\rho_w v_w^2} (1 + \varepsilon P^{**}) + \varepsilon \nabla^{*2} \theta + \varepsilon^2 Br \Phi^* \tag{A58}$$

discarding $O(\varepsilon^2)$ terms results in:

$$-Bre^{-x} ur = E \left[\frac{1}{r} \frac{\partial}{\partial r} \left(r \frac{\partial \theta}{\partial r} \right) + \frac{1}{L^2} \frac{\partial^2 \theta}{\partial z^2} \right] \tag{A59}$$

The left hand side is the work done in compression and the right hand side is the diffusion of heat.

A7 Linearization of the continuity equation

The continuity equation as presented earlier as eq. (A2) is:

$$\frac{\partial(\rho)}{\partial t} + \nabla . (\rho \underline{v}) = 0 \tag{A60}$$

By applying eqs. (A10) - (A12), A(20) and A(35), the following equation in cylindrical coordinates results for the steady, axisymmetrical state:

$$\frac{1}{r} \frac{\partial}{\partial r} \left(r \rho^* u \right) + \frac{1}{L} \frac{\partial}{\partial z} \left(\rho^* w \right) = 0 \tag{A61}$$

Subsequently substitution of the perturbations eqs. (A34) results in:

$$\frac{1}{r} \frac{\partial}{\partial r} \left(r(\rho_s (1 + \varepsilon \rho^{**})) u \right) + \frac{1}{L} \frac{\partial}{\partial z} \left((\rho_s (1 + \varepsilon \rho^{**})) w \right) = 0 \tag{A62}$$

Dropping terms $O(\varepsilon^2)$ and applying eq. (A33) yields the $O(\varepsilon)$ equation for continuity:

$$\frac{e^x}{r}\frac{\partial(re^{-x}u)}{\partial r}+\frac{1}{L}\frac{\partial w}{\partial z}=0 \tag{A63}$$

A8 A stream function and vorticity model

The stream function – vorticity model is based on the $O(\varepsilon)$ equations for the radial and axial velocities as derived in the previous sections:

$$r(\theta-2\omega)e^{-x}=-\frac{\partial(P_r^{**})}{\partial r}+E\left\{\frac{\partial}{\partial r}\left[\frac{1}{r}\frac{\partial ru}{\partial r}\right]+\frac{\partial^2 u}{L^2\partial z^2}+\frac{1}{3}\frac{\partial}{\partial r}(\nabla^*.\underline{v}^*)\right\} \tag{A64}$$

$$0=-\frac{1}{L}\frac{\partial(P_r^{**})}{\partial z}+E\left\{\frac{1}{r}\frac{\partial}{\partial r}\left[r\frac{\partial w}{\partial r}\right]+\frac{1}{L^2}\frac{\partial^2 w}{\partial z^2}+\frac{1}{3L}\frac{\partial}{\partial z}(\nabla^*.\underline{v}^*)\right\} \tag{A65}$$

The vorticity is defined as $\underline{\xi}=\nabla\times\underline{v}$. In a two-dimensional situation, only ξ_ϕ, the axisymmetrical component is non-zero. From here "*vorticity*" is defined as ξ_ϕ and will be written as ξ. This vorticity ξ follows from:

$$\xi=\frac{\partial U}{\partial Z}-\frac{\partial W}{\partial R} \tag{A66}$$

with *U* and *W* are the absolute velocities and *Z*, *R* the dimensional coordinates.

Applying dimensionless coordinates and the perturbation for the velocities, results in the equation for the dimensionless vorticity ζ:

$$-\xi\frac{a}{v_w}=\zeta r=\frac{\partial w}{\partial r}-\frac{1}{L}\frac{\partial u}{\partial z} \tag{A67}$$

Differentiating eq. (A64) to *z* and (A65) to *r*, subtracting them and applying eq. (A67), results in:

$$\frac{1}{L}\frac{\partial}{\partial z}(2\omega-\theta)e^{-x}=E\left[\frac{1}{r}\frac{\partial}{\partial r}\left(\frac{1}{r}\frac{\partial r^2\zeta}{\partial r}\right)+\frac{1}{L^2}\frac{\partial^2\zeta}{\partial z^2}\right] \tag{A68}$$

In order to define a stream function, the continuity eq. (A63) is used:

$$\frac{1}{e^{-x}r}\frac{\partial(re^{-x}u)}{\partial r}+\frac{1}{L}\frac{\partial w}{\partial z}=0 \tag{A69}$$

Based of this equation, the dimensionless stream function ψ for an axisymmetrical two-dimensional situation is as:

$$\frac{1}{L}\frac{\partial \psi}{\partial z} = -e^{-x} ur \quad \text{and} \quad \frac{\partial \psi}{\partial r} = wre^{-x} \tag{A70}$$

Substitution of eq. (A70) in the definition for the vorticity eq. (A67) results in:

$$\zeta r = \frac{\partial w}{\partial r} - \frac{1}{L}\frac{\partial u}{\partial z} = \frac{\partial}{\partial r}\left(\frac{e^x}{r}\frac{\partial \psi}{\partial r}\right) + \frac{e^x}{rL^2}\frac{\partial^2 \psi}{\partial z^2} \tag{A71}$$

or:

$$\zeta\ r^2 e^{-x} = re^{-x}\ \frac{\partial}{\partial r}\left(\frac{e^x}{r}\frac{\partial \psi}{\partial r}\right) + \frac{1}{L^2}\frac{\partial^2 \psi}{\partial z^2} \tag{A72}$$

With these definitions for the stream function ψ and vorticity ζ, the energy equation reads:

$$\frac{Br}{L}\frac{\partial \psi}{\partial z} = E\left[\frac{1}{r}\frac{\partial}{\partial r}\left(r\frac{\partial \theta}{\partial r}\right) + \frac{1}{L^2}\frac{\partial^2 \theta}{\partial z^2}\right] \tag{A73}$$

and for the azimuthal velocity equation:

$$\frac{-2}{r^2 L}\frac{\partial \psi}{\partial z} = E\left[\frac{1}{r}\frac{\partial}{\partial r}\left(\frac{1}{r}\frac{\partial r^2 \omega}{\partial r}\right) + \frac{1}{L^2}\frac{\partial^2 \omega}{\partial z^2}\right] \tag{A74}$$

Now two different formulations of the linear fluid dynamic model for a gas in a fast rotating cylinder have been derived:

- in primary variables eqs. (A44), (A47), (A50), (A59) and (A40);
- in stream function - vorticity eqs. (A68), (A72), (A73) and (A74).

From a mathematical point of view the differences are obvious and considerable:

- the ψ - ζ formulation is a model with four coupled elliptic partial differential equations
- the primary variable model consists of 6 equations of distinct different character.

In the remainder of this study, the "*stream function – vorticity"* model will be abbreviated as "ψ - ζ" model.

A9 Transformation of equations to pressure decay

In this section a transformation of the ψ - ζ description to the radial coordinate: x as introduced in eq. (A31) will be presented:

$$x = A(1-r^2) \text{ and } A = \frac{1}{2}\frac{Mv_w^2}{\overline{RT}} \tag{A75}$$

applying this coordinate then all derivatives to r can be written as:

$$\frac{\partial}{\partial r} = \frac{dx}{dr}\frac{\partial}{\partial x} = -2Ar\frac{\partial}{\partial x} \tag{A76}$$

Substituting this transformation into eqs. (A71) - (A74), results in:

vorticity

$$\frac{1}{L}\frac{\partial}{\partial z}(2\omega-\theta)e^{-x} = E\left[4A^2\frac{\partial^2(1-x/A)\zeta}{\partial x^2}+\frac{1}{L^2}\frac{\partial^2\zeta}{\partial z^2}\right] \tag{A77}$$

stream function

$$\zeta(1-x/A)\ e^{-x} = 4A^2(1-x/A)e^{-x}\frac{\partial}{\partial x}\left(e^x\frac{\partial\psi}{\partial x}\right)+\frac{1}{L^2}\frac{\partial^2\psi}{\partial z^2} \tag{A78}$$

energy

$$\frac{Br}{L}\frac{\partial\psi}{\partial z} = E\left[4A^2\frac{\partial}{\partial x}\left((1-x/A)\frac{\partial\theta}{\partial x}\right)+\frac{1}{L^2}\frac{\partial^2\theta}{\partial z^2}\right] \tag{A79}$$

azimuthal velocity

$$\frac{-2}{(1-x/A)L}\frac{\partial\psi}{\partial z} = E\left[4A^2\frac{\partial^2(1-x/A)\omega}{\partial x^2}+\frac{1}{L^2}\frac{\partial^2\omega}{\partial z^2}\right] \tag{A80}$$

and the definitions for the dimensionless stream function reads:

$$\frac{1}{L}\frac{\partial\psi}{\partial z} = -e^{-x}u\sqrt{(1-x/A)} \text{ and } \frac{\partial\psi}{\partial x} = -\frac{w}{2A}e^{-x} \tag{A81}$$

A10 Discussion on model equations

The equation for the stream function as applied by Brouwers [3] and [4] reads:

$$\frac{\partial w}{\partial z}(2\omega-\theta)=LE\left[\left\{\ \frac{1}{r}\frac{\partial}{\partial r}e^{x}\,\frac{1}{r}\frac{\partial}{\partial r}r^{2}+L^{-2}e^{x}\,\frac{\partial^{2}}{\partial z^{2}}\ \right\}^{2}-\frac{4}{3}\left\{2AL^{-1}e^{x}r\frac{\partial}{\partial z}\right\}^{2}\right](\frac{\psi}{r^{2}}) \quad \text{(A82)}$$

The right hand side operator in eq. (A82) is to be split into two equations to compare this result with the derived equations in the previous sections:

$$\frac{\partial w}{\partial z}(2\omega-\theta)=\ LE\left[\left\{\ \frac{1}{r}\frac{\partial}{\partial r}e^{x}\,\frac{1}{r}\frac{\partial}{\partial r}r^{2}+L^{-2}e^{x}\,\frac{\partial^{2}}{\partial z^{2}}\ \right\}\zeta-\frac{4}{3}\left\{2AL^{-1}e^{x}r\frac{\partial}{\partial z}\right\}^{2}(\frac{\psi}{r^{2}})\right] \quad \text{(A83)}$$

$$\zeta=\left[\frac{1}{r}\frac{\partial}{\partial r}e^{x}\,\frac{1}{r}\frac{\partial}{\partial r}r^{2}+L^{-2}e^{x}\,\frac{\partial^{2}}{\partial z^{2}}\right](\frac{\psi}{r^{2}}) \quad \text{(A84)}$$

Rearranging terms in eq. (A84) yields:

$$r^{2}\ \zeta\ e^{-x}=re^{-x}\frac{\partial}{\partial r}\left(\frac{e^{x}}{r}\frac{\partial\psi}{\partial r}\right)+\frac{1}{L^{2}}\frac{\partial^{2}\psi}{\partial z^{2}} \quad \text{(A85)}$$

This result is identical to eq. (A72). Rearranging terms in eq. (A83) results in:

$$\frac{\partial}{\partial z}(2\omega-\theta)e^{-x}\ =LE\left[\frac{e^{-x}}{r}\frac{\partial}{\partial r}\left(\frac{e^{x}}{r}\frac{\partial r^{2}\zeta}{\partial r}\right)+\frac{\partial^{2}\zeta}{L^{2}\partial z^{2}}\right]-\frac{4}{3}\left\{2AL^{-1}e^{x}\frac{\partial}{\partial z}\right\}^{2}(\psi) \quad \text{(A86)}$$

When comparing these equations and the derived set in the previous sections, two differences are found:

(1) comparing the vorticity eqs. (A86) and (A68) shows that Brouwers [3], [4] analysis results in a term for the radial diffusion eq. (A86): $\frac{e^{-x}}{r}\frac{\partial}{\partial r}\frac{e^{x}}{r}\frac{\partial r^{2}\zeta}{\partial r}$, while eq. (A68) results in $\frac{1}{r}\frac{\partial}{\partial r}\left(\frac{1}{r}\frac{\partial r^{2}\zeta}{\partial r}\right)$

This term is identical when compared to Dickinson and Jones [17] and Schroeder and Hanel [23].

(2) Brouwers includes a correction for the divergence of a compressible gas in the right hand side of the vorticity eq. (A83):

$$-\frac{4}{3}\left\{2AL^{-1}e^{x}\,\frac{\partial}{\partial z}\right\}^{2}(\psi)$$

This term could not be reproduced in the analysis in this appendix and is not included in Dickinson and Jones [17] and Schroeder and Hanel [23].

A11 Transformation of the separation equation

In Chapter 1, the equation to calculate the separation performance has been presented as based on widely accepted literature. Here these equations will be transformed applying the radial coordinate *x* and the parameter *A*.

Separation performance follows from eq. (1.5):

$$\delta U = 0.81 E_f m^2 /(1+m^2)\delta U_{\max} \qquad \text{[kg/s]}$$

Here E_f is the flow efficiency and m the flow strength, eqs. (1.6) - (1.9), applying the dimensionless radial coordinate r:

$$E_f = \frac{4\left[\int_0^1 \psi^*(r)\,r\,dr\right]^2}{\int_0^1 \frac{\left[\psi^*(r)\right]^2}{r}\,dr} \qquad \text{[-]} \qquad \text{(A87)}$$

$$m = \sqrt{\int_0^1 \frac{\psi^*(r)^2}{r}\,dr} \Big/ \left(\sqrt{2}\pi\rho a D\right) \qquad \text{[-]} \qquad \text{(A88)}$$

$$\delta U_{\max} = \frac{\pi l \rho D}{2}\left[\frac{\Delta M v_w^2}{2R_0T_0}\right]^2 \qquad \text{[kg/s]} \qquad \text{(A89)}$$

Here $\psi(r)$ is defined as the stream function according to:

$$\psi^*(r) = 2\pi a^2 \int_0^r \rho(r^*)w(r^*)r^*\,dr^* \qquad \text{[kg/s]} \qquad \text{(A90)}$$

By applying the definitions for the radial coordinate (*x),* velocity parameter (A), Ekman number (*E)* and the dimensionless variables eq. (A10), eqs. (A87) - (A89) can be transformed in the following expressions:

flow efficiency

$$E_f = \frac{2\left[\int_0^A \psi(x)dx\right]^2}{A\int_0^A \frac{[\psi(x)]^2}{(1-x/A)}dx} \qquad [-] \qquad (A91)$$

flow strength

$$m = \varepsilon \frac{\mu}{\rho D}\sqrt{\int_0^A \frac{\psi(x)^2}{(1-x/A)}dx E^{-1}A^{-1/2}} \qquad [-] \qquad (A92)$$

or

$$m = \varepsilon\ m^* \qquad [-] \qquad (A93)$$

with m^* representing the intrinsic flow strength defined by

$$m^* = \frac{\mu}{\rho D}\sqrt{\int_0^A \frac{\psi(x)^2}{(1-x/A)}dx E^{-1}A^{-1/2}} \qquad [-] \qquad (A94)$$

Maximum separation performance

$$\delta U_{\max} = \frac{\pi l \rho D}{2}\left(\frac{\Delta M}{M}\right)^2 A^2 \qquad [kg/s] \qquad (A95)$$

Values of the stream function will vary along the z-axis resulting in varying values of E_f and *m* along the *z*-axis, therefore averaged values of eqs. (A91) and (A94) will be used.

Appendix B

Derivation of Onsager's equation

The basis for Onsager's equation is the set of linearised equations as derived in Appendix A, (A68), (A72) to (A74):

vorticity

$$\frac{1}{L}\frac{\partial}{\partial z}(2\omega-\theta)e^{-x} = E\left[\frac{1}{r}\frac{\partial}{\partial r}\left(\frac{1}{r}\frac{\partial r^2\zeta}{\partial r}\right)+\frac{1}{L^2}\frac{\partial^2\zeta}{\partial z^2}\right] \tag{B1}$$

stream function

$$\zeta\ r^2e^{-x} = re^{-x}\frac{\partial}{\partial r}\left(\frac{e^x}{r}\frac{\partial\psi}{\partial r}\right)+\frac{1}{L^2}\frac{\partial^2\psi}{\partial z^2} \tag{B2}$$

azimuthal velocity

$$-\frac{2}{r^2L}\frac{\partial\psi}{\partial z} = E\left[\frac{1}{r}\frac{\partial}{\partial r}\left(\frac{1}{r}\frac{\partial r^2\omega}{\partial r}\right)+\frac{1}{L^2}\frac{\partial^2\omega}{\partial z^2}\right] \tag{B3}$$

energy

$$\frac{Br}{L}\frac{\partial\psi}{\partial z} = E\left[\frac{1}{r}\frac{\partial}{\partial r}\left(r\frac{\partial\theta}{\partial r}\right)+\frac{1}{L^2}\frac{\partial^2\theta}{\partial z^2}\right] \tag{B4}$$

Onsager's approach is based on two more assumptions:

- *L* is very large, so that the terms containing $\frac{1}{L^2}$ can be neglected
- the area of interest is only a very thin layer of gas immediately adjacent to the wall. This implies that algebraic formulations in *r* can be neglected in the set of equations above.

Applying these assumptions, the set of equations (B1) – (B4) become:

vorticity

$$\frac{1}{L}\frac{\partial}{\partial z}(2\omega-\theta)e^{-x} = E\frac{\partial^2\zeta}{\partial r^2} \tag{B5}$$

stream function

$$\zeta = \frac{\partial}{\partial r}\left(e^x\frac{\partial\psi}{\partial r}\right) \tag{B6}$$

azimuthal velocity

$$-\frac{2}{L}\frac{\partial\psi}{\partial z} = E\frac{\partial^2\omega}{\partial r^2} \tag{B7}$$

energy

$$\frac{Br}{L}\frac{\partial \psi}{\partial z} = E\frac{\partial^2 \theta}{\partial r^2} \tag{B8}$$

The Onsager analysis continues as follows:

Combining eq. (B5) and (B6) results in:

$$\frac{\partial}{\partial z}(2\omega - T) = LEe^x \frac{\partial^3}{\partial r^3}\left(e^x \frac{\partial \psi}{\partial r}\right) \tag{B9}$$

Twice differentiation eq. (B9) with respect to *r* results in:

$$\frac{\partial}{\partial z}\left[\frac{\partial^2}{\partial r^2}(2\omega - \theta)\right] = LE\frac{\partial^2}{\partial r^2}\left[e^x \frac{\partial^3}{\partial r^3}\left(e^x \frac{\partial \psi}{\partial r}\right)\right] \tag{B10}$$

Differentiating eq. (B7) and eq. (B8) to *z* and substituting them into eq. (B10) results in Onsager's equation:

$$\frac{\partial^2}{\partial r^2}\left[e^x \frac{\partial^3}{\partial r^3}\left(e^x \frac{\partial \psi}{\partial r}\right)\right] + B^2 \frac{\partial^2 \psi}{\partial z^2} = 0 \tag{B11}$$

with B defined as:

$$B^2 = \frac{(Br + 4)}{L^2 E^2} \tag{B12}$$

Because at moderate velocities $Br \approx 1$ then eq. (B12) can be simplified to:

$$B^2 = \frac{5}{L^2 E^2} \tag{B13}$$

Next a transformation in eq. (B11) to the radial coordinate defined by: $x = A(1 - r^2)$ is applied:

$$\frac{\partial^2}{\partial x^2}\left[e^x \frac{\partial^3}{\partial x^3}\left(e^x \frac{\partial \psi}{\partial x}\right)\right] + B^{*2} \frac{\partial^2 \psi}{\partial z^2} = 0 \tag{B14}$$

For $B^* << 1$ and a linear temperature gradient along the wall at *x = 0*, the lowest eigenvalue solution of eq. (B14) is, see Brouwers [42]:

$$\psi \sim e^{-x}(1 - e^{-x} - xe^{-x}) \tag{B15}$$

Substituting eq. (B15) into eq. (A91) and by assuming that $x/A << 1$, results in:

$$E_f = \frac{7.2}{A} \qquad [-] \qquad \text{(B16)}$$

or

$$E_f = \frac{720}{A} \qquad [\%] \qquad \text{(B17)}$$

This is the limiting solution of the flow efficiency for an infinitely long centrifuge at very high wall velocity, where the internal flow is driven by a linear temperature gradient along the wall.

Appendix C

Discretisation of equations

In Chapter 4 the discrete form of the vorticity equation is given; in this appendix the discrete version of the remaining equations will be discussed and presented.

C1 Stream function

The partial differential equation for the stream function is given in eq. (A78):

$$\zeta(1-x/A)\ e^{-x} = 4A^2(1-x/A)e^{-x}\frac{\partial}{\partial x}\left(e^{x}\frac{\partial \psi}{\partial x}\right)+\frac{1}{L^2}\frac{\partial^2 \psi}{\partial z^2} \qquad \text{(C1)}$$

The equation is solved centrally at the same mesh i,j as the vorticity equation. Applying the same technique as for the vorticity equation, the stream function equation results in:

$$4A^2(1-x/A)e^{-x}\Big|_i \frac{d\eta}{dx}\Big|_i \left\{\frac{\partial}{\partial \eta}\left[e^{x}\frac{d\eta}{dx}\left(\frac{\partial \psi}{\partial \eta}\right)\right]\right\}\Bigg|_{i,j} \sim$$

$$4A^2((1-x/A)e^{-x}\frac{d\eta}{dx})\Big|_i \left\{(e^{x}\frac{d\eta}{dx})\Big|_{i+1/2}\left[\frac{\psi_{i+1.j}}{(\delta\eta)^2}-\frac{\psi_{i.j}}{(\delta\eta)^2}\right]\right\}$$

$$-4A^2((1-x/A)e^{-x}\frac{d\eta}{dx})\Big|_i \left\{(e^{x}\frac{d\eta}{dx})\Big|_{i-1/2}\left[\frac{\psi_{i.j}}{(\delta\eta)^2}-\frac{\psi_{i-1.j}}{(\delta\eta)^2}\right]\right\}+\ O(\delta\eta^2) \qquad \text{(C2)}$$

The second term at the right hand side of eq. (C1) results in:

$$\frac{1}{L^2}\frac{d\xi}{dz}\Big|_j \left\{\frac{\partial}{\partial \xi}\left[\frac{d\xi}{dz}\left(\frac{\partial \psi}{\partial \xi}\right)\right]\right\}\Bigg|_{i,j} \sim \frac{1}{L^2}\frac{d\xi}{dz}\Big|_j \left\{\frac{d\xi}{dz}\Big|_{j+1/2}\left[\frac{\psi_{i,j+1}}{(\delta\xi)^2}-\frac{\psi_{i.j}}{(\delta\xi)^2}\right]\right\}$$

$$-\frac{1}{L^2}\frac{d\xi}{dz}\Big|_j \left\{\frac{d\xi}{dz}\Big|_{j-1/2}\left[\frac{\psi_{i,j}}{(\delta\xi)^2}-\frac{\psi_{i.j-1}}{(\delta\xi)^2}\right]\right\}+\ O(\delta\xi^2) \qquad \text{(C3)}$$

The term in the left hand side of eq. (C1) results in:

$$\zeta(1-x/A)\ \ e^{-x} = ((1-x/A)e^{-x})\Big|_i\ \zeta_{i,j} \qquad \text{(C4)}$$

Combining eqs. (C3) and (C4) results in a linear equation for the discrete version of the stream function. The boundary conditions for the stream function are very simple to incorporate.

C2 Energy equation

The energy equation is derived in Appendix A, eq. (A79):

$$\frac{Br}{L}\frac{\partial \psi}{\partial z} = E\left[4A^2\frac{\partial}{\partial x}\left((1-x/A)\frac{\partial \theta}{\partial x}\right)+\frac{1}{L^2}\frac{\partial^2 \theta}{\partial z^2}\right] \tag{C5}$$

As discussed in Section 4.3, the equation for temperature is solved on a mesh shifted downwards in the i,j mesh by half a grid size. Discretisation of the left hand term of eq. (C5) results in:

$$\frac{Br}{LE}\frac{\partial \psi}{\partial z} = \frac{Br}{LE}\frac{d\xi}{dz}\bigg|_{j-1/2}\frac{\partial \psi}{\partial \xi}\bigg|_{i,j-1/2} \sim$$
$$\frac{Br}{LE}\frac{d\xi}{dz}\bigg|_{j-1/2}\left\{\frac{\psi_{i,j}}{\delta\xi}-\frac{\psi_{i,j-1}}{\delta\xi}\right\}+O(\delta\xi^2) \tag{C6}$$

while the right hand term of eq. (C5) becomes:

$$4A^2\frac{d\eta}{dx}\bigg|_i\left\{\frac{\partial}{\partial\eta}\left[(1-x/A)\frac{d\eta}{dx}\left(\frac{\partial\theta}{\partial\eta}\right)\right]\right\}\bigg|_{i,j-1/2} \sim$$
$$4A^2\frac{d\eta}{dx}\bigg|_i\left\{((1-x/A)\frac{d\eta}{dx})\bigg|_{i+1/2}\left[\frac{\theta_{i+1.j}}{(\delta\eta)^2}-\frac{\theta_{i.j}}{(\delta\eta)^2}\right]\right\}$$
$$-4A^2\frac{d\eta}{dx}\bigg|_i\left\{((1-x/A)\frac{d\eta}{dx})\bigg|_{i-1/2}\left[\frac{\theta_{i.j}}{(\delta\eta)^2}-\frac{\theta_{i-1.j}}{(\delta\eta)^2}\right]\right\}+O(\delta\eta^2) \tag{C7}$$

and the second term in the right hand side of eq. (C5):

$$\frac{1}{L^2}\frac{d\xi}{dz}\bigg|_j\left\{\frac{\partial}{\partial\xi}\left[\frac{d\xi}{dz}\left(\frac{\partial\theta}{\partial\xi}\right)\right]\right\}\bigg|_{i,j} \sim \frac{1}{L^2}\frac{d\xi}{dz}\bigg|_j\left\{\frac{d\xi}{dz}\bigg|_{j+1/2}\left[\frac{\theta_{i,j+1}}{(\delta\xi)^2}-\frac{\theta_{i.j}}{(\delta\xi)^2}\right]\right\}$$
$$-\frac{1}{L^2}\frac{d\xi}{dz}\bigg|_j\left\{\frac{d\xi}{dz}\bigg|_{j-1/2}\left[\frac{\theta_{i,j}}{(\delta\xi)^2}-\frac{\theta_{i.j-1}}{(\delta\xi)^2}\right]\right\}+O(\delta\xi^2) \tag{C8}$$

C3 Azimuthal velocity equation

The azimuthal velocity equation as derived before, eq. (A80):

$$\frac{-2}{(1-x/A)L}\frac{\partial\psi}{\partial z} = E\left[4A^2\,\frac{\partial^2(1-x/A)\omega}{\partial x^2}+\frac{1}{L^2}\frac{\partial^2\omega}{\partial z^2}\right] \tag{C9}$$

As discussed in Section 4.3, the equation for the azimuthal velocity is solved on a mesh shifted upwards in the i,j mesh by half a grid size. Discretisation of the left hand term of eq. (C9) results in:

$$\frac{-2}{(1-x/A)LE}\frac{\partial\psi}{\partial z} = \frac{-2}{(1-x/A)LE}\frac{d\xi}{dz}\bigg|_{j+1/2}\frac{\partial\psi}{\partial\xi}\bigg|_{i,j+1/2} \sim$$
$$\frac{-2}{(1-x/A)LE}\bigg|_i\frac{d\xi}{dz}\bigg|_{j+1/2}\left\{\frac{\psi_{i,j+1}}{\delta\xi}-\frac{\psi_{i,j}}{\delta\xi}\right\}+O(\delta\xi^2) \tag{C10}$$

The right hand side term of eq. (C9) becomes:

$$4A^2\,\frac{d\eta}{dx}\bigg|_i\left\{\frac{\partial}{\partial\eta}\left[\frac{d\eta}{dx}\left(\frac{\partial(1-x/A)\omega}{\partial\eta}\right)\right]\right\}\bigg|_{i,j+1/2} \sim$$
$$4A^2\,\frac{d\eta}{dx}\bigg|_i\left\{\frac{d\eta}{dx}\bigg|_{i+1/2}\left[(1-x/A)\big|_{i+1}\frac{\omega_{i+1.j}}{(\delta\eta)^2}-(1-x/A)\big|_i\frac{\omega_{i.j}}{(\delta\eta)^2}\right]\right\}$$
$$-4A^2\,\frac{d\eta}{dx}\bigg|_i\left\{\frac{d\eta}{dx}\bigg|_{i-1/2}\left[(1-x/A)\big|_i\frac{\omega_{i.j}}{(\delta\eta)^2}-(1-x/A)\big|_{i-1}\frac{\omega_{i-1.j}}{(\delta\eta)^2}\right]\right\}+O(\delta\eta^2) \tag{C11}$$

while the second term at the right hand side becomes:

$$\frac{1}{L^2}\frac{d\xi}{dz}\bigg|_j\left\{\frac{\partial}{\partial\xi}\left[\frac{d\xi}{dz}\left(\frac{\partial\omega}{\partial\xi}\right)\right]\right\}\bigg|_{i,j} \sim \frac{1}{L^2}\frac{d\xi}{dz}\bigg|_j\left\{\frac{d\xi}{dz}\bigg|_{j+1/2}\left[\frac{\omega_{i,j+1}}{(\delta\xi)^2}-\frac{\omega_{i.j}}{(\delta\xi)^2}\right]\right\}$$
$$-\frac{1}{L^2}\frac{d\xi}{dz}\bigg|_j\left\{\frac{d\xi}{dz}\bigg|_{j-1/2}\left[\frac{\omega_{i,j}}{(\delta\xi)^2}-\frac{\omega_{i.j-1}}{(\delta\xi)^2}\right]\right\}+O(\delta\xi^2) \tag{C12}$$

Appendix D

Stretching functions

In this appendix some background information on the calculations of the Semi-long centrifuge presented in Section 4.6 are given to illustrate the stretching of the coordinates.

Applying the standard settings, see Section 4.2.1 and Section 4.2.2, for the stretching of the axial coordinate: $\xi = \xi(z)$ and radial coordinate $\eta = \eta(x)$, results in functions as illustrated in Figure D1 and Figure D2.

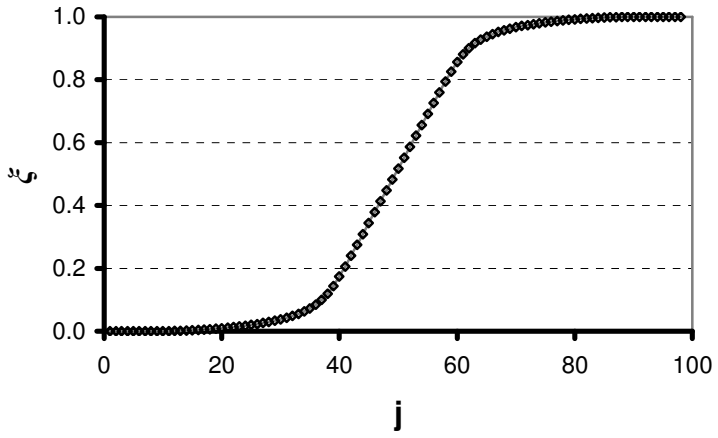

Figure D1: Illustration of the axial stretching function, $\xi = \xi(z)$.

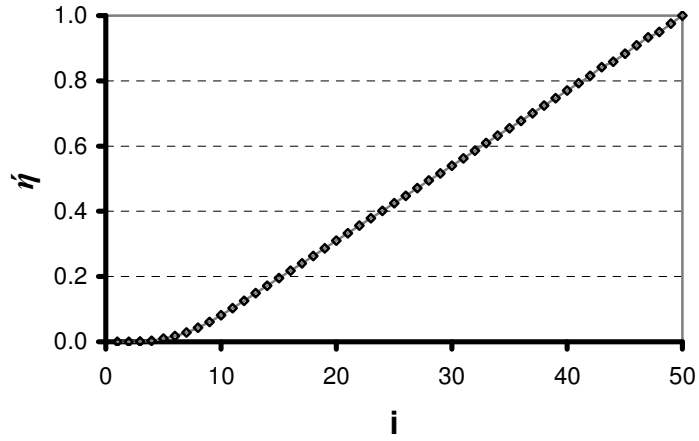

Figure D2: Illustration of the radial stretching function, $\eta = \eta(x)$.

Summary

There are two physical phenomena playing a role in predicting the performance of a gas centrifuge used for isotope separation:

- the isotope separation, this was described in the 1960's, e.g. by Los [36]
- the transport of the isotopes by the gas flow in the centrifuge. The latter has been described by applying analytical methods in the 1970's, e.g. by Brouwers [42].

The latter work clarifies the gas dynamics and how it impacts on the final efficiency of a gas centrifuge under the assumption of simplified and idealised boundary conditions. Assumptions were needed to be made since analytical solutions for more complex boundary conditions were not available and are not available at present day. Numerical methods that became available over the last decades make it possible to model a gas centrifuge in much larger detail and clarify the gas flow in great detail applying realistic conditions. This is the subject of the present thesis.

The numerical model developed for this application is based on a linearised set of fundamental equations describing momentum, mass and energy transport of a heavy ideal gas rotating at very high velocities. An efficient algorithm has been developed to solve the resulting set of four stiff coupled elliptic differential equations. The final software package programmed in C++ runs easily on an average PC.

The numerical analysis in this thesis is focussing on the effects that complex boundary conditions have on the gas flow like strongly axial nonsymmetrical boundary conditions as they are applied in real applications. A specific example at the bottom end cap of the centrifuge is: strongly increasing temperatures towards the centre line subsequently cut off at realistic levels and a constant temperature at the top end cap. These types of boundary conditions affect the resulting gas flow significantly and hence the separation efficiency of the centrifuge.

Next, a new display of results is presented to be used as an engineering tool. It enables a user to predict the resulting separation efficiency of a gas centrifuge, subject to chosen boundary conditions, within a few percent accurate.

This single graph presentation is used to compare analytical results with the numerical results of this study. The results are in very good agreement and the differences due to the assumptions made in the analytical model are explained.

The analytical work is based on theories developed in geophysical disciplines and results in separating the gas flow into various flow regions separated by vertical boundary layers parallel to the rotation axis of the centrifuge. The existence of the boundary layers separating the all-diffusive core and the viscous region is proven numerically in this thesis by applying "pulse tests". Locally introduced disturbances are followed in the flow field and show the changing local gas dynamic character of the region. Results are very much in line with the analytic predictions.

The Brinkman number, which is defined as the ratio of the production of heat and its conductivity increases strongly with the applied wall velocities. Careful comparison between the analytical and numerical model shows that the analytical approach maintains its viability up to very high velocities. The correction for increasing values of the Brinkman number, incorporated in the Ekman suction relation, is accurate.

The thermal properties of the wall and end caps as well as the heat transfer coefficient between the rotating cylinder and the environment has a limited effect on the overall separating performance of a gas centrifuge.

Samenvatting

Er zijn twee fysische fenomenen die een rol spelen bij het voorspellen van het scheidend vermogen van een gascentrifuge, zoals die gebruikt wordt voor het scheiden van isotopen:

- men moet de achterliggende fysica van isotopenscheiding begrijpen. Dit is gerealiseerd in de 60-er jaren. Zie bijvoorbeeld het werk van Los [36].
- vervolgens moet het eigenlijke transport van isotopen als gevolg van de gasstroom begrepen worden. Dit probleem is met behulp van analytische methoden opgelost in de 70-er jaren; zie Brouwers [4].

Dit laatste werk verklaart de gasdynamica en hoe dit uiteindelijk invloed heeft op de efficiency van een gascentrifuge onder aanname van vereenvoudigde en geïdealiseerde randvoorwaarden. Deze aannames waren noodzakelijk, omdat analytische oplossingen voor meer complexe randvoorwaarden tot de dag van vandaag niet bekend zijn. Numerieke methoden die de laatste decennia beschikbaar gekomen zijn, maken het mogelijk om een gascentrifuge te modelleren in veel groter detail en de gasstroming te kunnen verklaren onder complexe condities. Dit is het onderwerp van dit proefschrift.

Het numerieke model dat ontwikkeld is voor deze toepassing, is gebaseerd op een set gelineariseerde vergelijkingen die het impuls-, massa- en energietransport van een zwaar ideaal gas, roterend bij zeer hoge snelheden, beschrijft. Een efficiënt algoritme is ontwikkeld dat de resulterende set lineaire vergelijkingen oplost. Het uiteindelijke model is geimplementeerd in C++ en kan gemakkelijk op een gemiddelde PC, anno 2010, gebruikt worden.

De numerieke analyse in dit proefschrift concentreert zich op de effecten die complexe randvoorwaarden hebben op de gasstroming, zoals niet axiaal antisymmetrische condities die in werkelijke toepassingen worden gebruikt. Een specifiek voorbeeld voor de bodem van de centrifuge zijn de sterk toenemende temperaturen naar het centrum die afgekapt worden op realistische waarden, terwijl de bovenplaat op een uniforme lagere temperatuur gehouden wordt. Het effect dat dit soort randvoorwaarden heeft op de resulterende gasstroming en daarmee op de scheidingsefficiency van de centrifuge, is aanzienlijk.

Vervolgens wordt een handige weergave van resultaten gepresenteerd die nuttig is voor ingenieurs. Het stelt de gebruiker in staat om eenvoudig de resulterende scheidingsefficiency van een gascentrifuge te berekenen. Voor de berekeningen is alleen een zakrekenmachine nodig. Deze enkelvoudige grafieken, zie bijv. Figuur 5.9, zijn gebruikt om bovengenoemde analytische resultaten te vergelijken met de numerieke resultaten van deze studie. De resultaten zijn goed vergelijkbaar, en de verschillen die er zijn, zijn verklaarbaar.

Het analytische werk is gebaseerd op een theorie, die ontwikkeld is in geofysische disciplines. Dit resulteert in het onderscheiden van verschillende dynamische en

thermische balansen. Hiermee is de gasstroming in de centrifuge onder te verdelen in diverse stromingsgebieden. Deze gebieden worden gescheiden door verticale grenslagen, evenwijdig aan de rotatieas van de centrifuge. Het bestaan van de grenslaag tussen het geheel door diffusie gedomineerde gebied en het visceuze gebied wordt numeriek anngetoond in dit proefschrift door zogenaamde “puls-testen”. Lokale verstoringen worden gevolgd in het stromingsveld en laten het lokale gas-dynamische karakter zien. De resultaten zijn erg goed vergelijkbaar met de analytische voorspellingen.

Het Brinkman-getal, dat de verhouding weergeeft van de productie en diffusie van warmte, neemt sterk toe met de toegepaste wandsnelheden. Nauwkeurig vergelijken van resultaten van het analytische en van het numerieke model laat zien dat de analytische aanpak zijn waarde behoudt, en dat de correctie bij toenemende waarden van het Brinkman-getal nauwkeurig is.

De thermische eigenschappen van de wand met einddeksels, zowel als de thermische condities tussen de roterende cilinder en zijn omgeving, heeft maar een beperkt effect op het uiteindelijke scheidende vermogen van een gascentrifuge.

Dankwoord

Geachte lezer, hierbij bent u aangekomen bij het dankwoord. Zoals bij veel proefschriften is dit waarschijnlijk het meest gelezen deel.

Promoveren tot doctor in de technische wetenschappen is een wens die ik al heel lang heb. Door diverse oorzaken heeft het lang geduurd voordat het er echt van kwam. Ook heb ik al heel lang interesse in de fysica van snel roterende zware gassen. Gedurende de laatste 10 jaar heb ik nogal wat over de wereld gezworven voor mijn werk en het Internet maakte het mogelijk om de literatuur op dit vakgebied, waar ook ter wereld, te blijven volgen en aan het onderwerp te werken. In het voorjaar en de zomer van 2007 kon mijn vrouw Hammy, door externe factoren, niet bij me zijn in Nigeria. In die periode ben ik de zaken betreffende dit onderwerp eens goed op een rij gaan zetten en in het voorjaar van 2008 heb ik vervolgens Theo van der Meer benaderd met een plan van aanpak. Gelukkig kreeg ik snel en enthousiast support van hem aangeboden en begon ik er vertrouwen in te krijgen, dat dit tot een promotievoorstel kon leiden.

Het proefschrift ligt nu voor u. Dat betekent dat het vrijwel afgerond is, en het completeert voorlopig mijn persoonlijk opleidingstraject.

Terugkijkend is er een enorme schakel van personen en instellingen ontstaan, die hebben geleid tot de totstandkoming van dit proefschrift. De belangrijkste zal ik hier noemen. Om te beginnen zijn het mijn ouders geweest, die de vooruitziende blik hadden om hun kinderen alle steun en vrijheid te geven om zich te ontwikkelen. Zij verdienen het daarom om als eerste te worden genoemd in dit dankwoord. Helaas zijn beiden al lang geleden overleden, maar ze zouden de promotieplechtigheid vol trots en in bescheidenheid hebben bijgewoond. Tijdens mijn studie aan de toenmalige Technische Hogeschool Twente heb ik ook veel steun gehad van mijn zus en zwager Annie en Jan Souman uit Hardenberg. Ook zij behoren hier genoemd te worden.

Prof. dr. ir. Theo van der Meer wil ik bedanken voor zijn ondersteuning, zijn inhoudelijke bijdrage en voor de persoonlijke coaching die ik van hem ontvangen heb. Zonder zijn steun zou dit proefschrift nooit zijn ontstaan. Hetzelfde geldt voor prof. dr. ir. Bert Brouwers, die een buitengewone kennis van dit vakgebied heeft en ook veel inbreng heeft gehad in de totstandkoming van dit proefschrift. Prof. dr. ir. Gert Jan van Heijst ben ik zeer dankbaar voor de inhoudelijke discussie over het onderwerp en voor zijn vele en zeer gewaardeerde commentaren op het conceptproefschrift in zijn rol als commissielid .

Als laatste spreek ik mijn dank uit voor de stimulans die ik gekregen heb van mijn gezin: Marjanka, Rik en mijn vrouw Hammy. De laatste steunt, adviseert en trekt al meer dan 30 jaar met me mee door het leven. Niet veel mannen hebben een partner die het volhoudt om door diverse gewesten in Nederland, de woestijn van Saudi-Arabië, Amerika, de jungle van Nigeria en over de steppe van Kazakstan te trekken. Ik ben erg blij dat zij dit wel gedaan heeft en bewonder dat ten zeerste. Dat is dan ook de reden waarom het proefschrift aan haar is opgedragen.

Klaas van Ommen, april 2010, Kazakstan.